IPP-Report

Max-Planck-Institut
für Plasmaphysik

Nina Schwarz

Vertical Displacement Events in ASDEX Upgrade

IPP 2020-14
November 2020

Department of Physics and Astronomy
University of Heidelberg

Master thesis
in Physics
submitted by
Nina Schwarz
born in Gunzenhausen
2020

Vertical Displacement Events
in
ASDEX Upgrade

This Master thesis has been carried out by Nina Schwarz
at the
Max Planck Institute for Plasma Physics (IPP Garching)
under the supervision of
Prof. Dr. Friedrich Röpke (University of Heidelberg)
Second Supervisor: Prof. Dr. Sibylle Günter (IPP Garching)
Daily Supervisor: Dr. Matthias Hölzl (IPP Garching)

Simulationen von Vertical Displacement Events in ASDEX Upgrade:

Fusionskraftwerke, in denen ein Plasma unter Fusionsbedingungen durch Magnetfeldern eingeschlossen wird, können eine Möglichkeit aufzeigen, den wachsenden Elektrizitätsbedarf zu decken. Es ist jedoch eine Herausforderung, ein Plasma ausreichend lange unter hohen Temperaturen und Dichten aufrecht zu erhalten, ohne dass Instabilitäten zu einem Verlust der Plasmaenergie führen. Eine Art von Instabilität, das Vertical Displacement Event (VDE), eine schnelle vertikale Bewegung des Plasmas, muss vollständig vermieden oder zumindest in ihren Konsequenzen mitigiert werden. Realitätsnahe Simulationen ermöglichen es, die zu Grunde liegende Physik zu verstehen, um Vorhersagen zu zukünftigen Experimenten zu treffen und Mitigationstechniken zu testen. Zu diesem Zweck werden in der vorliegenden Masterarbeit Simulationen mit den Codes JOREK und STARWALL zur Untersuchung von VDEs in der realistischen Geometrie des Tokamaks ASDEX Upgrade durchgeführt und der Einsatz eines virtuellen Reglers in der Simulation zur Kontrolle der vertikalen Position des Plasmas untersucht. Die Validierung von passiven Spulen, ein Benchmark mit einem linearen MHD Code und Untersuchungen zur VDE Dynamik bilden die Grundlage für die darauffolgenden Simulationen. Untersucht wird zum einen die axisymmtrische Entwicklung des Plasmas nach einem künstlich hervorgerufenen Thermal Quench, einem Verlust der thermischen Energie, als auch die 3D Entwicklung eines durch Instabilitäten hervorgerufenen Energieverlusts durch eine massive, lokalisierte Dichtequelle, wie sie in Experimenten zur Mitigation genutzt wird.

Simulations of Vertical Displacement Events in ASDEX Upgrade:

Fusion power plants, which use magnetic fields to confine a plasma under fusion conditions, could show one possible way to supply for the increasing electricity demand. However, it proves to be challenging to keep a burning plasma at high temperatures and densities without the occurrence of instabilities causing a loss of the energy. One kind of instability, the Vertical Displacement Event (VDE), a fast vertical motion of the plasma, must be avoided completely or at least be mitigated. Reliable numerical simulations allow to understand the underlying physics to make predictions about future experiments or test mitigation techniques. Towards this goal, the present master thesis focuses on simulations with the codes JOREK and STARWALL, to study the dynamics of VDEs in the realistic geometry of the tokamak ASDEX Upgrade and explore the possibility of controlling the vertical position of the plasma. A thorough validation of passive conductive structures, a benchmark of the growth rate against a linear MHD code and investigations of the VDE dynamics were performed. Finally, simulations of the two-dimensional evolution of a VDE after an artificially triggered thermal quench, a loss of energy confinement, and 3D simulations of a thermal quench triggered by massive material injection as used for mitigation were carried out.

Contents

Contents II

Abbreviations IV

1 Introduction 1
- 1.1 Motivation . . . 1
- 1.2 Plasma and fusion basics . . . 1
- 1.3 Magnetic confinement fusion . . . 7
  - 1.3.1 Tokamaks . . . 7
  - 1.3.2 Tokamak plasma properties . . . 9
  - 1.3.3 The tokamak ASDEX Upgrade . . . 13
- 1.4 Vertical Displacement Events (VDEs) . . . 16
- 1.5 Scope of the thesis . . . 17

2 Theoretical Background 19
- 2.1 Magnetohydrodynamics . . . 19
  - 2.1.1 Equations . . . 19
  - 2.1.2 Equilibrium . . . 21
- 2.2 Vertical Displacement Events . . . 24
  - 2.2.1 The three wire model . . . 24
  - 2.2.2 Axisymmetric stability . . . 27
  - 2.2.3 VDE mechanisms . . . 31
  - 2.2.4 Asymmetric VDEs . . . 35
- 2.3 Control theory . . . 37
  - 2.3.1 Basics of control theory . . . 37
  - 2.3.2 PID controller . . . 39
  - 2.3.3 Vertical stability control in ASDEX Upgrade . . . 41
- 2.4 Tokamak modelling . . . 44
  - 2.4.1 The JOREK code . . . 44
  - 2.4.2 The STARWALL code . . . 47

3 Setup and modelling 49
- 3.1 Initial setup . . . 49
- 3.2 Coil modelling . . . 51
- 3.3 Vertical stability control in JOREK . . . 53

4 Results 56
- 4.1 Validation of axissymetric coils . . . 56
  - 4.1.1 Coil validation . . . 56
  - 4.1.2 Coil plasma interaction . . . 60
- 4.2 Benchmark with CASTOR3D . . . 66
- 4.3 VDE investigations . . . 70
  - 4.3.1 Different PSL geometries . . . 70
  - 4.3.2 Dependence on the wall resistivity . . . 72
  - 4.3.3 Dependence on the PSL resistance . . . 73
- 4.4 VDE Control . . . 75
  - 4.4.1 PID controller tests . . . 75

4.4.2 Elongation and shape scan 78
4.5 Artificial thermal quench 81
4.6 Thermal quench by Massive Material Injection 87

5 Summary and Conclusion **92**

A Acknowledgments **94**

B Lists **95**
B.1 List of Figures 95
B.2 List of Tables 96

C References **97**

D Magnetic axis finding **102**

Abbreviations

Physical quantities		**Unit**
$\mathbf{B}$	Magnetic field	[T]
$\mathbf{E}$	Electric field	$[\mathrm{V\,m^{-1}}]$
η	Resistivity	$[\Omega\,\mathrm{m}]$
$\mathbf{J}$	Current density	$[\mathrm{A\,m^{-2}}]$
σ	Conductivity	$[\mathrm{S\,m^{-1}}]$
Φ	Magnetic flux	$[\mathrm{T\,m^2}]$
ψ	Poloidal magnetic flux ($\psi = \frac{\Phi}{2\pi}$)	$[\mathrm{T\,m^2}]$
n	Number density	$[\mathrm{m^{-3}}]$
p	Pressure	$[\mathrm{N\,m^{-2}}]$
ρ	Mass density	$[\mathrm{kg\,m^{-3}}]$
T	Temperature	[K]
I	Current	[A]
$\mathcal{L}$	Inductance	[H]
$\mathcal{R}$	Resistance	[Ω]
Physical constants		
μ_0	Vacuum permeability	$4 \times 10^{-7}\pi\,\mathrm{H\,m^{-1}}$
ε_0	Vacuum permittivity	$8.858 \times 10^{-12}\,\mathrm{F\,m^{-1}}$
e	Electric unit charge	$1.9 \times 10^{-19}\,\mathrm{C}$
k_B	Boltzmann constant	$1.38 \times 10^{-23}\,\mathrm{J\,K^{-1}}$
Math abbreviations		
$\langle\cdot\rangle$	spatial average	
Tokamak quantities		
a	Minor Radius	[m]
κ	Elongation of plasma cross section	[–]
q	Safety factor	[–]
R_0	Major Radius	[m]
ϕ, θ,z	toroidal, poloidal angle, vertical coordinate	[rad],[rad],[m]
General abbreviations		
AUG	**A**SDEX **Upg**rade	
LHS/RHS	Left/ Right Hand Side (of an equation)	
CQ	**C**urrent **Q**uench	
MHD	**M**agneto**H**ydro**D**ynamics	
PFC	**P**lasma **F**acing **C**omponents	
PF coil	**P**oloidal **F**ield coil	
SOL	**S**crape–**O**ff **L**ayer	
TF coil	**T**oroidal **F**ield coil	
TQ	**T**hermal **Q**uench	
VDE	**V**ertical **D**isplacement **E**vent	

1 Introduction

1.1 Motivation

Plasma is a state of matter, in which atoms are partially or completely ionized due to high temperatures and densities. In this state, they are susceptible to influences of magnetic fields enforcing collective behavior on the charges. In fact, most of the matter in the universe exists in the plasma state, which requires temperatures above the characteristic ionization energy. Under these conditions, fusion reactions of two nuclei are possible, where the difference in masses Δm between the reactants and the products is released as kinetic energy ΔE according to Einstein's well known formula:

$$\Delta E = \Delta m c^2, \tag{1.1}$$

where c is the speed of light. These reactions also take place in stars like the sun, where the matter is partly ionized. It naturally is of interest whether it is possible to reproduce this kind of reaction in laboratory plasmas and ultimately generate electricity from the released energy. So far, the confinement of plasmas by magnetic fields has shown to be the most promising way of approaching fusion conditions. However, present devices are prone to large scale plasma instabilities, which limit the operation time and can damage the surrounding material. In this thesis, the vertical instability is addressed as one of the most critical problems for the devices.

In the following introduction, the basics of plasma physics and fusion are laid out before exploring one possible configuration of a fusion device in detail, the tokamak. After covering these principles, the vertical instability, which is a major concern for the safe operation of a tokamak, is briefly addressed and discussed more in detail in a later chapter. In the last section, the structure and scope of this thesis are lined out.

1.2 Plasma and fusion basics

The first part of this introduction covers the principles of plasma physics following the outline of [Che16] and [Miy16].

Fusion reactions: A plasma usually consists of electrons and positive ions, with charges of the same sign repelling each other due to the Coulomb force. In order to make fusion reactions between the ions possible, the so called Coulomb barrier between the repelling charges has to be overcome by their thermal energy and with help of quantum tunneling. Additionally, the plasma density has to be sufficiently high to allow for frequent collisions. The diagram of the binding energy per nucleon in figure 1.1 shows that the energy balance of fusion reactions is positive for elements up to iron. For heavier elements, energy can only be gained by fission reactions. Apart from the released energy per reaction, the reaction cross section, a measure for the probability, as a function of temperature is important for

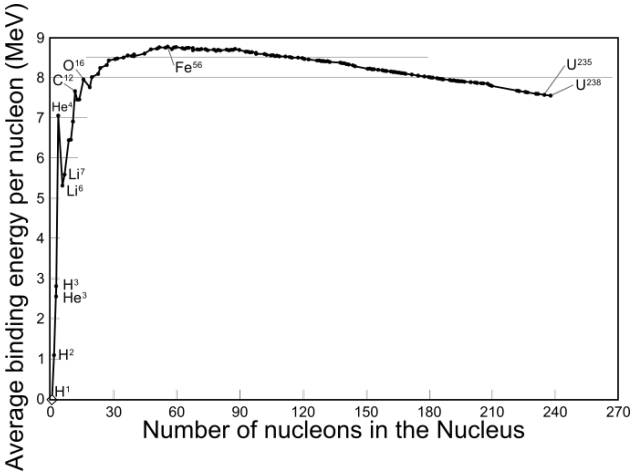

Figure 1.1: Binding energy per nucleon for different elements. The energy balance is positive, when the product has a higher binding energy than the initial elements. (adapted from [Eng])

the total energy output. It was found that the reaction of the hydrogen isotopes deuterium ($^2_1$H) and tritium ($^3_1$H),

$$^2_1\mathrm{H} + {}^3_1\mathrm{H} \rightarrow {}^4_2\mathrm{H}e + {}^1_0\mathrm{n} \quad (17.6\,\mathrm{MeV}), \tag{1.2}$$

is the most promising in terms of cross section and energy gain. The products are an α–particle ($^4_2$He) and a neutron, where the latter carries the largest portion of the energy (14 MeV) and therefore, making a massive shielding necessary for any fusion device relying on this reaction. Since the α–particles are charged, they remain in the plasma and supply additional heating. While deuterium is abundant and can, for example, be extracted from sea water, tritium does not exist in nature due to its short life time of 13 years. It has to be obtained either as a byproduct of fission reactors or, preferably, by a reaction of Lithium and a neutron, called Lithium breeding, directly inside the fusion device.

Having identified a suitable reaction, it needs to be studied under which conditions this reaction takes place and whether it is possible to sustain a plasma at this state. The density and temperature have to be maintained by suitable techniques, like the confinement of the plasma by magnetic fields, to obtain a large number of fusion reactions. This approach is of interest for this thesis, focusing on one type of device, the toroidal **tokamak** configuration. Typical temperatures and number densities in tokamaks are around 15 keV and $10^{20}\,\mathrm{m}^{-3}$. The ratio Q of the fusion power of the reaction P_{reaction} over the supplied heating power P_{heating},

$$Q = \frac{P_{\mathrm{reaction}}}{P_{\mathrm{heating}}}, \tag{1.3}$$

describes how close the device is to reactor conditions. ITER, the biggest tokamak so far,

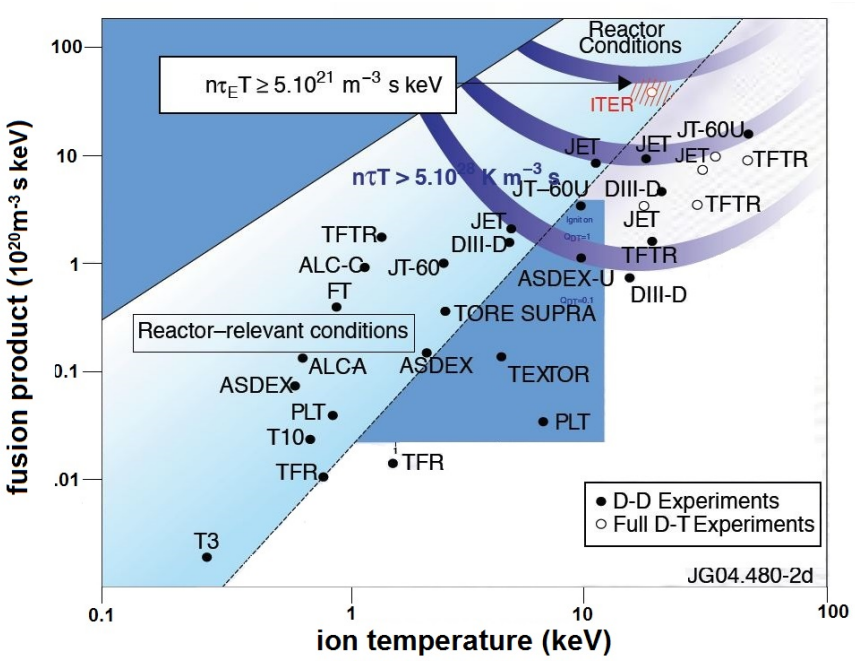

Figure 1.2: The triple product of density, temperature and cross section is a measure for the output power of the device. The development of the fusion product of different devices show how far research has advanced in the last years approaching the goal of a working power plant. (adapted from [Fus])

which is currently under construction, aims to reach a value of $Q = 10$ or higher.

For a power plant, the energy output by fusion reactions should be significantly higher than the energy necessary to heat and maintain the plasma. Also, the confinement time, defined by the ratio between energy density W and power losses P_{loss},

$$\tau_E = \frac{W}{P_{\text{loss}}}, \tag{1.4}$$

has to be maximized to improve the total energy output. In particular, two conditions have to be reached: one is the point, where the output power equals the input power, called **break even**. The other is defined as the point, where the kinetic energy of the α–particles is sufficient for heating and maintaining a self-sustained reaction, the **ignition condition** expressed by:

$$n\,T\,\tau_E \geq 5 \times 10^{21}\,\text{m}^{-3}\,\text{keV}\,\text{s}, \tag{1.5}$$

for the D–T reaction, where T is the plasma temperature and n its number density. The left hand side represents another figure of merit for fusion, the triple product of density, temperature and confinement time referred to as the **fusion product**, which has to cross a certain threshold to reach the above mentioned conditions. The fusion product of different experiments since the start of the development of tokamaks is shown in figure 1.2.

In the following, the fundamental properties of moving charges and plasmas are outlined

before introducing the tokamak device and its physics.

Quasineutrality: First, we look how a large number of electrons behaves around a positive charge. Due to its comparatively large mass, the ion is assumed to be fixed in space, while the electrons assemble around it in a way to minimize the potential energy and thus, shield the central charge from the outside region. The electrons can escape from the potential of the ion at a certain length scale, where their kinetic energy becomes comparable to the potential energy. This length scale is called the **Debye length** $\lambda_{\mathbf{D}}$ and is determined by the temperature T and electron number density n_e :

$$\lambda_{\mathrm{D}} = \left(\frac{\varepsilon_0 \, k_B T}{n_e \, e^2} \right)^{1/2}, \tag{1.6}$$

where ε_0 is the dielectricity constant, k_B the Boltzmann constant and e the electron charge. At length scales below the Debye length, the effect of the single charges becomes important. Above, the charges are shielded and the plasma is considered to be quasi-neutral.

Motion in uniform magnetic fields: In the presence of electro-magnetic fields, charges experience a Lorentz force $\mathbf{F}_{\mathrm{L}}$ expressed by:

$$\mathbf{F}_{\mathrm{L}} = q \, (\mathbf{E} + \mathbf{v} \times \mathbf{B}), \tag{1.7}$$

where q is the charge of the particle, $\mathbf{E}$ the electric field, $\mathbf{B}$ the magnetic field and $\mathbf{v}$ the velocity of the charge. In a uniform magnetic field in the z direction $\mathbf{B} = B_z \, \mathbf{e}_z$, the equation of motion is the following:

$$m \, \frac{\mathrm{d}\mathbf{v}}{\mathrm{d}t} = q \, \mathbf{v} \times \mathbf{B} \tag{1.8}$$

$$\Rightarrow \mathbf{v} = \begin{pmatrix} v_\perp \cos(\omega t) \\ v_\perp \sin(\omega t) \\ v_\parallel \end{pmatrix}, \tag{1.9}$$

where q is the charge of the particle, m its mass and $\mathbf{v}$ its velocity. This tells us that the charge gyrates around the magnetic field with the cyclotron frequency $\omega = \frac{qB_z}{m}$ and the velocity $v_\perp$ in the plane perpendicular to $\mathbf{B}$. In the parallel direction, the charge moves unaffected by the magnetic field with the velocity $v_\parallel$. Integrating the perpendicular component of $\mathbf{v}$ over time, we find the gyration radius, called **Larmor radius**:

$$r_L = \frac{v_\perp}{\omega} = \frac{m v_\perp}{q B_z}. \tag{1.10}$$

The direction of the gyration depends on the sign of the charge and aims to reduce the external magnetic field $\mathbf{B}$, which means that the motion is **diamagnetic**.

Particle Drifts: In nonuniform magnetic fields or when external forces are present, the

movement becomes more complicated. An additional force $\mathbf{F}$ will result in a drift motion perpendicular to both the force and the magnetic field with the velocity

$$\mathbf{v}_{\text{drift}} = \frac{\mathbf{F} \times \mathbf{B}}{qB^2}. \tag{1.11}$$

This motion is superimposed on the gyration orbit, so that that the trajectory is composed of the gyration and the additional drift. The following drifts are relevant for our application. An electric field $\mathbf{E}$ with a component perpendicular to the magnetic field in the configuration above results in the $\mathbf{E} \times \mathbf{B}$ **drift** with the velocity:

$$\mathbf{v}_{\mathbf{E}\times\mathbf{B}} = \frac{\mathbf{E} \times \mathbf{B}}{B^2}. \tag{1.12}$$

Note that the direction of the drift is independent from the sign of the charge. In nonuniform magnetic fields, the gradient acts on the magnetic moment of the gyrating charge. This results in a $\boldsymbol{\nabla} B$**-drift** with the velocity

$$\mathbf{v}_{\boldsymbol{\nabla} B} = -\mu \frac{\boldsymbol{\nabla} B \times \mathbf{B}}{qB^2} = -mv_\perp^2 \frac{\boldsymbol{\nabla} B \times \mathbf{B}}{2qB^3}, \tag{1.13}$$

where $\mu = \frac{mv_\perp^2}{2B}$ is the magnetic moment of a gyrating charge. Apart from the gradient, the curvature of the magnetic field can cause a similar drift due to the centrifugal force $F_c = \frac{m\, v_\parallel^2}{R_C}$. The curvature radius R_C can be written in terms of $\boldsymbol{\nabla} B$ with $\frac{1}{R_\text{c}}\, \mathbf{e}_\text{R} = -\frac{\boldsymbol{\nabla} B}{B}$, where $\mathbf{e}_\text{R}$ the radial direction from the center of the curvature. This leads to the expression:

$$\mathbf{v}_{\text{R}_\text{c}} = -m\, v_\parallel^2 \frac{\boldsymbol{\nabla} B \times \mathbf{B}}{qB^3}. \tag{1.14}$$

Finally, leaving the single particle picture for a moment, there is a drift due to the collective motion of the particles. In a fluid, the collection of particles experiences a force from a pressure gradient $\boldsymbol{\nabla} p$, which results in the so called **diamagnetic drift**:

$$\mathbf{v}_\text{d} = \frac{\boldsymbol{\nabla} p \times \mathbf{B}}{nqB^2}, \tag{1.15}$$

where n is the number density. The equations above describe the motion of single charges in presence of fields, except for the diamagnetic drift, which is a collective effect.

The motion of a collection of particles can be described by the **kinetic equations**. Instead of describing the motion of individual charges, the probability density distribution f in phase space is evolved in time and modified by to collisions according to the following equation:

$$\frac{\mathrm{d}f}{\mathrm{d}t} = \frac{\partial f}{\partial t} + \mathbf{v} \cdot \boldsymbol{\nabla}_r f + \frac{\mathbf{F}_\text{L}}{m} \cdot \boldsymbol{\nabla}_v f = \left.\frac{\partial f}{\partial t}\right|_\text{collisions}, \tag{1.16}$$

where $\boldsymbol{\nabla}_{r,v}$ are the gradients of space and velocity, respectively, $\frac{\partial f}{\partial t}\big|_{\text{collisions}}$ is the change of the probability density due to collisions and $\mathbf{F}_{\text{L}}$ is the Lorentz force (1.7). The form of the collision operator depends on the assumptions on the nature of the collisions. In the case of no collisions between the particles, the right hand side becomes zero, which results in the Vlasov equation. If only direct binary collisions are taken into account, the equation is called the Boltzmann equation. The Fokker-Planck equation also includes the electromagnetic Coulomb interaction. The exact form of the operator is not relevant here, as we focus on an alternative description of the equations of motion.

The kinetic equations can describe the motion of particles, however, the calculation becomes numerically difficult for a large number of particles due to the high dimensional phase space 6N, with N being the number of particles, and the small length scales involved. The equations can be simplified by averaging over the gyroradius, as done in gyrokinetic models, and solved with particle in cell methods, for example. It is often sufficient to look at the average properties of the plasma for general stability considerations. Taking the moments of the velocity of equation (1.16), one arrives at a fluid description of the plasma. Together with additional assumptions and the non-relativistic, long wavelength Maxwell equations, a set of equations is obtained, which are called **magnetohydrodynamic (MHD) equations**. These equations are presented in section 2.1.

1.3 Magnetic confinement fusion

High plasma temperatures as well as high densities are required to reach fusion conditions and fulfill the ignition condition defined in equation (1.5). One approach to reach this goal aims to confine the plasma with magnetic fields. In the following, the configuration of one magnetic confinement fusion device, the tokamak, as well as the relevant physical effects are described. At the end of this section, the tokamak ASDEX Upgrade is introduced, as it is the device studied by the simulations in this thesis.

1.3.1 Tokamaks

When applying a magnetic field, charged particles follow the field lines in a gyratic motion, which makes it possible to enforce a direction on them. While choosing a toroidal configuration prevents end particle losses, it poses some challenges on the confinement of the plasma. The first toroidal devices were developed in Russia in the 1950s, where they were given the name **tokamak**, translated as toroidal fusion device. The research for this kind of machines has advanced enormously in the last decades as shown by the increasing fusion product and the temperatures achieved by different experiments in figure 1.2. In particular, the largest tokamak so far is currently under construction in the south of France, called ITER, as a proof of principle that a tokamak can reach reactor conditions with $Q \geq 10$. Another promising geometry for toroidal magnetic confinement, the stellarator, uses complex 3D fields to confine the plasma, whereas tokamaks are almost toroidally symmetric. The standard textbook of [Wes11] provides a broad overview of tokamak related physics, while other plasma physics text books such as [Che16, Fre14] also contain information about tokamaks.

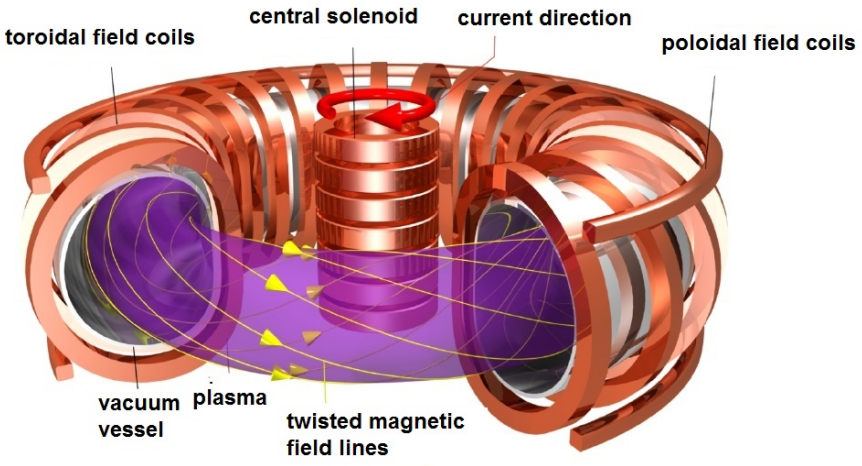

Figure 1.3: The toroidal field coils create the main toroidal field in the plasma of a tokamak, while the central solenoid induces the toroidal plasma current, which gives rise to the poloidal magnetic field component. The additional poloidal magnetic field coils control the shape and position of the plasma. (adapted from [Tok])

The main magnetic field in the toroidal direction B_ϕ is in a range of 2 to 10 T and is produced by **toroidal field (TF) coils**, which are located in the poloidal plane as shown in figure 1.3. In section 1.2, it was explained how particles in a curved, nonuniform magnetic field experience a drift perpendicular to the gradient of the toroidal field according to equation (1.13). The resulting motion is in upward direction for ions and downward for electron, which creates a vertical electric field due to the separation of charges. The resulting, charge independent $\mathbf{E} \times \mathbf{B}$ drift (1.12) leads to an outward radial motion of both electrons and ions. This means that confinement in a torus by a purely toroidal magnetic field is not possible. Instead, a poloidal magnetic field has to be superimposed on B_ϕ to prevent radial losses on a fast time scale. This poloidal component is introduced by means of a **toroidal plasma current** in the case of a tokamak. In stellarators, it is typically part of the 3D magnetic field, which has been optimized for confinement, with the consequence that the plasma is nearly current free.

The central solenoid acts as a transformer, with the second winding being the plasma itself, to induce a toroidal current I_p in the plasma. However, this sets a limit on the discharge time, as the coil current cannot be increased indefinitely. Therefore, other driving mechanisms for I_p such as the injection of energetic neutral particle beams or radiofrequency waves, which resonate with the electron or ion cyclotron frequency, have to be employed. Advanced tokamak operation will also rely on a toroidal current driven by radial pressure gradients in the plasma, the so called bootstrap current, to extend the discharge time. Typical discharges in present experiments last from seconds to a minute, while ITER discharges will last up to 8 min for $Q = 10$ scenarios and explore the possibility of a discharge duration of a quarter of an hour [Shi07]. The tokamak JT60-SA will soon start operation with the goal of supporting the research ITER and future power plants by investigating relevant discharge scenarios. Its steady state operations will have a typical discharge duration of ≈ 100 s [Gir17].

The toroidally symmmetric **poloidal field (PF) coils** control the plasma shape and position. They are distributed at different heights and radii around the plasma, and are in general located on the outside of the TF coils. Furthermore, a plethora of diagnostic coils, not shown in figure 1.3, with various geometries are placed close to the plasma to measure the components of the magnetic flux changes to obtain information about the plasma state. Also not shown here are additional saddle coils responsible for magnetic error fields.

The **vacuum vessel** is located inside the TF coils as shown in figure 1.3. It does not only contain the plasma and the vacuum, but also allows diagnostic and heating systems access to the plasma. The hot plasma region has to be prevented from coming into contact with the wall, which would lead to a dilution of the fuel and to radiation losses due to the accumulation of impurities. This is done by either a physical limiter or by controlling the plasma shape with magnetic fields. In the latter case, the plasma cross section has a form as shown in figure 1.4 with one or two so called **X–points**, where the poloidal magnetic field component is zero. The last closed flux surface (LCFS) separates the hot plasma region, where the

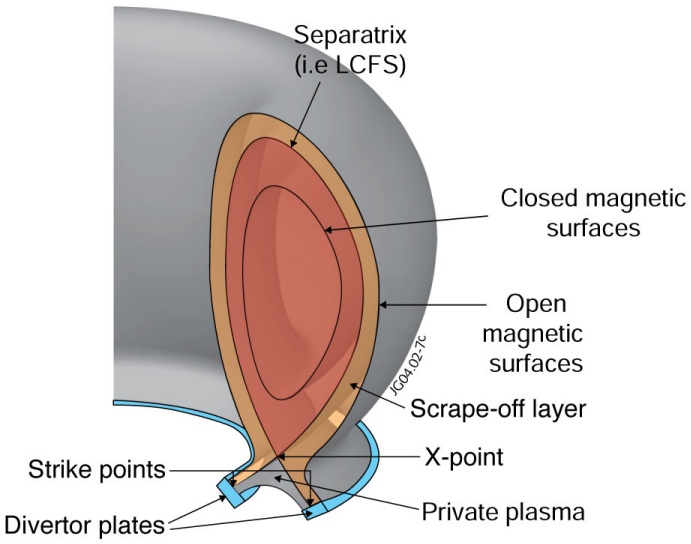

Figure 1.4: The cross section of a lower X–point plasma is shown, where the last closed flux surfaces divides the open field line region from the inner plasma. (taken from [Sha])

magnetic field lines close upon themselves, from the outer region, where the magnetic field lines move helically outward until they hit a limiting surface. In X–point configuration, the LCFS is named **separatrix**. The open field line region, in which the plasma is still present, is called the scrape-off layer (SOL). On the outside of the separatrix, the magnetic field is directed towards a metal surface, the **divertor** target plates. This configuration impedes the back flow of impurities, which are removed by a pumping system. Between the vacuum vessel and the LCFS, there are other structures like the divertor or heat shields, called the plasma facing components (PFC), which are designed to take up large heat loads to protect the outer structures and accommodate diagnostic systems.

During a discharge, currents can be generated in the components and the vessel, so that they have to be designed to withstand the forces due to the interaction with the magnetic field. These currents also allow a stabilization of certain instabilities by their feedback on the plasma. In cases, where the vessel is located at a large distance from the plasma, large saddle coils have to be added to provide for stabilization.

1.3.2 Tokamak plasma properties

The **coordinate system** used for tokamaks, as shown in figure 1.5, is described by the **major radius** R pointing horizontally outward from the vertical axis, while the **minor radius** r defines the radial position with respect to the center of the plasma cross section with $r = a$ at the LCFS. The **poloidal** and **toroidal** angles are defined by θ and ϕ, respectively. The aspect ratio R_0/a indicates the importance of the toroidal effects.

In a tokamak equilibrium, the plasma forms closed surfaces defined by the magnetic field lines, on which the pressure is constant. The **safety factor** q describes the toroidal angle

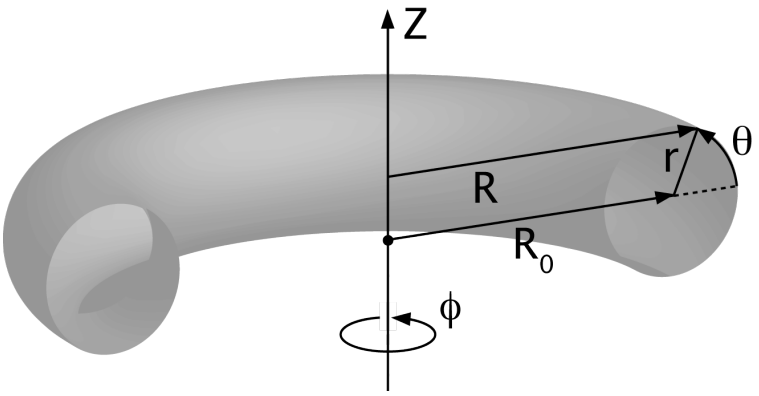

Figure 1.5: The toroidal coordinate system is used in tokamaks. (taken from [Coo])

$\Delta\phi$ after which a field line completes one full poloidal turn:

$$q = \frac{\Delta\phi}{2\pi}. \tag{1.17}$$

When a field line closes on itself after an integer number of poloidal and toroidal turns, the safety factor can be written as the ratio of m poloidal over n toroidal turns $q = \frac{m}{n}$. These surfaces are called **rational** surfaces and are susceptible to instabilities. A high safety factor is related to good MHD stability and some limits can be defined for the value of q at the edge as well as the core that trigger an instability when crossed. In an X–point configuration, the q–profile increases until it becomes infinite at the separatrix, where the poloidal magnetic field vanishes. The safety factor on the edge q_a can be written as

$$q_a = \frac{a^2 B_\phi}{\mu_0 I_p R_0} \tag{1.18}$$

for a circular cross section with radius a, plasma current I_p and major radius R_0.

The magnetic flux Φ is defined by the magnetic field $\mathbf{B}$, which passes through a surface of area S. The poloidal flux ψ is defined accordingly as the flux through a toroidal ribbon of area S:

$$\begin{aligned} \Phi &= \int_S \mathbf{B} \cdot \mathrm{d}\mathbf{S} \\ \psi &= \frac{1}{2\pi} \int_S \mathbf{B} \cdot \mathrm{d}\mathbf{S}. \end{aligned} \tag{1.19}$$

As poloidal surfaces of equal ψ are nested in equilibrium, it is convenient to describe the radial position as a function of the normalized poloidal flux ψ_N defined by the difference of flux on the boundary and the **magnetic axis**, the center of the nested surfaces, as

$$\psi_N = \frac{\psi - \psi_{\text{axis}}}{\psi_{\text{bnd}} - \psi_{\text{axis}}}. \tag{1.20}$$

The value of q at $\psi_N = 0.95$, denoted q_{95}, is often used as an important figure of merit for the fusion power and plasma stability because the safety factor is not defined on the separatrix.

Another figure of merit to describe the performance of fusion devices is the parameter β, indicating the efficiency of confinement of the plasma pressure by the magnetic field. It is defined by the ratio of average pressure and magnetic field pressure:

$$\beta = \frac{\langle p \rangle}{\langle B^2 \rangle / 2\mu_0}, \tag{1.21}$$

where μ_0 is the vacuum permeability. Often, the poloidal β_p is used, which is defined by the ratio of pressure over the poloidal magnetic field pressure:

$$\beta_p = \frac{\langle p \rangle}{\langle B_\theta^2 \rangle / 2\mu_0} \tag{1.22}$$

This quantity has a practical interpretation. For $\beta_p > 1$, the plasma is **diamagnetic** and reduces the toroidal vacuum field, otherwise, it is **paramagnetic**. The effect on the toroidal magnetic field can be seen in figure 1.6, where the magnetic field is decreased inside the plasma for $\beta_p > 1$ and increased for $\beta_p < 1$.

A high pressure is linked to a better plasma performance by increasing the fusion product (1.5). However, the Greenwald limit on the density and other onset conditions for large scale plasma instabilities restrict the operational range, so that the value of β is far below one during operation. If the density limit is violated, large scale instabilities can develop, which eject a large part of the energy during a short time and thus endanger the integrity of the device. Such an event, where a large part of the thermal energy is lost on a small time scale, is called a **major disruption**.

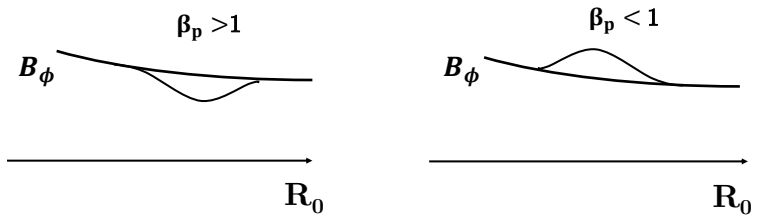

Figure 1.6: The plasma is diamagnetic if $\beta_p > 1$ reducing the vacuum toroidal field $\mathbf{B}_\phi$ and paramagnetic if $\beta_p < 1$. (adapted from [Wes11, p. 117])

It has been found advantageous to give the plasma a D shape by means of a quadrupole field in addition to the vertical field, both produced by the PF coils, to obtain better confinement and allow for higher densities. The total field is then the superposition of the poloidal field of the plasma current and the field of the PF coils as shown in figure 1.7. The poloidal cross section, shown in figure 1.8, can be characterized by the **elongation** κ, defined as the ratio

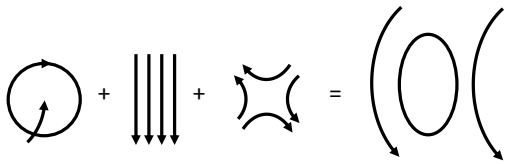

Figure 1.7: The poloidal field by the plasma current and vertical field of the PF coils are overlaid by an additional quadrupole field produced also produced by poloidal field coils in order to obtain a shaping of the plasma cross section. The total magnetic field is shown on the right. (own representation)

between the height $2b$ and the width $2a$ of the plasma cross section:

$$\kappa = \frac{b}{a}. \tag{1.23}$$

For lower/upper X–point plasmas, the vertical X–point position determines the lower/upper bound of the height. The triangularity characterizes the horizontal difference between the X–point and the geometric center of the cross section as shown in figure 1.8.

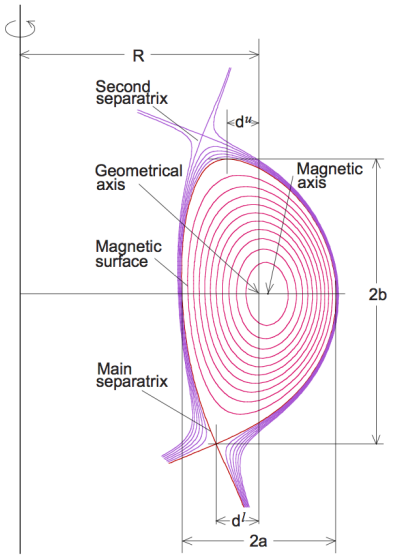

Figure 1.8: The shape of the cross section can be characterized by the triangularity and elongation. A D–shaped cross section has favorable properties for plasma performance. (taken from [Geo])

The shaping of the cross section, however, raises a problem with the **vertical stability** of the plasma and can lead to an uncontrollable vertical motion. The vertical instability is the main topic of this thesis, as it represents a major problem for the safe machine operation due to possible serious impact on the structures. The origin and implications will be discussed in section 1.4 after the introduction of the tokamak ASDEX Upgrade in the following section.

1.3.3 The tokamak ASDEX Upgrade

ASDEX Upgrade (AUG) is an example for a medium sized tokamak that started operation in 1990 as the successor of ASDEX, short for **A** **S**ymmetrical **D**ivertor **EX**periment, with the goal to find fusion reactor relevant discharges and contribute to the definition of potential operation scenarios for ITER. The machine and typical plasma parameters can be found in table 1.1. In figure 1.9, the setup of ASDEX Upgrade can be seen including the supporting structures, the coil system as well as the vacuum vessel with the antenna ports. The poloidal cross section in figure 1.10 shows part of the coil system, the plasma facing components and the vacuum vessel.

Table 1.1: Machine and plasma parameters of ASDEX Upgrade for a typical discharge [AUG].

Major radius R_0	1.65 m
Minor radius (horizontal) a	0.5 m
Minor radius (vertical) b	0.8 m
Elongation κ	1.8
Triangularity	0.4
Volume	14 m^3
Plasma mass	3 mg
Electron density	1×10^{20} m^{-3}
Plasma temperature	60-100 $\times 10^6$ K
Discharge duration	$\leq$ 10 s

The plasma facing components, consisting of the divertor on the top and bottom as well as a heat shield on the inboard side, are made of tungsten and are located closest to the plasma. Inside the TF-coils, the vacuum vessel made out of stainless steel can be found. It has holes to accomodate diagnostic ports as well as the heating antennas, which can be seen in figure 1.9.

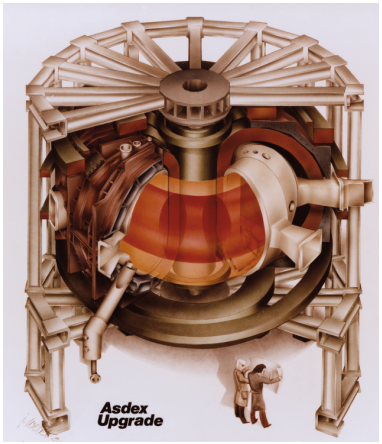

Figure 1.9: Configuration of ASDEX Upgrade including the supportive structures and ports. (taken from [Bil])

The coil system of the tokamak is especially important for this work, which will be described in the following. The coils needed for the plasma start up and operation are shown in figure 1.10 and their purpose was introduced in section 1.3.1. The transformer (OH) coil is located at the center of the torus and both responsible for the initial plasma heating and the induction of the toroidal plasma current. The toroidal field coils, surrounding the vaccuum vessel, are poloidally shaped and produce the main toroidal field. Furthermore, poloidal field (PF) coils, a **p**assive **s**tabilising **l**oop (PSL) and small OH coils are part of the system. Additional diagnostic coils and coils for applying magnetic perturbations (RMP coils) are not shown here.

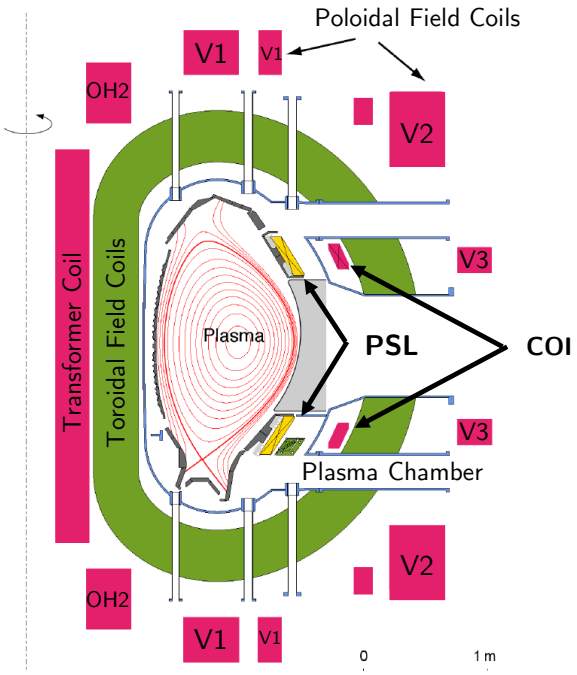

Figure 1.10: The main parts of the coil system as well as the vacuum vessel and plasma facing components in the poloidal cross section of AUG are shown. (adapted from [Bil]).

The PF coils create a vertical field component, which is necessary for the radial plasma equilibrium, as well as a quadrupole field for the shaping of the cross section. In figure 1.7, it can be seen how the combination leads to a curvature of the magnetic field lines. This is done by the V1–V3 PF coils in ASDEX Upgrade, which are distributed on the top and bottom side of the system as well as on the outboard side.

The plasma position and shape can vary during the discharge because of disturbances or MHD instabilities, making an active control system necessary to maintain the equilibrium state. The control system acts on the CoI coils, located between the vacuum vessel and the TF coils, for the fast vertical position control, as they are closest to the plasma. For the position and shape control on a longer time scale, the V1–V3 coils are used. The details of the vertical control system are described in the section 2.3.3.

Since the vacuum vessel, also needed for the stabilization of some instabilities, is located at

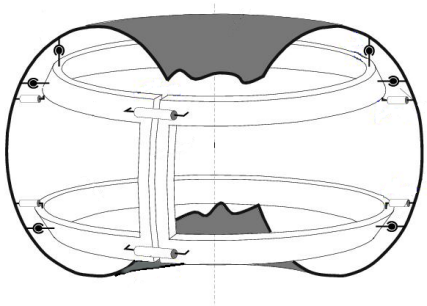

Figure 1.11: The PSL consists of two, not fully closed, copper rings which are connected by a bridge. (adapted from [Upg])

a relatively large distance in ASDEX Upgrade to allow for more flexibility for the placement of other structures [Gru93b], it is not well coupled to the plasma. This is different from most other tokamaks including ITER, where a closely fitting wall is planned. Therefore, a large saddle coil, the PSL, highlighted in yellow in figure 1.10, is installed inside the vacuum vessel. The PSL consists of two loops made of copper, shown in figure 1.11, on the upper and lower side of the vessel, which are connected by a bridge, so that the currents in the lower and upper part are anti-parallel and it only reacts to the net flux change of the plasma. It has a resistance of effectively 23 µΩ and an inductance of 13.2 µH [Upg]. The loops are not closed on itself, but separated by a small, well isolated gap. The main task of the PSL is the stabilization of the vertical movement of the plasma, which occurs due to the plasma elongation as explained in the following section.

1.4 Vertical Displacement Events (VDEs)

The elongation of the plasma is created by the poloidal field coils located outside the vacuum vessel. Their quadrupole field is superimposed on the poloidal magnetic field of the plasma current and the vertical dipole field as shown in figure 1.7. While the shaping is needed for better plasma performance, it has serious implications on the vertical stability of the plasma column, as the interaction of the nonuniform magnetic field with the plasma enhances perturbations from the equilibrium position. The net vertical force on the plasma is zero until it is displaced from its equilibrium position Z_0, where a net vertical force acts on the plasma due to the radial component of the magnetic field shown in figure 1.7.

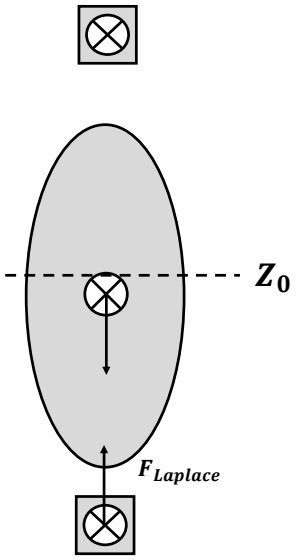

Figure 1.12: Laplace force due to the PF coils.
(own representation)

This can also be viewed from a more intuitive perspective. When a small displacement in the vertical direction occurs, the force balance is perturbed and the plasma experiences an attractive force in the direction of the initial perturbation by the Laplace force of the coils as shown schematically in figure 1.12. In vacuum, this instability would occur on the time scale of µs, on which any active control system fails. To mitigate this fast vertical motion, the plasma is placed inside a closely fitting, conductive shell, which slows down the motion by induced eddy currents in the wall. In some tokamaks, the wall is located at a large distance from the plasma, so that additional conductors are added for vertical stability, like in ASDEX Upgrade. This reduces the time scale to the resistive decay time of the eddy currents in the conductive structures. At this time scale of hundreds of ms, it is possible to implement an active stabilization system, which acts on the poloidal field coils to re-establish the vertical force balance.

The control system can fail in certain situations due to a system failure, or when the limits of the power supply system are exhausted. This leads to a vertical motion of the plasma column until it comes into contact with a limiting surface and the plasma energy is rapidly lost. This event is called a **Vertical Displacement Event (VDE)**.

MHD theory introduces a set of stability criteria on the pressure, the density and the current. A tokamak often operates close to these limits to obtain better plasma performance. However, this makes the occurrence of MHD instabilities more probable. In some cases, they can lead to a **disruption**, an event where a large portion of the energy is lost on a short time scale. As a result of the fast temperature decrease, the **thermal quench**, the current reduces rapidly during the **current quench**, which triggers a fast vertical, in most cases also uncontrollable, motion of the plasma. This is another source of VDEs. As the plasma

has a lower temperature, when it touches a limiting surface, this type of VDE is sometimes referred to as cold VDE or Vertical Displacement (VD), while the first type is named hot VDE.

VDEs are a major issue for large tokamak devices, as it imposes strong heat loads on the plasma facing components as well as large forces on the conductive structures. In case of non-axisymmetric VDEs, the electro-magnetic forces and thermal energy can be strongly toroidally localized, which leads to large horizontal forces and material damage. The theory and consequences of VDEs will be described in detail in section 2.2.2 in the second chapter of this thesis.

1.5 Scope of the thesis

Disruptions and VDEs pose a major threat for long term tokamak operation as it is foreseen in fusion power plants because of their potential fatal damage to the device. Thus, it is essential to understand the physics behind these events in order to avoid them completely or mitigate their consequences. Reliable computer simulations allow to understand the dynamics and underlying effects, which take into account all relevant physical phenomena as well as the geometry of the problem.

This thesis investigates the dynamics of VDEs in the tokamak ASDEX Upgrade, using the code framework of JOREK and STARWALL. JOREK [Huy07, Hoe20] is a non-linear, extended MHD code that solves the MHD equations in realistic tokamak geometry. The effects of a resistive wall and coils can be modelled with STARWALL [Mer15]. The two codes are coupled by suitable boundary condition [Hö12] in JOREK. Investigations of VDEs with JOREK and STARWALL have already been carried out in [AS18], benchmarked against other codes in [Kre20] and most recently with 3D VDEs in [Art20c]. Simulations of VDEs in ASDEX Upgrade with other codes have already been performed by [Wig11, Nak02, Seh16] and several others [Pau11b]. This thesis extends the previous simulation work of vertical displacement events by including the structures of AUG and introduces an active feedback system in JOREK to control the vertical position of the plasma.

In chapter 2, the relevant background is introduced consisting of the presentation of the MHD equations in section 2.1 as well as the theory and experimental observations of VDEs in section 2.2. For the active stabilization, a short background of control theory and its application to the vertical stability problem in tokamaks is given in section 2.3. The non-linear MHD code JOREK and the code, which models the resistive structures, STARWALL are introduced in section 2.4. Chapter 3 includes the description of the simulation setup in section 3.1, the modelling approaches for the PSL in section 3.2 as well as the implementation of the control system in JOREK in section 3.3.

Chapter 4 presents the main results of this thesis. One particularity of ASDEX Upgrade is the large passive loop, which is the main stabilizing factor of the vertical instability. Thus, it had to be shown first, that the passive coils in JOREK-STARWALL work correctly by

carrying out various validation tests for axisymmetric coils. The results of this are shown in section 4.1. A benchmark with the linear MHD code CASTOR3D [Str16] is shown in section 4.2 to validate the influence of the PSL in AUG on the growth rate of the instability. Afterwards, the influence of the wall and the coil parameters on the VDE growth rate were investigated in section 4.3. In section 4.4, a controller of the vertical position, similar to the one employed in ASDEX Upgrade, was implemented and tested in JOREK. A thermal quench was then artificially induced by large transport coefficients to investigate the effect of different current quench rates on the dynamics of a 2D VDE evolution. The results are shown in section 4.5. Finally, 3D simulations of VDEs resulting from a thermal quench triggered by massive material injection were carried out in section 4.6. In the end, a summary of the results and an outlook to future work is given in chapter 5

2 Theoretical Background

Chapter 1 gave an overview about the fusion and plasma physics topics relevant for tokamaks and introduced vertical displacement events (VDEs) as a fundamental problem of today's devices. This chapter will provide the necessary background for the simulations of VDEs carried out in the work of this thesis.

This includes the introduction of the underlying equations for the description of plasma physical phenomena by the equations of magnetohydrodynamics and of the tokamak equilibrium properties in section 2.1. Also, the unavoidable vertical instability in tokamaks is presented more in detail followed by a discussion of the implications of VDEs and their connection to disruption events in section 2.2. Afterwards, the basics of control theory and its application to the vertical instability in tokamaks are introduced in section 2.3. Finally, the codes used for the numerical simulations, JOREK and STARWALL, are presented in section 2.4.

2.1 Magnetohydrodynamics

In order to understand the dynamics of a plasma, the kinetic equations introduced in section 1.2 can be solved. However, following the evolution of the probability density function f is computationally expensive, as the full kinetic equations reside in the 6N dimensional phase space. Furthermore, the large scale behavior of the system is sufficient for the description of some phenomena of interest like large scale plasma instabilities. Thus, one approach to deal with the complexity of the problem is to average over the particles to deduce macroscopic properties. The set of equations for a plasma obtained by this method is called **magnetohydrodynamic** (MHD) equations, as they model the plasma like a fluid that is also subjected to electro-magnetic forces.

In the following, the fundamental equations are introduced in one of their simplest forms, before describing the MHD equilibrium properties in a tokamak following the outline of the standard textbooks [Goe04] and [Fre14].

2.1.1 Equations

The MHD equations can be derived by taking the velocity moments of the kinetic equation (1.16), which describes the time evolution of the probability density function in phase space due to external fields and collective behavior, and by introducing closure relations for the collisional terms. The MHD equations exist in different variants, which can be distinguished by the physical effects they include. In ideal MHD, for example, the resistivity of the plasma is neglected, which gives rise to special properties, some of which are mentioned below. More complex models treat the electrons and ions as two separate fluids, contain the effect of radiation, dissipation or the anisotropy of heat and particle transport.

Here, the resistive MHD equations are presented to show the principle structure of the equations.

$$\frac{\partial \rho}{\partial t} + \boldsymbol{\nabla} \cdot (\rho \mathbf{v}) = 0 \qquad \text{(continuity equation)} \tag{2.1a}$$

$$\rho \frac{\partial \mathbf{v}}{\partial t} + (\mathbf{v} \cdot \boldsymbol{\nabla})\mathbf{v} = \mathbf{J} \times \mathbf{B} - \boldsymbol{\nabla} p \qquad \text{(momentum equation)} \tag{2.1b}$$

$$\frac{\partial p}{\partial t} + \gamma p \boldsymbol{\nabla} \cdot \mathbf{v} + \mathbf{v} \cdot \boldsymbol{\nabla} p = (\gamma - 1)\eta \mathbf{J}^2 \qquad \text{(energy equation)} \tag{2.1c}$$

$$\boldsymbol{\nabla} \times \mathbf{E} = -\frac{\partial \mathbf{B}}{\partial t} \qquad \text{(Faraday's law)} \tag{2.1d}$$

The fluid quantities are the mass density ρ, the velocity $\mathbf{v}$ and the pressure p. Compared to purely hydrodynamic equations, the magnetic field $\mathbf{B}$, the electric field $\mathbf{E}$, the current density $\mathbf{J}$ and the resistivity η are included in the model. The energy equation contains the equation of state $p = cn^{-\gamma}$ with the adiabatic index γ.

The current is defined by Ampère's law, where the displacement current was dropped, and the electric field is given by Ohm's law:

$$\boldsymbol{\nabla} \times \mathbf{B} = \mu_0 \mathbf{J} \qquad \text{(Ampère's law)} \tag{2.2a}$$

$$\mathbf{J} = \sigma(\mathbf{E} + \mathbf{v} \times \mathbf{B}), \qquad \text{(Ohm's law)} \tag{2.2b}$$

with the conductivity $\sigma = \eta^{-1}$. Finally, the divergence freeness of the magnetic field has to be fulfilled:

$$\boldsymbol{\nabla} \cdot \mathbf{B} = 0. \tag{2.3}$$

The MHD equations (2.1) can also be written in the conservative form, where it becomes apparent that they represent a set of conservation equations for mass, density and energy.

A number of assumptions have to be made in order to derive the equations above. First, the system is assumed to be collision dominated, which ensures that the fluid approximation is valid and we can average over a fluid element. This is not strictly true in the case of fusion plasmas, which are mostly collisionless. However, it has been found that MHD is still a good description for most phenomena of interest as discussed in [Fre14, ch. 2]. Second, the time and length scales of interest must be large enough to allow for averaging over the elements. This is true if the size of the system is much larger than the Larmor radius and if the typical MHD timescale, related to the Alfvén speed v_a, is much larger than the cyclotron frequency:

$$\lambda_{\mathrm{MHD}} = a \gg R_i \qquad \tau_{\mathrm{a}} = \frac{a}{v_a} \gg \Omega_i^{-1}, \tag{2.4}$$

with $v_a = \frac{B}{\sqrt{\mu_0 \rho_0}}$ and a being the typical size of the system. The Alfvén speed v_a is the phase velocity of magnetohydrodynamic waves, which can be derived from the MHD equa-

tions (2.1). Combining Ampère's (2.2a) and Faraday's law (2.1d), the **induction equation** for the magnetic field is obtained:

$$\partial_t \mathbf{B} = \eta \boldsymbol{\nabla}^2 \mathbf{B} + \boldsymbol{\nabla} \times (\mathbf{v} \times \mathbf{B}), \tag{2.5}$$

which defines the evolution of the magnetic field over time.

In the case of ideal MHD, the resistivity of the plasma is zero, so that the first term on the RHS side of equation (2.5) vanishes, which leads to an important property. The flux, defined as the magnetic field that passes through a certain area $\mathbf{S}$:

$$\begin{aligned} \Phi &= \int_{\partial S} \mathbf{B} \cdot \mathrm{d}\mathbf{S} \\ \partial_t \Phi &= 0 \quad \text{if } \eta = 0, \end{aligned} \tag{2.6}$$

is constant in time in ideal plasmas. As a consequence, the field lines are convected with the fluid. They are, so to say, "frozen in" the plasma. Because of this coupling to the fluid motion, the field line topology cannot change in ideal plasmas. Only when the resistivity is finite, the field lines can break up and reconnect.

Having thus defined the equations of magnetohydrodynamics, we will continue with the equilibrium properties of a tokamak plasma.

2.1.2 Equilibrium

In equilibrium, the force balance equation (2.1b) reduces to a balance equation between the pressure gradient and the Lorentz force:

$$\mathbf{J} \times \mathbf{B} = \boldsymbol{\nabla} p. \tag{2.7}$$

Taking the dot product of this equation with the magnetic field, we see that the pressure is constant along the magnetic field $\mathbf{B} \cdot \boldsymbol{\nabla} p = 0$. Thus, the plasma consists of nested surfaces of constant pressure defined by the helical field lines, the **flux surfaces**. Repeating this with $\mathbf{J}$, we can see that the current is tangent to the flux surface, as $\mathbf{J} \cdot \boldsymbol{\nabla} p = 0$. This motivates the use of flux coordinates for the position in a tokamak $(R,Z,\phi) \rightarrow (\psi,\theta,\phi)$, where θ is the poloidal and ϕ the toroidal angle, while ψ is the poloidal flux. With this, the pressure can be expressed as a function of the poloidal flux $p = p(\psi)$.

Using the force balance equation (2.7) together with Ampère's law (2.2a) to obtain an expression for the current in terms of the magnetic field, an equation for the equilibrium can be derived (see for example [Fre14, ch. 6.2]), called the **Grad-Shafranov** equation:

$$\Delta^* \psi \equiv R \partial_R \left(\frac{1}{R} \partial_R \psi \right) + \partial_{zz} \psi = -\mu_0 R^2 \frac{\mathrm{d}p}{\mathrm{d}\psi} - \frac{\mathrm{d}F^2}{\mathrm{d}\psi}, \tag{2.8}$$

where ψ is the poloidal flux, R the major radius and $F(\psi)$ is defined as $F = RB_\phi$.

A toroidal device needs both toroidal and poloidal magnetic fields to be in a steady state equilibrium as shown in section 1.3.2. The radial equilibrium has already been discussed in the particle picture, but it is also instructive to look at this problem from a macroscopic perspective as done in [Fre14, chapter 4.8] or [Igo15], for example.

Due to the toroidicity, the toroidal magnetic field decreases with the major radius with $\mathbf{B}_\phi \propto \frac{1}{R}$. Thus, the inboard side is called the **high field side (HFS)**, while the outboard side is the **low field side (LFS)**. The plasma experiences the so called *hoop force* due to the radial decrease of the toroidal magnetic field, which is proportional to the difference in the magnetic field strength times the area S on the outboard and inboard side respectively:

$$F_R \propto (B_o^2 S_o - B_i^2 S_i).$$

The larger area on the LFS cannot compensate due to the quadratic dependence of the magnetic field, resulting in an outward force. Also, there is a net force in major radial direction due to the different pressure and area sizes on the inboard and outboard side of the torus $F_R = (p_o S_o - p_i S_i)$, called *tire tube force*. The action of the plasma on the magnetic field is diamagnetic in most cases, thus, as shown before in figure 1.6, the toroidal field is partially cancelled inside the plasma region. This results in a net outward *(1/R)*-force in addition to the hoop and tube force.

These effects can be compensated by a perfectly conducting wall, compressing the field lines on the outboard side until there is a balance of pressures. Since walls in experiments have a finite resistance, a different method has to be chosen. Instead, the radial outward force is balanced by a vertical field B_v. This field is created by poloidal field coils, which interact with the toroidal plasma current J_ϕ by the Lorentz force

$$F_R = -J_\phi B_v \tag{2.9}$$

to balance the radial outward forces. In the large aspect ratio limit, the vertical magnetic field of the coils required for this balance can be written as [Wes11, ch. 3.8]

$$B_v = -\frac{\mu_0 I_p}{4\pi R_0}\left(\ln\frac{8R_0}{a} + \Lambda - \frac{1}{2}\right), \tag{2.10}$$

with R_0 and a being the major and minor radius respectively. The quantity Λ depends on the poloidal beta β_p and on the **internal inductance** l_i of the plasma. The latter is a measure for the peakedness of the current profile and defined below.

Λ and l_i are defined as:

$$\Lambda \equiv \beta_p + \frac{l_i}{2} - 1 \tag{2.11}$$

$$l_i \equiv \frac{\langle B_\theta^2 \rangle}{B_\theta^2(a)} = \frac{2\int_0^a B_\theta^2 r \, \mathrm{d}r}{a^2 B_\theta^2(a)} \approx 2V \frac{\langle B_\theta^2 \rangle}{\mu_0^2 I_p^2 R}, \tag{2.12}$$

where B_θ is the poloidal magnetic field, mainly produced by the toroidal plasma current, a is the minor plasma radius and β_p is the ratio between the pressure and magnetic pressure of the poloidal field defined in equation (1.22). The internal inductance l_i can be approximated by the expression on the right as shown in [Hen07], where V is the plasma volume.

As long as these conditions are fulfilled, the plasma is in radial equilibrium. However, we also need to consider the vertical stability of the plasma column, which gives rise to a different challenge. In elongated configurations, the plasma is vertically unstable, so that active control is required to maintain the steady state position. In situations, where the MHD stability limits are violated, the control limits can be exceeded, leading to a plasma movement into the wall. The physical background and implications of vertical displacement events are laid out in the next section.

2.2 Vertical Displacement Events

The basic problem of vertical stability and its implications on safe tokamak operation were introduced in section 1.4 and is discussed more in detail in this section. In section 2.2.1, the vertical stability of a current loop in an external field is analyzed as a simplified model of a tokamak and later extended to the real system in section 2.2.2. Also, the onset and implications of vertical displacement events are described in section 2.2.3. Finally, a short overview about asymmetric VDE effects is given in section 2.2.4.

2.2.1 The three wire model

Before going into the physics in a complicated geometry, it is instructive to look at a simplified model of the plasma and the surrounding coil system, the **three wire model**. It can be used to describe the vertical stability of a tokamak as it is done for example in [Kik12, p. 244ff] and [Wig11] or to design a feedback stabilization system [Jar82]. It represents, however, a strongly simplified model, which neglects the current distribution in the plasma, the variation of the total current as well as the deformation of the plasma cross section and assumes a perfect vacuum around the plasma.

The model consists of three co-planar wires as shown in figure 2.1, where the center loop represents the plasma, carrying the fixed current I_p, and is free to move in the vertical direction. Whereas the other two loops are passive coils without current or voltage source located at a fixed position. The setup is in steady state with an equilibrium magnetic field until the position of the center loop is perturbed. A coil set with constant currents, which is not shown in figure 2.1, creates the nonuniform background field of the form as shown in figure 1.7, with a zero radial component at the equilibrium position of the plasma coil. At the position $z = 0$, the net force onto the plasma loop is zero.

When the center loop is perturbed from its equilibrium position by $\mathrm{d}z$, it experiences a destabilizing Laplace force $F_{z,d}$ on the current carrying plasma wire with radius R_0 due to the background magnetic field:

$$\mathrm{d}\mathbf{F} = I_p \, \mathrm{d}\mathbf{l} \times \mathbf{B} \tag{2.13a}$$

$$F_{z,d} = 2\pi R_0 I_p B_r = 2\pi R_0 I_p \frac{\partial B_r}{\partial z} \, \mathrm{d}z, \tag{2.13b}$$

where $\mathrm{d}\mathbf{l}$ represents a segment of the plasma loop and B_r is the external magnetic field, which is Taylor expanded around the equilibrium position and is zero at $z = 0$. The magnetic field has to fulfill the condition $I_p \frac{\partial B_r}{\partial z} > 0$, resulting in a destabilizing force.

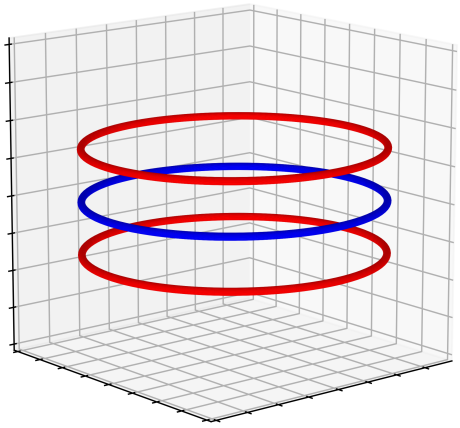

Figure 2.1: The plasma can be seen as a current carrying loop for analyzing the basic vertical stability properties of the system in a strongly simplified model. The conductive structures are represented by two passive loops in red located above and below the plasma loop. The setup is placed in a nonuniform magnetic field without net force on the plasma loop in equilibrium. (own representation)

The resulting flux change $\frac{\mathrm{d}\Phi}{\mathrm{d}t}$ from the motion of the current loop in a magnetic field induces a current I_c in the passive coils, which evolves according to the circuit equation:

$$\begin{aligned} \frac{\mathrm{d}\Phi}{\mathrm{d}t} &= -\mathcal{R}I_c - \mathcal{L}\frac{\mathrm{d}I_c}{\mathrm{d}t} \\ \text{with} \quad \frac{\mathrm{d}\Phi}{\mathrm{d}t} &= \frac{\mathrm{d}(M_{cp}I_p)}{\mathrm{d}t} = I_p\frac{\partial M_{cp}}{\partial z}\frac{\mathrm{d}z}{\mathrm{d}t}, \end{aligned} \tag{2.14}$$

where $\mathcal{R}$ is the resistance and $\mathcal{L}$ the self-inductance of the passive coils. The flux Φ can be expressed by the mutual inductance M_{cp} between the plasma loop and the passive coils multiplied by the plasma current I_p. The stabilizing force by the outer passive loops, creating the radial magnetic field

$$B_{r,coil} = -\frac{1}{R_0}\frac{\partial \psi_{coil}}{\partial z} = \frac{1}{2\pi R_0}\frac{\partial (M_{pc}I_c)}{\partial z}, \tag{2.15}$$

with $M_{pc} = M_{cp}$, can be expressed by:

$$F_{z,s} = I_p I_c \frac{\partial M_{pc}}{\partial z}. \tag{2.16}$$

The equation of motion of the center wire is then the sum of the stabilizing and destabilizing force:

$$m\frac{\mathrm{d}^2 z}{\mathrm{d}t^2} = I_p I_c \frac{\partial M_{pc}}{\partial z} + 2\pi I_p R_0 \frac{\partial B_r}{\partial z} z, \tag{2.17}$$

with m being the mass of the plasma loop. Without the stabilizing force of the passive loops, the center wire with a mass of the order of a gram would experience a force in the order of

MN, causing a movement on a time scale of ≈µs.

When applying an exponential ansatz on the position as well as on the currents of the passive coils ($z, I \propto e^{\gamma t}$), and inserting the coil current of equation (2.14) in the equation of motion (2.17) above, we obtain an equation for the growth rate γ:

$$m\gamma^2 = -\gamma \frac{I_p^2 (\partial_z M_{pc})^2}{\mathcal{R} + \gamma \mathcal{L}} + 2\pi I_p R_0 \frac{\partial B_r}{\partial z}. \tag{2.18}$$

It is practical to introduce the normalization constants

$$s = \frac{(\partial_z M_{pc})^2}{\mu_0 \mathcal{L} R_0}, \quad d = \frac{2\pi R_0^2}{\mu_0 I_p} \partial_z B_r \quad \text{and} \quad \gamma_0^2 = \frac{\mu_0 I_p^2}{R_0 m}, \tag{2.19}$$

motivated by the magnitude of the equilibrium vertical field introduced in equation (2.10), which is in the order of $\frac{\mu_0 I_p}{2\pi R_0}$. The constants s and d are related to the magnitude of the stabilizing and destabilizing force.

In the limit of a perfect conductor ($\mathcal{R} = 0$), the growth rate can be expressed as

$$\gamma = \gamma_0 \sqrt{d} \sqrt{1 - \frac{s}{d}}. \tag{2.20}$$

When the destabilizing force is bigger than the stabilizing one ($d > s$), the growth rate becomes real and positive, leading to a movement of the wire on an inertial time scale. This can be due to an insufficient coupling between the passive coils and the plasma loop or a large gradient of the background field, for example. Otherwise, if $d < s$, the plasma loop oscillates around its equilibrium position.

In case of resistive wires, the growth rate can be expressed by:

$$\gamma^{\star 2} + \gamma^\star \frac{s}{\gamma_c + \gamma^\star} - d = 0, \tag{2.21}$$

with the normalized growth rate $\gamma^\star = \gamma/\gamma_0$ and the normalized current decay constant $\gamma_c = \mathcal{R}/(\mathcal{L}\gamma^\star)$. The influence of the resistance can be seen in the plots in figure 2.2 of the normalized growth rate $\gamma^\star$ against the ratio of destabilizing and stabilizing forces for different resistances of the passive conductors.

This simplified model, as an example for a **rigid diplacement model**, already contains the basic vertical stability properties of a tokamak plasma. It shows that conductors with finite resistivity can reduce the time scale of the mode to the characteristic current decay time of the conductor and hereby allow control. Otherwise, the time scale of the motion is in the order of µs, which is beyond the reaction capability of any controller. The next section treats the vertical stability of a tokamak, which shows similar properties as the three wire model.

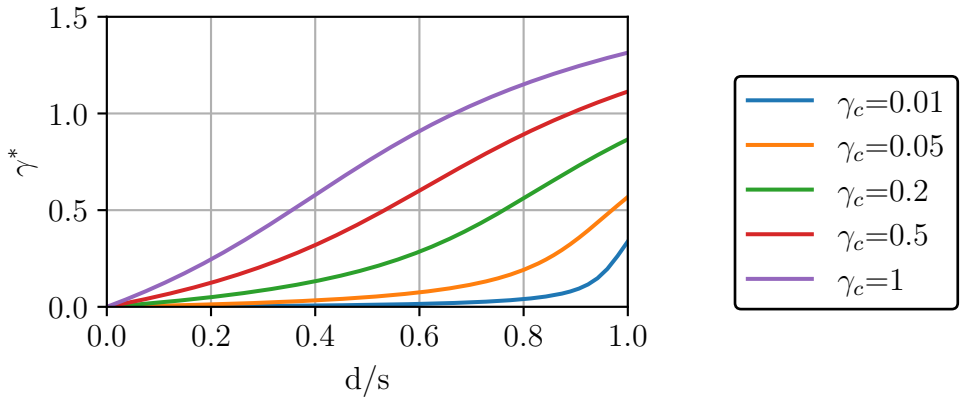

Figure 2.2: The normalized growth rate derived in equation (2.21) is shown depending on the ratio of destabilizing and stabilizing force (d/s) for different, normalized current decay constants γ_c of the passive loops. The resistance has a strong influence on the growth rate and low values can reduce the growth rate significantly. In contrast to an ideal conductor, the motion becomes unstable even if the ratio d/s is below 1.

2.2.2 Axisymmetric stability

Tokamak plasmas with non-circular cross sections are inherently unstable against a vertical perturbation as it will be shown in this section. If the resulting vertical motion is not stabilized in some way, the plasma moves into the surrounding structure, leading to high thermal loads and electro-magnetic forces. The origin of this instability is described in the following.

The shape and position of the plasma in a tokamak are determined by the poloidal field coils, introduced in section 1.3. They produce the quadrupole magnetic field, shown in figure 1.7, responsible for the a vertical elongation of the cross section associated with a better plasma performance, as it increases the stability limit for the pressure and the currents. In equilibrium, there is no net force by these coils because the upward and downward contributions compensate each other. However, when a small deviation from the equilibrium position occurs, the force balance is perturbed, causing an acceleration of the plasma column by the Laplace force in the direction of the initial perturbation. This is also shown schematically in figure 1.12. In the previous section 2.2.1, the same configuration is considered with the simplified three wire model, where the magnetic background field is the same as the one produced by the PF coils. The net vertical force by the vacuum field of the PF coils on the displaced plasma can be expressed by:

$$\mathrm{d}F_{\mathrm{destab}} = -2\pi R I_p \frac{\partial B_{r,\mathrm{vac}}}{\partial z}\,\mathrm{d}z = 2\pi I_p n B_{z,\mathrm{vac}}\,\mathrm{d}z, \tag{2.22}$$

where R is the plasma major radius and the field index $n = -\frac{R}{B_{z,\mathrm{vac}}}\frac{\partial B_{z,\mathrm{vac}}}{\partial R}$, a measure for the quadrupole moment, was used together with the relation between the vertical and radial

field $\partial_r B_{z,\mathrm{vac}} = \partial_z B_{r,\mathrm{vac}}$ derived from Ampère's law (2.2a) in vacuum. The vertical magnetic field given by equation (2.10) as well as the field index n determine the magnitude of the destabilizing force (2.22). Therefore, the poloidal β_p (1.22) and the internal inductance l_i (2.12) influence the growth rate via the dependence of $B_{z,\mathrm{vac}}$ on these parameters. For a given elongation, a smaller l_i reduces the required quadrupole moment, as it decreases the effective distance between the coils and the plasma. With $B_{z,\mathrm{vac}}$ being negative to satisfy the radial equilibrium, the criterion for vertical stability becomes [Miy16, ch. 16]:

$$n = -\frac{R}{B_{z,\mathrm{vac}}} \frac{\partial B_{z,\mathrm{vac}}}{\partial R} > 0. \tag{2.23}$$

For elongated plasmas, this value is always negative because $\frac{\partial B_{z,\mathrm{vac}}}{\partial R} < 0$. Therefore, **elongated cross sections are inherently vertically unstable** and need a combination of passive stabilization and active control to maintain steady state.

A displacement from the equilibrium position triggers stabilizing forces originating from different sources. First, a vertical movement induces **eddy currents** in the passive conductive structures surrounding the plasma, consisting of a closely fitting wall and optionally a large passive coil. Second, so called **halo currents** are generated outside the last closed flux surface, following a path through the scrape-off layer and wall as shown in figure 2.3. Both of these effects slow down the motion by creating vertical forces to balance the destabilizing force (2.22) by the PF coils.

The dominating effect is determined by the characteristic resistive time scales of the plasma, the halo and the wall currents,

$$\tau_p = \frac{\mu_0}{\eta_p} a^2, \quad \tau_h = \frac{\mu_0}{\eta_h} a \Delta_h \quad \text{and} \quad \tau_w = \frac{\mu_0}{\eta_w} a_w \Delta_w, \tag{2.24}$$

introduced in [Boo13], with $\eta_{p,h,w}$ being the resistivity of the plasma, the halo region or the wall, respectively. a is the plasma minor radius, a_w the wall minor radius and $\Delta_{h,w}$ the thickness of the halo region and wall, respectively. The time scale of the halo current is only valid in the limit of $\Delta_h \ll a$, which is not the case in the late phase of the VDE described in the following section.

When $\tau_w \gg \tau_h$, the effect of the induced **eddy currents** in the **encompassing conductive structures** dominates unless the distance between the wall and the plasma is too large to allow for sufficient coupling. For simplicity, the passive conductive structures, like the vacuum vessel and stabilizing coils, will also be referred to as the wall in the following. According to Lenz's law, the currents are directed in a way to inhibit the plasma motion by a magnetic field, resulting in a force with the magnitude:

$$\mathrm{d}F_{\mathrm{stab}} = -I_p^2 \left(\frac{\partial M_{cp}}{\partial z} \right)^2 \frac{\mathrm{d}z}{L_s}, \tag{2.25}$$

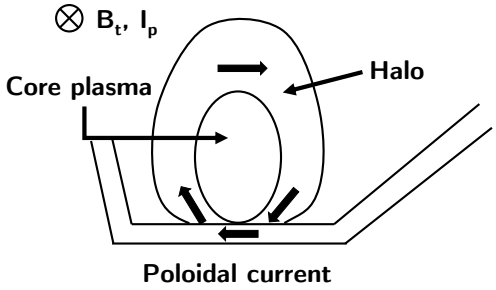

Figure 2.3: As the plasma moves downward, halo currents are induced due to flux conservation and the decaying plasma current. The currents flow along the magnetic field lines inside the scrape-off layer and along the path of the smallest impedance inside the wall. (adapted from [Hum99])

where M_{cp} is the mutual inductance between the plasma and the conducting structures, and L_s is the self-inductance of the wall or passive coils. The ratio between the stabilizing and destabilizing forces,

$$f = -\frac{\mathrm{d}F_{\mathrm{stab}}}{\mathrm{d}F_{\mathrm{destab}}}, \tag{2.26}$$

defines the stability reciprocal to the ratio d/s of the three wire model in section 2.2.1. The unstable region is found for $f \leq 1$, where the destabilizing force becomes larger than the stabilizing one, resulting in a movement on the Alfvénic time scale defined by equation 2.4. For f larger than 1, the motion takes place on the resistive time scale of the wall, on which the stabilizing eddy currents in the conducting structures decay. In ASDEX Upgrade, the ratio f has a value of approximately 1 because of the large plasma-wall distance. In order to increase this value, a passive saddle coil is added inside the vacuum vessel as presented in section 1.3.3, which increases f to $1.1 - 1.5$ [Gru93b]. Only the reduction of the growth rate by the presence of conducting structures as shown in the example of the three wire model allows the employment of a feedback stabilization system, consisting of a controller that acts on specific PF coils. These active coils restore the force balance and can lead the plasma back to its initial position. The working principle of the feedback system is described in detail in section 2.3.3.

When the force by the eddy currents is not sufficient to slow down the plasma, or the resistive time scales of the wall and parts the scrape-off layer (SOL) are similar $\tau_w \approx \tau_h$, **halo currents** are induced by the vertical motion of the plasma through the magnetic field. Because of the low pressure in the SOL, the currents are parallel to the magnetic field to fulfill the force balance equation (2.7), leading to the following relation [Gru93b]:

$$\begin{aligned} \mathbf{J} \times \mathbf{B} &= 0 \\ \Rightarrow q_h I_{\mathrm{halo},\theta} &= I_{\mathrm{halo},\phi}, \end{aligned} \tag{2.27}$$

with the local safety factor q_h of the halo region related to the pitch angle of the helical field lines.

Outside the last closed flux surface, in the scrape off layer, the magnetic field lines are not closed on themselves, but move helically into the wall. In the wall structure, the currents move along the path of smallest resistance in mainly the poloidal direction as shown in figure 2.3. This is due to the fact that, different from the SOL, the wall can take up forces, so that the force-free condition is not valid here. Strong halo currents can cause concern for the integrity of the device if the mechanical safety limits of the supporting structures are exceeded due to the electro-magnetic forces and thermal loads.

The force balance is modified by the additional vertical force from the halo currents, which is according to (2.13a): $F_{z,h} = B_\phi I_{\mathrm{halo},\theta} \Delta R$, where ΔR is the radial distance between the intersection points of the halo current with the wall. The force by the halo current due to the plasma motion is as strong as required to balance the vertical forces given by (2.22) and (2.25):

$$-F_{z,h} = F_{\mathrm{destab}} + F_{\mathrm{stab}}. \tag{2.28}$$

Let's assume that $F_{z,h}$ is too small to compensate for the net force on the RHS of the equation. Then, the plasma motion would accelerate and hereby drive larger voltages, increasing the halo currents until the total force in (2.28) is zero. For VDEs, other driving mechanisms of the halo currents become important, which will be discussed in the following section.

So far, the three wire model has been helpful to describe the vertical stability of the plasma. However, it reaches its limit, when taking into account halo currents and the following considerations. Rigid displacement models like the three wire model are often employed for stability analysis or the design of an active feedback stabilization system [Laz90]. However, it was found [War92, Seh16] that the plasma deformation plays a role for the vertical displacement, especially for high elongations and triangularities [Nak96a]. Also, the plasma current, the current distribution and the pressure are not constant during a VDE, which influences the coupling to the passive structures, and the destabilizing force. Effectively, this accelerates the vertical displacement. Therefore, the rigid displacement model only gives an estimate of the lower bound of the growth rate [Seh16], which can be estimated by the following relation as introduced in [Gru93b]:

$$\gamma_{RD} = \frac{1}{\tau_w} \frac{1}{f-1}, \tag{2.29}$$

where f is the ratio of stabilizing and destabilizing force defined in equation (2.26) and τ_w is the resistive decay time of the wall.

Here, the basic influences of the vertical stability of a tokamak plasma were reviewed. In the following, the mechanisms that lead to uncontrolled displacements as well as their dynamics are described.

2.2.3 VDE mechanisms

In the previous section 2.2, the problem of vertical stability was introduced, which is unavoidable in tokamaks with non-circular cross sections. As the stabilizing wall currents decay on their characteristic time scale, the plasma position has to be maintained by an active feedback system. However, situations may occur during operation, where the control limits are violated or the system fails. Two different scenarios play a role, where one is called a **hot VDE** and the other one is a **disruption** followed by a VDE.

First, we are going to look on the mechanism behind a hot VDE, where the plasma reaches the wall with almost its initial temperature and current, hence the name. The cause for this scenario can be the violation of the stability criterion (2.26) due to an excessive elongation, for example, or a failure of the control system, resulting in a fast vertical motion. The plasma then moves until it comes into contact with a limiting surface, leading to a reduction of the cross section area, as the outer layers are scraped off, while the edge current is re-induced in the plasma core with the total plasma current staying almost constant. When the area reduction is faster than the plasma current decay, the edge safety factor (1.18) decreases until it reaches the kink safety limit ($q \approx 2$) and a kink mode develops, which ultimately leads to a loss of confinement [Boo13, Hum99]. The mechanism behind the reduction of the safety factor is described in [Art20a]. This failure of the control system can be fatal, as the plasma still has most of its initial thermal energy and current upon reaching the wall, which results in high thermal loads on the plasma facing components. This type of VDE must be avoided to ensure safe operation.

Second, a VDE can follow after a **disruption**, a loss of confinement, with the advantage that the temperature is already significantly lower at the time of the wall contact. The mechanism behind this kind of VDE is shown in figure 2.4 and described in the following.

Operation close to the MHD stability limits or an unforeseen perturbation to the operation can cause a disruption, which leads to a rapid decrease of the thermal energy, called **thermal quench (TQ)**, on a time scale of ≈0.1 ms in ASDEX Upgrade and is estimated for ITER to be around 1 ms [ITE99]. This loss of thermal energy is due to a reconnection of the field lines, which break up from their nested structure, resulting in an enhanced heat and particle transport. At the same time, this leads to a flattening of the current profile, which leads to a characteristic spike in the plasma current of up to 10 % of its initial value like it is often observed during a disruption. Finally, the drop in pressure reduces the required vertical field for the radial equilibrium (2.10), causing an inward shift of the plasma column.

Following the thermal quench, the resistivity increases because of the lower temperature (with $\eta \propto T^{-1.5}$), which is the cause of the subsequent **current quench (CQ)** typically on a time scale from several ms [Gra96, Pau11a] up to hundred ms [Ric05]. The evolution of the thermal quench with a moderate current spike and the ensuing current quench is shown in an example in figure 2.5. This influences the vertical stability in two ways. If the current decay

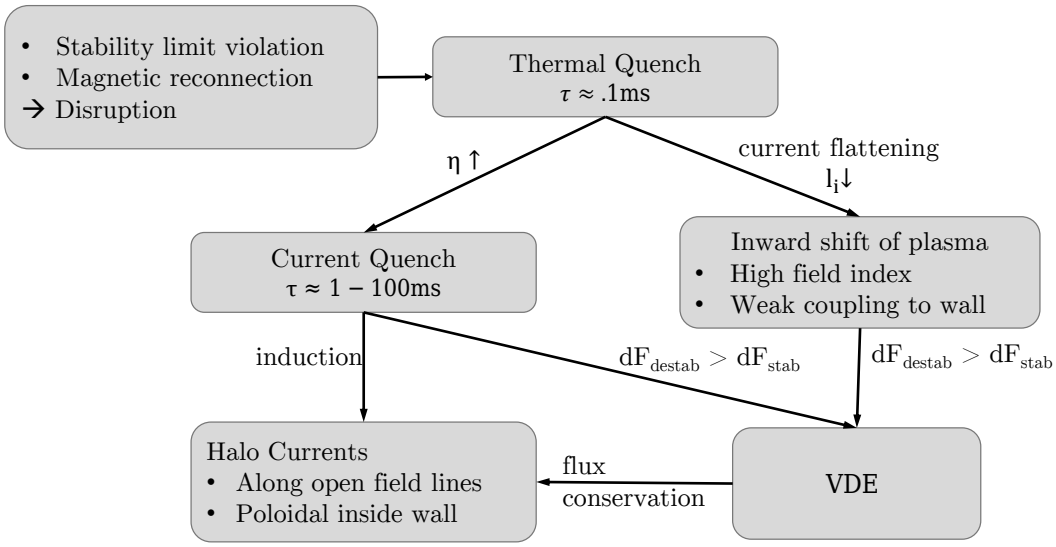

Figure 2.4: A violation of the MHD stability limits can cause a reconnection of the field lines resulting in a rapid loss of thermal energy. The plasma then moves inward due to pressure drop. The decrease of the temperature leads to a higher resistivity and a subsequent current decay. Finally, a VDE is triggered and halo currents are generated in the SOL. (own representation)

is too fast for scaling down the PF coil current, the destabilizing force $\propto I_p$ (2.22) decreases slower than the stabilizing force $\propto I_p^2$ (2.25). As a consequence, the stability ratio f defined by equation (2.26) decreases and crosses the stability margin after a time $t = \gamma_p \ln(1/f)$, where γ_p is the CQ rate defined by $\frac{\mathrm{d}I_p}{\mathrm{d}t} = \gamma_p I_p$ [Gru93a]. In addition, the plasma moves inward during the TQ to a region, which is in general related to a weaker coupling to the active coil feedback system as well as the stabilizing structures and is also associated with a higher field index n [Gru95]. Under these circumstances, the eddy currents in the wall and the active feedback system cannot stabilize the plasma in most cases, so that it moves vertically, usually in direction to the X–point.

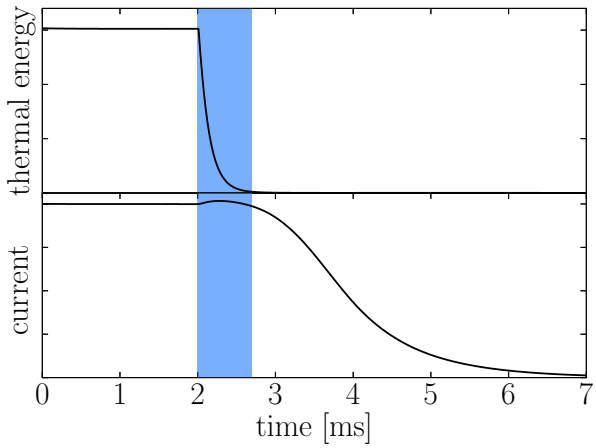

Figure 2.5: After the onset of the thermal quench, a spike in the plasma current can be observed before the current decays as a result of the enhanced resistivity. (own representation)

During both types of VDEs, **halo currents** are generated by various driving mechanisms, with one already introduced in the section 2.2.2. Despite the different VDE origins, the sources and evolution of the halo currents are similar for both hot and disruption induced VDEs. However, the complete mechanism behind the halo current drive has not yet been fully understood. A model of the creation of halo currents by circuit equations is presented in [Hum99]. Due to **flux conservation**, currents are induced in the scrape off layer (SOL) and on the plasma edge, when the plasma moves vertically. Because of the low pressure in this region, the halo currents in the SOL have to follow the helical magnetic field lines to ensure the force balance (2.27). Therefore, they can be induced by both toroidal and poloidal electrical fields. However, it seems that the large toroidal electric field produced by poloidal flux conservation is the main driving mechanism [Hum99]. In a later phase of the VDE, the plasma touches the wall, leading to current decay and shrinking of the cross section area, which enhances the halo current by **induction**. Furthermore, the field lines open up, when the closed flux surfaces come into contact with the wall, so that currents can flow along the field lines into the wall and SOL. They are "**convected**" from the core plasma. During the whole process, the plasma region is gradually replaced by the halo region.

In summary, halo currents arise from flux conservation due to the vertical motion in the magnetic field, the induction of current by the decaying plasma current and the scraping off of the plasma at the wall surface. It should be noted that the direction of the halo current originating from the current decay is in the same direction as the plasma current. Hence, it acts stabilizing and decreases the growth rate. This can be seen from the direction of the currents in figure 2.3.

In the following, further influences on the **dynamics** are analyzed. First, as described in section 2.2.2, the initial stability ratio determines the growth rate of the VDE by the elongation as well as other shape parameters of the plasma, the pressure, the internal inductance and the initial position [Seh16, Nak96a]. Also, the **current quench** influences the growth rate strongly [Nak96b, Gru93a]. In fact, it was shown in [Kir17] that in the ideal wall limit ($\tau_w \gg \tau_p$), the vertical position is a function of the plasma current only. Because the wall currents do not decay in this scenario, the plasma only moves to a new equilibrium position due to the change in current. When considering a resistive wall, a fast CQ enhances halo currents by induction due to the current decay as well as by the acceleration of the VDE as a result of the reduced stability ratio f. The CQ time is often defined by the linear current decay time:

$$\tau_{CQ,60} = \frac{t_{0.2} - t_{0.8}}{0.6}. \tag{2.30}$$

Additionally, as mentioned in section 2.2.2, effects due to the plasma deformation and changes in the current profile as well as the pressure can accelerate the vertical displacement. Finally, the shape and position of the wall play a role. On the one hand to allow a

close inductive coupling for eddy current induction. On the other hand, a top down asymmetric vessel makes it difficult to find a neutral point, the vertical position with the best stability properties [ITE99, Nak96b]. The negative effect by an asymmetric vessel is even enhanced as the asymmetric eddy currents can degrade the vertical field index n [Nak96b].

Regarding the **effects on the device**, VDEs can cause substantial damage to the machine structures. In case of hot VDEs, the plasma still carries most of its initial thermal energy at the time of wall contact, which exceeds the material limits of the plasma facing components. Additionally, halo currents exert a large electro-magnetic force in the vertical direction due to the interaction of its poloidal component with the toroidal magnetic field. These forces are naturally larger on the high field side due to the $1/R$ dependence of the magnetic field. The largest halo currents are found near the point of plasma-wall contact, while almost no currents are measured on the opposite side of the vessel [Pau11a], corresponding with the path of the halo currents shown in figure 2.3. To ensure safe operation, halo currents have to be limited to stay below the structural limits.

Due to the large electro-magnetic forces and thermal loads, the mechanisms and scaling of the halo currents have to be understood to develop mitigation strategies. In some experiments (e.g. in [Gra96]) and the analytical model in [Hum99], a scaling of the maximum halo current with the ratio of the plasma current and the edge safety factor I_p/q_a can be found. This provides an upper limit for the estimation of the halo current. Also, the efficiency of the halo current generation is related to the resistivity of the halo region. Therefore, to reduce the magnitude of the halo currents, the resistivity of the halo region can be increased by gas puffs, for example. The same method can be applied to induce a thermal quench and reduce the plasma current like it is done in practice to avoid hot VDEs, for example. In section 4.6, this method is applied in the simulation to study a thermal quench triggered by massive material injection followed by a VDE. It would be beneficial to slow down the initial displacement as far as possible, as the halo current is also related to the initial growth rate and the plasma current can decrease before the plasma comes into contact with a limiting surface [Hum99].

Another threat for safe operation, especially for large tokamaks, is the occurrence of so called **runaway electrons (RE)**, which are produced by different mechanisms [Bre19] and often occur after a disruption. The electric field created by the current quench accelerates electrons, with some reaching relativistic velocities. If this electric field is higher than a critical value, an avalanche of super thermal electrons is created resulting in a runaway effect. During the vertical displacement initiated by the CQ, this beam of energetic electrons moves with the plasma into the plasma facing components, where they can cause substantial damage. The current due to RE can be up to 70 % [Hen07] of the plasma current. Especially large tokamaks like ITER with a large plasma current are susceptible to the creation of runaway electrons.

This section showed the background of the onset of VDEs and gave an overview about its

dynamics. The avoidance of VDEs and mitigation of their effects including the associated halo currents are essential for a long term operation of tokamaks as it is foreseen in future power plants. Regarding the potential threat due to halo currents, the situation can get even worse, when an asymmetric component is introduced in the plasma and halo currents. The consequences are shown in the following section.

2.2.4 Asymmetric VDEs

Even when the onset of the vertical displacement event described in section 2.2.2 is axisymmetric, asymmetries can develop during its evolution. As explained in section 2.2.3, the shrinking of the plasma area during the wall contact reduces the edge safety factor if the area decreases on a faster time scale than the resistive decay of the plasma current. This leads to the development of a kink mode, when the safety factor reaches the kink safety limit, with the $n = 1$ mode presumably being the main factor responsible for the asymmetries of the halo currents. Other factors, like the machine asymmetries might also play a role. Especially dangerous is the interaction of this mode with the halo current, focusing large forces on small parts of the vessel and leading to a net horizontal force on the device [Fit11].

The asymmetry of the halo currents can be described by the toroidal peaking factor (TPF), defined as the ratio of the peak halo current to the toroidally averaged halo current:

$$\mathrm{TPF} = \frac{I_{\mathrm{h,max}}}{\langle I_{\mathrm{h}} \rangle_{\phi}}. \tag{2.31}$$

A high peaking factor concentrates the wall forces and thermal loads on one toroidal segment, which can pose a serious threat to the machine safety. Typical toroidal peaking factors are in the range of 1.2 to 2, but larger values have also been observed [ITE99]. The other factor determining the force on the wall is the magnitude of the halo current characterized by the halo fraction, the ratio between maximum halo current and pre-disruption plasma current:

$$\mathrm{HF} = \frac{I_{h,max}}{I_{p0}}. \tag{2.32}$$

The product of toroidal peaking factor and halo fraction is a measure for the maximum force on the vessel. For ITER, this value should satisfy $\mathrm{HF} \times \mathrm{TPF} \leq 0.75$ [Hen07] to ensure the integrity of the machine. In ASDEX Upgrade, the halo fraction is particularly high compared to other machines, with a value of HF up to 50 % [Pau11a] and without a final explanation for this behavior. It might be due to the PSL, which becomes more ineffective at large displacements [Hen07] or due to measurement artifacts [Pau11a]. Also, the product of halo fraction and TPF reached the critical value of 0.75 [Pau11a]. The average halo fraction is, however, lower at around 27 % [Pau11a]. In other machines following values were found: $\approx$ 30 % is measured in Alcator [Gra96], less than 40 % in DIII-D [Str91] or 10 % in JET [Ric10]. An overview over several machines and scaling laws is given in [ITE99,

Hen07]. The observations vary largely around different devices and a unique dependence on machine and plasma parameters cannot be deduced, so far [Hen07]. For VDEs after a major disruption, the halo current fraction is smaller and displays a smaller toroidal asymmetry as the plasma current decays fast enough to keep the edge safety factor above the threshold value [Hen07].

The asymmetrical halo current can rotate with a frequency in the order of kHz as observed in Alcator [Gra96] or some hundred Hz in JET [Ric10], although this has not been observed in all experiments. This can help to distribute the vessel forces over the toroidal range [Boo12]. On the other hand, there is some concern that the rotation frequency coincides with the resonance frequency of the structure of 3-8 Hz in ITER [Ger14], which would further amplify the forces.

While the vertical instability is unavoidable for elongated plasmas, it can be handled with passive stabilization and an active vertical control system. In some scenarios, a vertical displacement event is unavoidable, when this system fails or after a disruption occurs. Simulations can be helpful to assess the effects on the device as well as to test control mechanisms. In the following section, the vertical control system employed in tokamaks is introduced to understand its mechanism and limits.

2.3 Control theory

One task of this thesis is to implement a controller for the vertical position control into the JOREK code in a way similar to the control system in the experiment. In order to gain a basic understanding of the vertical control system, the relevant elements of the theory are introduced in the next section, followed by a presentation of the PID controller. The section is then concluded with the outline of the main features of the magnetic control system in ASDEX Upgrade.

2.3.1 Basics of control theory

In the following, the basics of control theory are introduced with application to the magnetic control in tokamaks following the outline of [DT19].

The basic task of any controller is to obtain or maintain a specific state of a time dependent system by regulating certain input parameters. The time evolution of a system is described by:

$$\frac{\mathrm{d}\mathbf{x}}{\mathrm{d}t} = f(\mathbf{x}, \mathbf{u}, t), \text{ with } \quad \mathbf{x}_0 = \mathbf{x}(t = 0) \tag{2.33a}$$

$$\mathbf{y} = h(\mathbf{x}, \mathbf{u}, t), \tag{2.33b}$$

where $\mathbf{x} \in \mathbb{R}^n$ is the state vector of the system consisting of n variables, $\mathbf{u}$ is the input and $\mathbf{y}$ the output vector. The function f describes the time evolution of the state depending on the current state and the input, while h determines the output of the system.

In a tokamak, the state is given by the plasma variables, such as the plasma current or the density. The input vector would be the coil currents, while the output are shape and plasma parameters, for example. When the input as well as the output is scalar, the system is called **Single Input Single Output** (SISO) system, while in all other cases, it is named **Multiple Input Multiple Output** (MIMO). In general, a tokamak falls into the latter category, as the controller has multiple objectives, like controlling both the shape of the plasma cross section and the position of the magnetic axis. Alternatively, several SISO controllers are used if controlled quantities can be separated and regulated independently.

For a linear, time independent (LTI) system, the equations (2.33a) and (2.33b) can be written as a linear system of equations:

$$\frac{\mathrm{d}\mathbf{x}}{\mathrm{d}t} = \underline{\mathrm{A}}\mathbf{x} + \underline{\mathrm{B}}\mathbf{u} \tag{2.34a}$$

$$\mathbf{y} = \underline{\mathrm{C}}\mathbf{x} + \underline{\mathrm{D}}\mathbf{u}, \tag{2.34b}$$

where $\underline{\mathrm{A}}$,$\underline{\mathrm{B}}$,$\underline{\mathrm{C}}$ and $\underline{\mathrm{D}}$ are matrices and the other variables are as defined in equation (2.33). Nonlinear systems can be linearized around an equilibrium point to obtain the form of equation (2.34). Based on the eigenvalues of $\underline{\mathrm{A}}$, the stability properties are analyzed. As

long as all real parts are negative, the system is stable.

This analysis can also be performed by means of a Laplace transform, with which (2.34) can be written as

$$Y = \underline{\mathrm{G}}(s)U(s) \tag{2.35a}$$

$$\underline{\mathrm{G}} = \underline{\mathrm{C}}(s\underline{\mathrm{I}} - \underline{\mathrm{A}})^{-1}\underline{\mathrm{B}} + \underline{\mathrm{D}}, \tag{2.35b}$$

where s is a complex variable and Y is the Laplace transform of y. The **total transfer function** $\underline{\mathrm{G}}$ describes the output Y of the system depending on Laplace transform U of the input vector. For LTI systems, the transfer function $\underline{\mathrm{G}}$ is a rational function with a certain number of zeros and poles. The location of the latter in the complex plane determines the stability of the system by the so called **Nyquist stability criterion**.

The system can be modified by introducing other components like a controller. The Laplace transform then allows an easy mathematical description and stability analysis of the new system. When an open loop controller without feedback is placed in series to the system, the total transfer function is the product of the controller and system transfer function. However, the addition of this open loop controller does not change the location of the poles and roots of the total transfer function, which means that it has the same stability properties. Instead, a closed feedback loop is added, resulting in the total transfer function

$$\frac{\underline{\mathrm{G}}(\mathrm{s})}{1 \pm \underline{\mathrm{G}}(\mathrm{s})\underline{\mathrm{K}}(\mathrm{s})}, \tag{2.36}$$

which modifies the number of poles and zeros of the total transfer function as well as their location in the complex plane, and thus, allows to tune the stability of the system. The positive sign stands for a negative feedback loop and vice versa.

A schematic representation of the system and controller model is shown in figure 2.6. The combined system contains the controller and the plant model, which form the open loop model $\underline{\mathrm{K}}(\mathrm{s})\underline{\mathrm{G}}(\mathrm{s})$, underlaid in grey. The output y is the sum of the system output and the disturbances $\underline{\mathrm{G}}_d$ not included in the system transfer function. Finally, the feedback loop is closed by using the deviation e from the reference value r as an input for the controller. The system output is influenced by unavoidable measurement noise, which is added to the controller input. The output of the latter u, e.g. the coil currents, is then used as an input for the system.

In the vertical stability problem, the system consists of the plasma as well as the power supply and the diagnostics. The details of the problem and the application to ASDEX Upgrade are explained in section 2.3.3. One type of controller, the PID controller, is often used in applications because it is powerful and easy to adjust, even without deeper understanding of control theory. The working principle and characteristics are described in the following section.

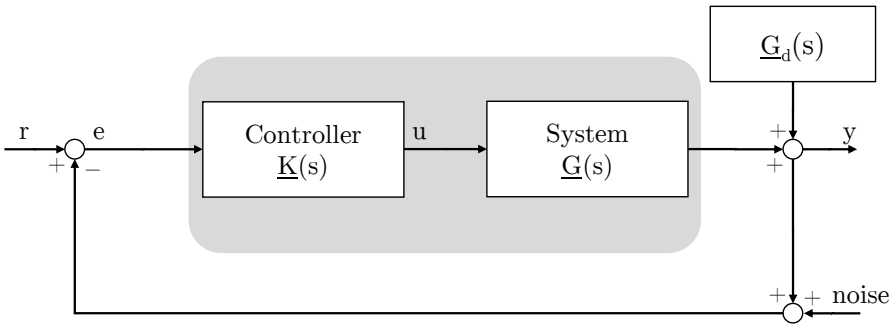

Figure 2.6: The schematic figure of the control problem contains the open loop system, shown in grey, which consists of the controller $\underline{\mathrm{K}}(\mathrm{s})$ as well as the system transfer function $\underline{\mathrm{G}}(\mathrm{s})$. The output of the system together with disturbances of the system G_d form the total output y. The loop is closed by using the error e between the reference value r and the system output together with measurement noise as an input of the controller. The output of the controller u, e.g. the coil currents, serves as an input for the system. (adapted from [DT19])

2.3.2 PID controller

The name of the **PID controller** has its origin in the way it calculates the output, consisting of a **p**roportional, **i**ntegral and **d**erivative component. The proportional gain K_P acts on the deviation from the reference value e, the derivative gain K_D on the time derivative of the error and the integral gain K_I on the time integrated error. The controller output u is calculated by the following equation:

$$u(t) = K_\mathrm{P}\, e(t) + K_\mathrm{D} \frac{\mathrm{d}e(t)}{\mathrm{d}t} + K_\mathrm{I} \int_{t_0}^{t} e(t')\mathrm{d}t'. \tag{2.37}$$

Different variants of this controller model are used, but most tokamaks employ the PD controller, which is a PID controller without integral gain.

The gains have different effects on the controlled signal. A controller with only proportional feedback would oscillate around the reference value and can destabilize the system if the gain is chosen too high. The derivative gain punishes changes in the controlled quantities and damps the oscillations of the output, while the integral gain reduces the steady state error from the reference signal and becomes more important the longer the error e persists.

The response of the system to a step excitation, a sudden change in the reference value, can be used to characterize the controller. Some important characteristics are shown in figure 2.7 and are explained in the following. The time it takes for the response to increase from 10 % to 90 % of the excitation value is referred to as the **rise time**. If the system is not overdamped, the response first exceeds the target value before it reverses and tends back to the reference. The difference between the maximum of the response to the excitation is defined as the **overshoot**. Usually, the response then oscillates around the reference value with a decreasing amplitude until it stays in a specified range (typically 2 % to 5 %) around

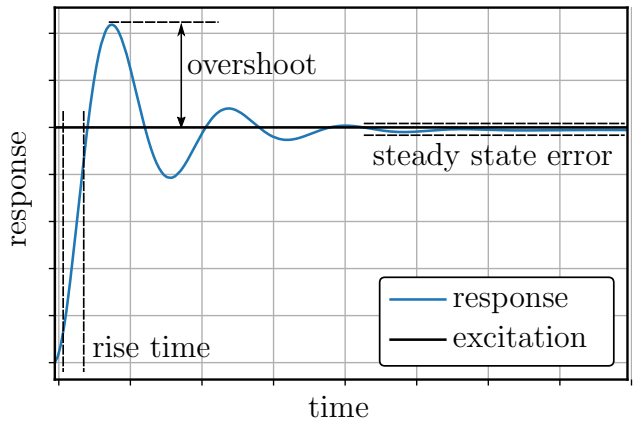

Figure 2.7: The step response of a closed loop system is shown. The rise time is largely influenced by the proportional gain and determines how fast it responds to a step excitation. This can however influence the overshoot, the maximum deviation from the reference value, negatively. The steady state error can be reduced by proportional gain and integral gain. (own representation)

it. The time it takes until it stays within these specified limits is called **settling time**. The response never fully reaches the reference value, but oscillates with a certain amplitude, the **steady state error**, around it. Finally, the **stability** defines, whether the system reaches a steady state at some point. Otherwise, it is called unstable.

The effects of the controller gains on these characteristics are analyzed by increasing the gains independently. The results are summarized in table 2.1 and the most important effects are described in the following. A larger proportional gain reduces the rise time, while the other gains do not have a strong effect. However, the proportional gain increases the overshoot and a too high setting can destabilize the controller. The overshoot and settling time can be reduced by increasing the derivative gain, which punishes fast changes of the response. Finally, the integral gain has the most important influence on the steady state error, as it becomes more important with time. However, a high value can create an **integral windup**, when the controller has reached its limits or when measurement errors occur, as the integral error then accumulates and eventually destabilizes the system. In practice, this is prevented by keeping the integrated error constant, when the limits of the output are

Table 2.1: The table shows the effect of an independent increase of the different gains on the closed loop step response. (adapted from [Kia05])

	Rise Time	**Overshoot**	**Settling Time**	**Steady State Error**	**Stability**
$K_\mathbf{P}$	Decrease	Increase	Small Increase	Decrease	Negative
K_I	Small Decrease	Increase	Increase	Large Decrease	Negative
K_D	Small Decrease	Decrease	Decrease	Minor Change	Improve

reached or by setting an upper threshold on the integral contribution.

A controller should reach a steady state, while observing a short rise time, a small overshoot and a small steady state error. The gains have to be tuned in a way to obtain a trade-off between these characteristics. Manual tuning is performed by first varying the proportional gain, while the others are zero until the system output oscillates around the steady state with a small error. Finally, the other gains are adjusted to optimize the response.

This type of controller is also employed in ASDEX Upgrade to control the plasma shape and position by the vertical field coils. The details of the system and the control strategy are explained in the following section.

2.3.3 Vertical stability control in ASDEX Upgrade

For stable plasma operation with optimal performance, control of certain plasma parameters such as the shape, the vertical position, the plasma current and auxiliary heating systems is indispensable. In this section, the vertical stability control of ASDEX Upgrade is described with brief mentioning of some of the other control systems of the machine and their dependencies.

In general, the feedback system has a MIMO (Multiple Input Multiple Output) structure, where multiple plasma parameters are used as an input to control several actuators. The control system reacts differently depending on the phase of the discharge – the current ramp up, the flat top phase, the ramp down – or when the onset of an instability is detected. The objectives of the control system is a stable plasma with optimal perfomance, while ensuring the safety of the machine as well as of the operators [Mer03]. In the following, only the magnetic control system for shape and position is described. Other control systems, e.g. for the heating, are not mentioned here.

As stated in the introduction section 1.3.2, the plasma shape is linked to its performance. Therefore, it is necessary to keep up optimal parameters by means of a control system. Apart from this, the plasma current as well as the vertical position have to be maintained because those quantities influence the vertical stability of the plasma as explained in detail in section 2.2. These three parameters are all controlled by PF coils presented in section 1.3.3, which are located far from the plasma outside the vacuum vessel, and thus, affect the whole plasma. This is a challenge for the control system, as it has to deal with multiple objectives that can, a priori, not be decoupled.

Each discharge phase has its own reprogrammed coil currents (FFC – Fast Forward Currents), which define the discharge scenario. The feedback system then acts on deviations from the target plasma and shape parameters. The input of the position and shape control is fed by several pairs of flux loops placed around the plasma to detect any deviation from the equilibrium state and the position is then deduced by a function paramterization (FP) algorithm. The position control is mainly done by the two fast position control coils (CoI) located inside the TF coils, while the V1–V3 coils are responsible for the shape control

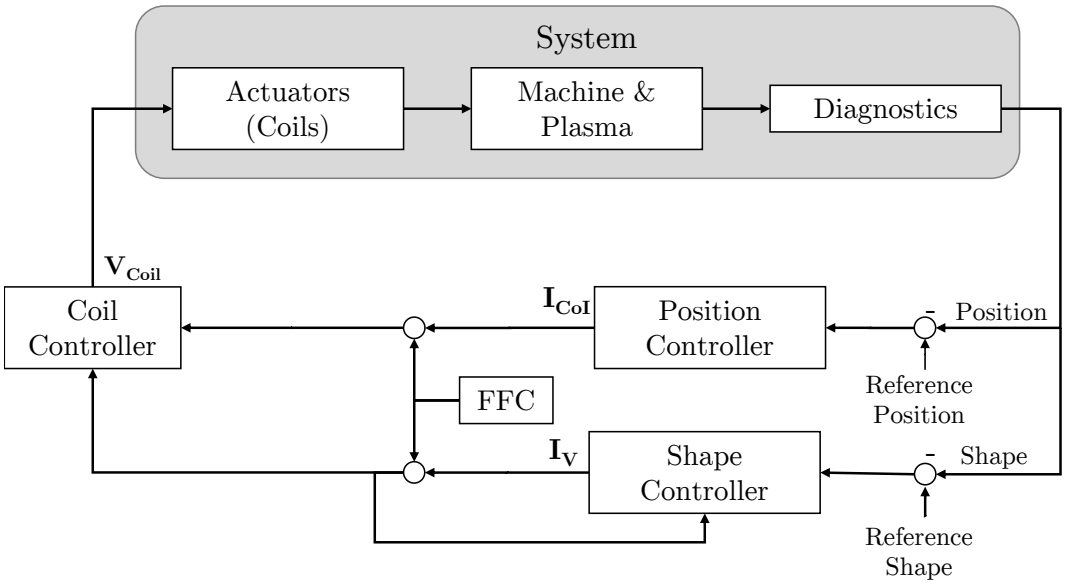

Figure 2.8: The control system of the plasma shape and position is shown here together with the system under control. The fast vertical feedback is done by the position controller acting on the CoI coils, while the shape control and load balance between the PF coils is performed by the shape controller, which acts on the V coils. The output of the controller is added to the predefined (FFC) currents. The system to be controlled consists of the coils, the plasma and the machine as well as the diagnostics. (adapted from was adapted from [Mer03])

acting on a longer time scale [Wie90]. In ASDEX Upgrade, the controller has a proportional-integral gain (PI) to control the coil current reference values, which are then in turn used as input of the power control system to calculate the required voltage [Gru93a]. The time constant of the vertical controller is about 40 ms [Mer03]. Only the presence of conductive structures, which slow down the motion from the inertial time scale to the resistive time of $\tau_{VDE} \approx 80$ ms, allow the control system to stabilize the vertical motion.

The output is **limited** by the voltage and current limits, as well as stresses on the mechanical structures and the power supply. Due to the coil current limits, it is necessary to take the load balancing between the PF coils into account for the controller design, as a failure of the control system could be fatal to the machine. The shape controller takes also care of distributing the loads between the V1–V3 coils as well as to reduce the current in the fast position control coils. In case no shape control is required, the vertical feedback is distributed between the CoI and V2 coils [Mer03]. Whereas in the other cases, the current distribution is more complex and goes beyond the scope of this thesis, where only the vertical control is implemented. The current limits of 21 kA [Dun] of the CoI coils are those relevant for the simulations of the vertical stability control in this thesis.

Figure 2.8 shows the principle design of the controllers for shape and vertical position together with the controlled system. The plasma current is also part of the magnetic control, as it is partly induced by the transformer coil, which is, however, not included here. The controller of the plasma shape and position provides target coil currents, which are added

to the prescribed currents of the discharge. Then, the target currents are translated into the voltage to be supplied by the power supply system. The whole system, which affects how the controller output is realized, consists of the actuators, the plasma and surrounding structures as well as the plasma diagnostics, which feed the input for the controllers. Each of these components has its own time delay properties as well as an error, which influence the control.

The implementation of the PID controller in the JOREK code is described in section 3.3. Before going into the details of the simulation setup and the controller implementation, the code framework used in this thesis is described in the following section.

2.4 Tokamak modelling

To better understand the physical processes observed in the experiments and to make extrapolation to future power plants, it is necessary to use large scale computer simulations, which produce reliable results. For disruptions and halo currents, for example, it has not been possible to deduce a scaling of the vessel forces and thermal loads based on only the machine parameters. Therefore, simulations provide a substantial contribution to the design and reliable operation of future devices. For the work performed in this thesis, the JOREK-STARWALL code framework is used, where JOREK solves the MHD equations in tokamak geometry and STARWALL incorporates the effects of conductive structures and coils.

2.4.1 The JOREK code

JOREK is a non-linear, fully implicit code that solves the extended MHD equations in realistic tokamak geometry using both MPI and OpenMP parallelization [Huy07, Hoe20]. It was originally developed for peeling–ballooning modes to simulate ELMs and now covers a broad range of applications, including large scale MHD instabilities, disruptions and their mitigation techniques, runaway electrons, fast particles and is currently being extended for stellarator geometries. In particular, simulations of VDEs have been carried out [Hoe14, AS18, Kre20, Art20c] to study the non-linear evolution and 3D effects of VDEs including benchmarks to other non-linear MHD codes.

JOREK solves the non-linear MHD equations for different model complexities, which incorporate different physical effects, depending on the use case of the application. Some models contain a reduced form of the MHD equations, described in [Fra15]. This allows to reduce the number of variables to be solved by making assumptions on the form of the magnetic field as well as on the form of the velocity. Also, this eliminates the fast magnetosonic waves in the plasma, allowing for larger time steps. A full MHD model is also available in JOREK [Pam20].

The magnetic field in reduced MHD is of the form:

$$\mathbf{B} = \frac{F_0}{R}\mathbf{e}_\phi + \frac{1}{R}\boldsymbol{\nabla}\psi \times \mathbf{e}_\phi, \tag{2.38}$$

with F_0 being a constant, R the major radius, ψ the poloidal flux and $\mathbf{e}_\phi$ the toroidal unit vector. Thus, only the poloidal field evolves in time, while the toroidal one is constant. Note that this also neglects the diamagnetic property of the plasma.

The so called **model 199** was used for this thesis, which is a comparatively simple **reduced MHD** model, containing non-ideal and resistive effects, particle and heat transport as well as source terms for density and temperature. The parallel velocity $v_\parallel$ along the magnetic field lines is not included in the model, which allows for large time steps. Instead, the parallel transport is replaced by the anisotropic particle diffusion coefficient $D_\parallel$. Thus, the ansatz

for the velocity reduces to

$$\mathbf{v} = -R\boldsymbol{\nabla} u \times \mathbf{e}_\phi, \tag{2.39}$$

where u is the electric potential. The equations of model 199 have the following form:

$$\frac{\partial \rho}{\partial t} = -\boldsymbol{\nabla}\cdot(\rho\mathbf{v}) + \boldsymbol{\nabla}\cdot\left(D_\perp \nabla_\perp \rho + D_\parallel \nabla_\parallel \rho\right) + S_\rho \tag{2.40a}$$

$$\rho\frac{\partial \mathbf{v}}{\partial t} = -\rho\,\mathbf{v}\cdot\boldsymbol{\nabla}\mathbf{v} - \boldsymbol{\nabla} p + \mathbf{J}\times\mathbf{B} + \mu\,\Delta\mathbf{v} - \mathbf{v}\,S_\rho \tag{2.40b}$$

$$\rho\frac{\partial T}{\partial t} = -\rho\,\mathbf{v}\cdot\boldsymbol{\nabla} T + (\gamma-1)\rho\,T\,\boldsymbol{\nabla}\cdot\mathbf{v} + \boldsymbol{\nabla}\cdot\left(\kappa_\perp \boldsymbol{\nabla}_\perp T + \kappa_\parallel \boldsymbol{\nabla}_\parallel T\right) + S_T \tag{2.40c}$$

$$\frac{\partial \psi}{\partial t} = \eta(j - j_0) - R^2\,\mathbf{B}\cdot\boldsymbol{\nabla} u \tag{2.40d}$$

$$j = R\partial_R\left(\frac{1}{R}\partial_R\psi\right) + \partial_{zz}\psi \equiv \Delta^*\psi \tag{2.40e}$$

$$\omega = \frac{1}{R}\partial_R(R\partial_R u) + \partial_{zz} u \equiv \Delta_{\mathrm{pol}} u \tag{2.40f}$$

with the density ρ, the velocity $\mathbf{v}$, the pressure p, the adiabatic coefficient γ and the temperature T. $S_{\rho,T}$ are source terms for the density and energy. $\mathbf{J}$ is the current density and $\mathbf{B}$ the magnetic field. The evolution of the poloidal flux ψ is defined by the electric potential u, and the toroidal current $j = -R\,\mathbf{J}\cdot\mathbf{e}_\phi$. In applications, where the current profile should be kept approximately constant, an artificial current source j_0 is applied. The current j is determined by the magnetic flux, and the vorticity ω by the electric potential u. The particle and heat transport coefficients D and κ appear in the equation either along $\parallel$ or perpendicular $\perp$ to the field lines. These transport coefficients and the viscosity μ are determined by transport models and not by JOREK, so that they enter into the model as inputs. The equations are solved for the unknowns ψ, u, j, ω, ρ and T.

The equations are solved in the weak form using the **finite element** approach by multiplying them with suitable test functions and integrating them over space.

In order to solve the set of equations (2.40) numerically, they have to be discretized in time and space. JOREK uses a discretization in 2D, bicubic **Bézier elements** [Cza08] in the poloidal plane, while the toroidal direction is taken into account by **Fourier decomposition** into n_{har} harmonics. A variable X can then be expressed by:

$$X(s,t,\phi) = \sum_{n=0}^{n_{har}-1}\sum_{i=0}^{3}\sum_{j=0}^{3}\left(X_{i,j,c}B_i^3(s)B_j^3(t)\cos(n\phi) + X_{i,j,s}B_i^3(s)B_j^3(t)\sin(n\phi)\right), \tag{2.41}$$

where s and t are the coordinates on the element in the range $0 \le s,t \le 1$, $B_{i,j}^3$ are Bernstein polynomials of degree 3 and $X_{i,j}$ is the cosine or sine component of the quantity at the control point i,j. When running JOREK, first, the axisymmetric equilibrium is solved and the simulation runs linearly for some time steps to obtain steady state flows. Afterwards,

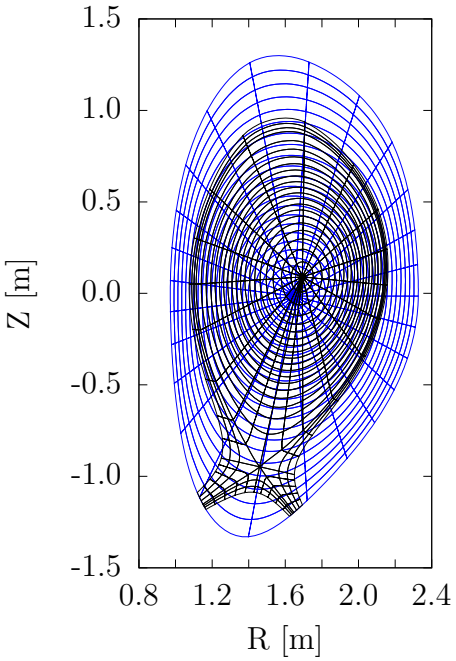

Figure 2.9: The equilibrium is first established on the poloidal grid shown in blue to find the flux surfaces which then are used to define the second grid shown in black. Here, the number of grid points was reduced significantly for better visibility. (own representation)

higher modes are are launched and can evolve non-linearly.

It is possible to use either a poloidal or a flux surface aligned grid, both shown in figure 2.9, for easier numerical treatment. A poloidal grid was sufficient for this thesis, as the advantages of a flux aligned grid vanish, when the plasma is displaced substantially from its initial position during a VDE.

The **time discretization** is fully implicit, allowing the usage of large time steps using the following scheme [Fra15]:

$$\begin{aligned} \frac{\partial \mathbf{A}(u)}{\partial t} &= \mathbf{B}(\mathbf{u}, t) \\ \left[(1+\xi)\left(\frac{\partial \mathbf{A}}{\partial \mathbf{u}}\right)^n - \Delta t\theta\left(\frac{\partial \mathbf{B}}{\partial \mathbf{u}}\right)^n\right]\delta\mathbf{u}^n &= \Delta t\mathbf{B}^n + \xi\left(\frac{\partial \mathbf{A}}{\partial \mathbf{u}}\right)^n \delta\mathbf{u}^{n-1}, \end{aligned} \tag{2.42}$$

where $\delta\mathbf{u}^n = u^{n+1} - u^n$. The time dependent equations of (2.40) can be written in the form of the first line with the RHS and LHS depending on the vector of variables $\mathbf{u}$, with the superscript indicating the evaluation at the time step n. The numerical parameters ξ and θ determine the scheme that is used. A value of $\theta = 1/2$ and $\xi = 0$ correspond to the Crank–Nicholson scheme for example. In the end, we obtain a matrix equation, which is solved with an iterative solver, like *GMRES*, after applying a preconditioner.

In **fixed boundary** simulations, the boundary conditions are given by Dirichlet conditions, fixing the variable values on the boundary, except for field lines intersecting the bound-

ary like in the divertor region. There, Bohm's boundary conditions are used to include the outflow of the particles along the field lines. In fixed boundary simulations, the value of the magnetic flux ψ on the boundary also remains fixed, which means that the boundary acts as an ideally conducting wall. When including resistive wall effects and external fields, free boundary simulations are required.

For **free boundary** simulations, the fixed boundary condition for the magnetic field is replaced by a Neumann boundary condition, which connects the normal magnetic field to the tangential magnetic field on the boundary. It is possible to apply the free boundary condition on only specified harmonics, when considering only magnetic perturbations for example. In particular, for free boundary simulations including the axisymmetric $n = 0$ mode, it is necessary to obtain a free boundary equilibrium. For this, the equilibrium magnetic field of the PF coils has to be provided either by experimental data of the coil currents or by using a functionality of JOREK, that calculates the coil currents for a given fixed boundary equilibrium. Both, the free boundary equilibrium solver and the equilibrium coil current calculation were developed in [AS18]. The tangential magnetic field is expressed by the STARWALL code in terms of matrix expressions, which will be described in the following section.

2.4.2 The STARWALL code

Instabilities that change the magnetic field signature outside the plasma induce mirror currents in the surrounding conductive structures, which in turn act back on the plasma and thus, can have a stabilizing effect in certain cases. Especially for VDE simulations, the response of the conductive structures is essential to capture the full dynamics as described in section 2.2. Also, the variation of the coil currents allows to control the plasma during the simulation run, while passive coils are used for diagnostic purposes. Therefore, modeling the passive conductive structures and active coils is necessary to study large scale instabilities and their mitigation techniques.

JOREK has the capability of incorporating the effects of a resistive or ideal wall as well as a set of coils by coupling [Hö12] it to the STARWALL code [Mer15]. A detailed derivation of the STARWALL equations can be found in [AS18]. Initially, the derivation was done using the energy variation principle, however not accounting for halo currents [Mer15].

The wall and conductive structures are discretized by triangles using the thin wall approximation. By applying a Green's function approach and the finite element method, STARWALL calculates the response of the vacuum and the wall to the magnetic field on the JOREK computational domain as well as the magnetic field by the active coils. This response can be expressed by a set of matrices, called the STARWALL "response matrices" that provide the tangential magnetic field on the JOREK boundary, when given the normal

magnetic field on the JOREK boundary and the currents in the conductive structures:

$$\mathbf{B} \times \mathbf{n} = \underline{\mathrm{M}}_{\mathrm{vac}} \mathbf{B} \cdot \mathbf{n} + \underline{\mathrm{M}}_{\mathrm{cp}} \mathbf{I}_c, \tag{2.43}$$

where the matrix $\underline{\mathrm{M}}_{\mathrm{vac}}$ describes the relation between the normal magnetic field and the tangential magnetic field of the plasma on the boundary, and the matrix $\underline{\mathrm{M}}_{\mathrm{cp}}$ provides the tangential magnetic field due to the current $\mathbf{I}_c$ in the conductive structures and $\mathbf{n}$ is the normal vector to the JOREK boundary.

Furthermore, STARWALL provides the evolution equation for the currents in the conductive structures and coil $\mathbf{I}_c$ derived by a resistive-inductive circuit equation of the form:

$$-\underline{\mathrm{L}} \dot{\mathbf{I}}_c = \underline{\mathrm{M}}_{\mathrm{pc}} \dot{\mathbf{B}} + \underline{\mathrm{R}} \mathbf{I}_c, \tag{2.44}$$

where $\underline{\mathrm{M}}_{\mathrm{pc}} \dot{\mathbf{B}}$ describes voltage in the conductors due to the flux change of the plasma, while $\underline{\mathrm{R}}$ and $\underline{\mathrm{L}}$ are the resistance and inductance of the conductive structures, respectively, also taking into account the mutual inductance between the conductive structures. This equation allows to evolve the currents in JOREK with the same implicit time stepping scheme (2.42) as used for solving the MHD equations.

This concludes the background required for the investigations of this thesis. In the following chapter, the setup of the simulation and the modelling of the PSL is described as well as the implementation of a control system in JOREK.

3 Setup and modelling

This chapter contains the description of the setup for an ASDEX Upgrade case as well as the modelling of the PSL in STARWALL. In the last section, the implementation of the controller in JOREK is explained.

3.1 Initial setup

The simulations carried out in this thesis are all based on the AUG discharge # 28848. The equilibrium reconstruction code *Cliste* [McC99] allows to extract the necessary equilibrium parameters from the shot files to create inputs for JOREK. These include the values of ψ on the boundary, necessary for the fixed boundary equilibrium, as well as the initial profiles of the density, the temperature and FF' ($= F\frac{\partial F}{\partial \psi}$). Also, the value of F_0 (see equation (2.38)), the density in the center and the geometric center used for the initial grid are provided. Furthermore, it is possible to obtain the PF coil currents of the experiment, which are needed for the free boundary simulation including the $n = 0$ mode. The plasma parameters extracted from the equilibrium code for this shot as well as the values obtained by the JOREK free boundary equilibrium solver are shown in table 3.1. The values show only a minor difference compared to those from the experiment, thus, the equilibrium reconstruction was successful.

Table 3.1: Comparison of JOREK equilibrium to the one reconstructed by *Cliste* equilibrium 28848, edition 2, t=7 s

parameter	unit	JOREK	*Cliste*
axis R	[m]	1.696	1.699
axis Z	[cm]	3.818	3.800
X–point R	[m]	1.429	1.441
X–point Z	[m]	-0.962	-0.955
$2\pi\Delta\psi$	[T m^2]	0.193	0.196
q_{95}	[−]	5.350	5.389
q_0	[−]	1.489	1.325
I_p	[MA]	7.870	8.000

For the STARWALL modelling, the coil positions, the number of turns and their geometry were provided by [Dun], which allows us to create the input files for STARWALL. The coils modelled include the PF coils V1–V3, the fast position control coils CoI, the transformer coil (OH) as well as the PSL as shown in figure 3.1. All these coil types and their function were introduced in section 1.3.3. The resistance of the active PF coils was set to a large value, since their currents are imposed by an external current source. Special care was given to obtain a realistic PSL geometry and the correct resistive decay time of the current. As the PSL plays an important role, the modelling will be explained in detail in section 3.2. The geometry of the structures as well as the plasma are presented in 3D in figure 3.2.

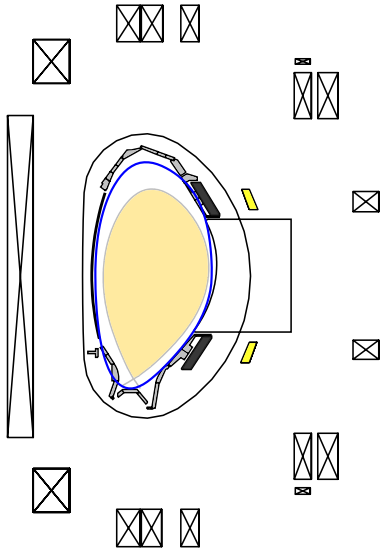

Figure 3.1: The JOREK computational domain boundary (in blue) was chosen to be as close as possible to fill the space inside the PFCs (in light grey, not modelled in STARWALL) and the PSL (dark grey). The plasma and internal structures are surrounded by the vacuum vessel. On its outside, the PF coils are located with the CoI coils used for the vertical feedback highlighted in yellow.

The vacuum vessel in STARWALL is represented as a toroidally symmetric structure, without holes and is modelled with triangles using the thin wall approximation. STARWALL requires the thin wall resistivity given by $\eta_{thin,w} = \frac{\eta}{d_w}$, where d_w is the wall thickness and η_w its resistivity. The AUG vacuum vessel has a value of $\eta_{w,thin} = 3 \times 10^{-5}\,\Omega$, when using the

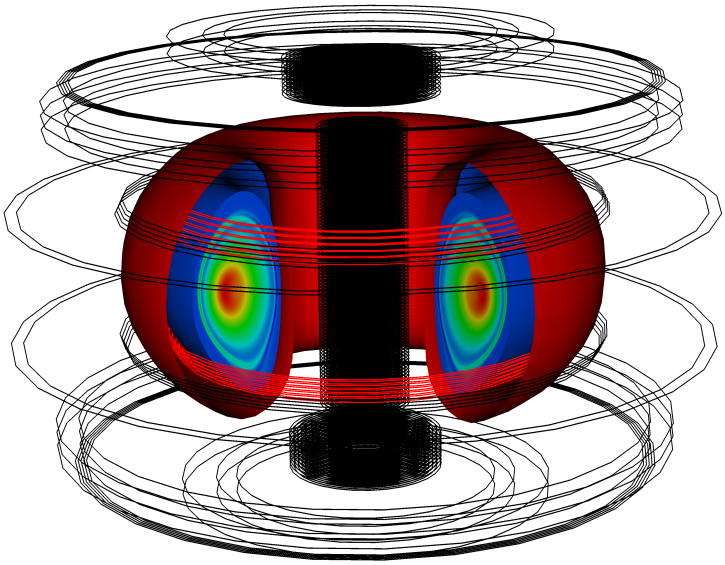

Figure 3.2: The poloidal field coils in black are located outside the wall, while the PSL in red is placed close to the plasma. The coils are modelled as thin axisymmetric filaments in this case.

material specification of steel, while the measured resistivity [Gia15], results in an $\eta_{w,thin}$ of $2 \times 10^{-4}\,\Omega$. The center of figure 3.1 shows the location of the JOREK boundary and the separatrix with respect to the PFC structures, which were not included in the modelling, as well as the the vacuum vessel. The boundary was chosen large enough to reach the height of the divertor, allowing the plasma to move in the same range as in the experiment. In the following section, the different options for modelling the PSL are presented and compared.

3.2 Coil modelling

The PSL geometry and location play an important role for passively stabilizing the vertical position of the plasma. Therefore, the modelling of the coil is presented in this section. There are three major influences of the geometry on the stabilization properties of the PSL. First, the location is important, as the distance from the plasma influences the coupling between the structures. Second, the shape of the coil determines the relation between its resistivity and the total resistance as well as the self-inductance. Third, the current in the loops have to be anti-parallel, in order to effectively produce a net vertical force on the plasma column. These factors have been taken care of during the modeling. The 3D geometry of the PSL in AUG is shown in figure 1.11.

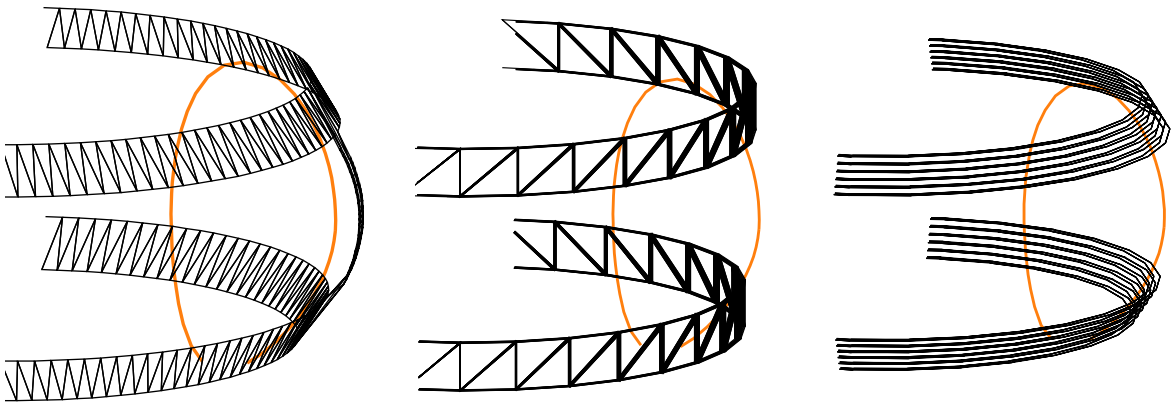

Figure 3.3: The PSL can be represented as a 3D structure including the vertical bridge as shown on the left, or as axisymmetric loops as in the middle and on the right. The JOREK computational boundary in orange was chosen as large as possible without intersecting with the coil structure.

There are three different approaches for modelling coils in STARWALL. The first is breaking down the coil structure into a number of thin, small filaments (named *axisym_fila* in STARWALL) as shown on the right of figure 3.3. This is used for axisymmetric coils and provides freedom for the form of the cross section. Second, the coil can be represented by axisymmetric, broad bands (*axisym_thick*). In order to model the thickness of the structure, the bands can be distributed in R and Z direction. Third, it is possible to generate a coil by

Table 3.2: Self inductance values for the geometries

3D PSL	broad band PSL	filamentary PSL	documentation value
15.1 µH	13.5 µH	3.52 µH	13.2 µH

providing points along the coil outline in STARWALL (*general_thin*). While it is possible to include the vertical bridge in this model, it neglects the thickness of the coil, while this can be accounted for by using several distributed bands or filaments for the other coil types. Details on this coil type in particular and coil properties in general can be found in [Sch17]. The total resistance and number of coils have to be specified for all the coil types. As the gap in the PSL rings is small, it can be represented as two loops of quadrangular cross section, while enforcing the coil currents to be of equal magnitude and opposite direction.

Different PSL models, based on the coil types described above, are created. In the 3D discretization, the bridge connecting the upper and lower ring is included as shown in figure 3.3, so that the coil current in the upper and lower part is automatically antiparallel. For the axisymmetric models, this was enforced by setting a negative value for the turns in the lower PSL ring. The validity of all these geometries for the PSL is shown in section 4.3.1.

Apart from the correct placement of the coil, the resistive decay time, defined by the ratio of self-inductance over resistance L/R, has to be correct as this determines the growth rate of the vertical instability. STARWALL calculates the resistivity in the thin wall approximation as well as the self-inductance and mutual inductance between each of the coils. Due to the differences in geometry, it can happen that the resistive decay time deviates from the real one. Therefore, the PSL resistance was scaled slightly to obtain the correct value of $\tau_{PSL} \approx 0.6s$

The self-inductance for the three geometries are listed in table 3.2, where it can be seen that the self-inductance value of the broad band model is closest to the documentation value, while the filamentary model has a large error. This is due to the difference in representation, as the filaments height is chosen too low to cover the full cross section height.

3.3 Vertical stability control in JOREK

For the work of this thesis, a PID controller (see section 2.3) has been implemented in JOREK. In ASDEX Upgrade, the CoI coils (see section 1.3.3 for the coils and section 2.3.3 for the control system in AUG) are used for the fast vertical stability control. The same coils are used for the AUG cases in JOREK, which only includes the fast vertical position control and not the shape control and load balancing performed by the V1–V3 coils.

The feedback control acts on the position and displacement velocity of the magnetic axis, which is determined by a search algorithm described in D. The difference in the coil current is calculated according to the feedback equation of a PID controller (2.37):

$$\Delta I = \frac{a}{\mathrm{d}t}\left(K_P(Z_n - Z_{\mathrm{ref}}) + K_D \frac{Z_n - Z_{n-1}}{\mathrm{d}t} + K_I Z_{\mathrm{int}} \right), \tag{3.1}$$

where Z_n is the vertical position of the magnetic axis at the time step t_n, Z_{ref} the target value and Z_{int} is the time integrated deviation from the reference. The controller output is normalized by the time step and a parameter a, to make the feedback independent from the time stepping. This is not necessary if a tact time is specified. In the following, the vertical position of the magnetic axis is referred to as axis position.

Table 3.3: Parameters for vertical stability control and their typical values

Parameter	Comment	Typical values
a_VFB(1)	proportional gain K_P	1.0×10^3
a_VFB(2)	derivative gain K_D	1.0
a_VFB(3)	integral gain K_I	1.0
VFB_start	start time of vertical feedback	-
vert_FB_amp_ts	gain amplification factor for individual coils	> 0 for upper < 0 for lower coils
I_coils_max	maximum allowed current in the PF coil	≈1 to 100 kA
VFB_tact [ms]	Apply VFB only every x ms	3 ms (not used)
Z_ref_ts(t)	time trace of reference axis position	case specific

The diagram in figure 3.4 shows how the PID controller is built into the time evolution in JOREK. The subscript n indicates the current time step and Z_{ref} is the target position of the axis. The controller response is calculated during the construction of the matrices, that arise from the MHD equations and are solved at every time step. Before the matrix construction, the current in the active coils, e.g., the PF coils, is determined for the current time step. The feedback of the controller is added to the prescribed value of the PF coil currents.

When the vertical feedback system is active, meaning the simulation time is larger than the start time and the feedback was activated by the coil amplification factor, the coil currents are calculated by the following procedure. First, the target axis position is determined for the current time step. Second, the integrated error Z_{int} is increased by $(Z_n - Z_{\mathrm{ref}})\Delta t$ and

the displacement velocity $\frac{\mathrm{d}Z}{\mathrm{d}t} = \frac{Z_n - Z_{n-1}}{\Delta t}$ is calculated. If the time since the last controller cycle is above the specified controller tact VFB_tact, equation (3.1) is applied to obtain the difference in coil currents. If the current limits of the coils I_coils_max are reached, the current is limited to the maximum coil current.

In the next step, the wall and coil currents are evolved. The PF coil currents are imposed via a source term in the evolution equation, which looks like

$$\underline{L}\frac{\mathrm{d}I}{\mathrm{d}t} = -\underline{R}(I - I_{PF}), \tag{3.2}$$

neglecting the induction by the plasma, where $\underline{L}$ is the inductance matrix and $\underline{R}$ is the resistance matrix of the coils. Due to the high resistance of the PF coils, the currents follow the imposed value very closely.

Finally, the matrix is constructed and solved, before going to the next time step.

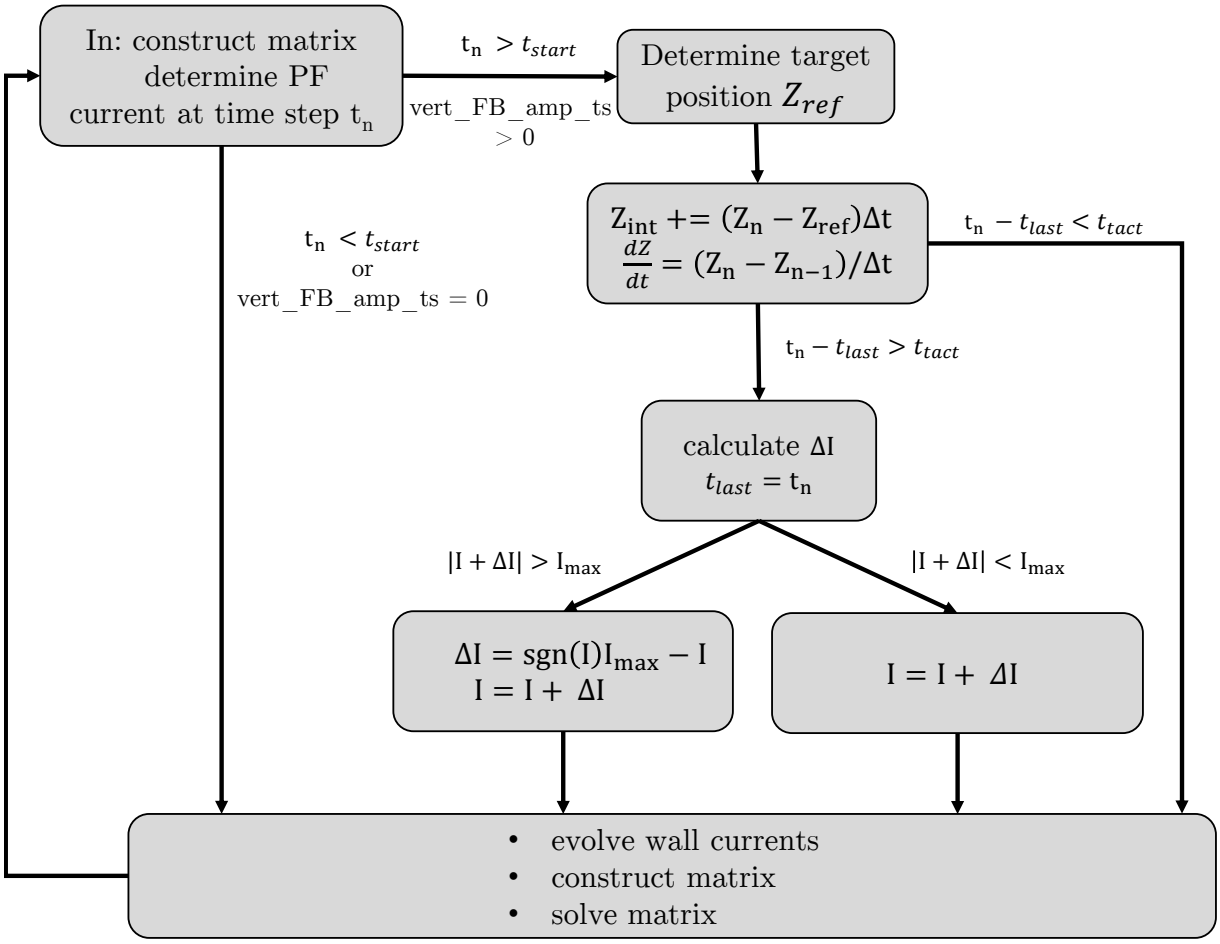

Figure 3.4: The structure of the PID controller in the JOREK time stepping is shown. Additional steps, like preconditioning and diagnostics are not shown here.

While the controller type modelled here is the same as in the ASDEX Upgrade experiment, there are some substantial differences to the real control system. First, the controller acts

directly on the magnetic axis position, while the experimental one relies on measurements of magnetic flux loops. Second, the power supply system and its limits are not included in the model of JOREK. Instead, only a limit on the maximum current is given, without taking into account the delays and limits on the gradient of the currents. Furthermore, the controller acts continuously in the simulations performed here and not tacted as in ASDEX Upgrade, as we are not limited by the measurement rates in the diagnostics, the controller system itself or the time delays of the power supply system. Thus, the implemented controller represents an idealized model excluding the time delays of the system components and the measurement noise of the experiment.

This chapter explained the setup used for the simulations, that were carried out in this thesis. The following chapter presents the results of the simulations.

4 Results

In this chapter, the work of this thesis and its results are presented. First, the results of an extensive validation of axisymmetric, passive coils in JOREK-STARWALL are shown in section 4.1, as they are essential for modelling the PSL in ASDEX Upgrade as well as passive stabilizing structures in general. Second, the interaction of the vertical plasma motion with the PSL is validated in a benchmark with the linear MHD code CASTOR3D in section 4.2 to show the correct scaling of the VDE growth rate with the PSL conductivity. Afterwards, the influence of the wall and coil resistivity as well as different PSL representations in the code is investigated in section 4.3. An active controller for the vertical stabilization was implemented in JOREK as part of the work of this thesis, which will be studied in section 4.4.

This validation and code development form the basis for more advanced simulations. First the dependence on the VDE growth rate and the effects of the controller is tested for different plasma elongations in section 4.4.2. Further on in section 4.5, the evolution of an axisymmetric VDE following an artificial thermal quench for different current quench rates is measured including an investigation of the controller limits. Finally, first simulations of the vertical plasma motion resulting from a thermal quench triggered by massive material injection are carried out in section 4.6.

4.1 Validation of axissymetric coils

Free boundary simulations of VDEs with JOREK have already been carried out before (e.g. [Kre20]). Different to these cases, ASDEX Upgrade contains a passive stabilising loop, which compensates for the insufficient stabilization of the $n = 0$ mode by the distant conducting vacuum vessel. Therefore, the passive coils in JOREK-STARWALL have to be validated before realistic VDE simulations with the structures of ASDEX Upgrade can be performed. The first part of this section consists of the validation of the coils and their mutual interaction, before including the effects of the plasma in the second part.

4.1.1 Coil validation

Self-inductance: An important characteristic of conductive structures is the self-inductance $\mathcal{L}$, which together with the resistance $\mathcal{R}$ determines the resistive decay time $\tau_{PSL} = \mathcal{L}/\mathcal{R}$ that limits the growth rate of the VDE as shown in section 2.2. To measure the current decay time of the PSL models in JOREK, the plasma current was quenched to zero, which induces a current in the passive coil due to flux conservation. The induced current then decays exponentially in absence of the plasma like:

$$I = I_0 e^{-\gamma(t-t_0)}, \tag{4.1}$$

where I_0 is the PSL current at the time t_0, when the plasma current reaches zero. The decay constant $\gamma = (\mathcal{L}/\mathcal{R})^{-1}$ is the inverse of the resistive decay time.

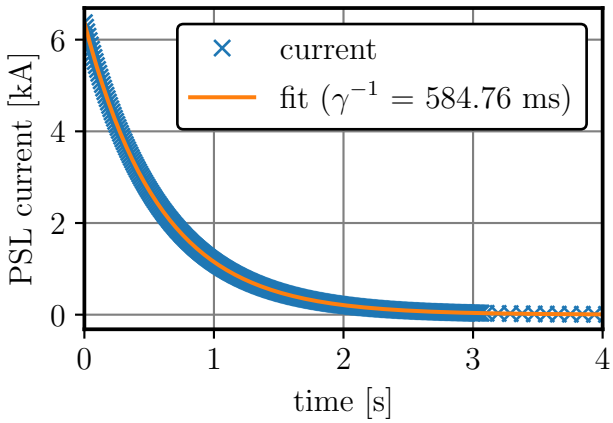

Figure 4.1: The current decays exponentially in the time scale of the resistive $\mathcal{L}/\mathcal{R}$ time of the coil. The measured value for the broad band model is close to the experimental value of 600 ms.

The fit to the current decay curve of the broad band PSL model shown in figure 4.1 resulted in a value of $\gamma^{-1} = 585$ ms, which is close to the value of ≈ 600 ms given in the documentation [Upg]. The self-inductance calculated by STARWALL is 13.5 µH, which results in an $\mathcal{L}/\mathcal{R}$ time of 586 ms given the resistance of 23 µΩ. This shows that, first, the modelled coil has the same specifications as the real one and second, that the self-inductance calculated by STARWALL is consistent with the current decay in JOREK.

For the filamentary model and the 3D PSL, two alternative models to describe the PSL in STARWALL introduced in section 3.2, an $\mathcal{L}/\mathcal{R}$ time of 608 ms and of 654 ms were obtained, respectively, in the same manner after scaling the resistances to compensate for the deviation in the self-inductance as explained in the same section.

Coil-coil interaction: The interaction between coils was validated by placing two coaxial loops with a diameter of 50 m close to each other at a distance of 2 cm in a setup without plasma. The current of one was prescribed, while the other one acted as a passive coil. When the current of the active loop is ramped up from zero, the current of the passive loop is given by:

$$I_p = -\frac{M_{ap}}{L_p} I_a, \tag{4.2}$$

where $I_{p,a}$ is the current of the passive, active coil respectively, L_p is the self-inductance of the passive loop and M_{ap} is the mutual inductance of the coil pair.

The current of the active coil was ramped up to 3 kA, following the shape shown in figure 4.2. Using the inductance values calculated by STARWALL as $L_p = 23.1$ µH and $M_{ap} = 11.7$ µH, we obtain the ratio of $M_{ap}/L_p \approx 0.51$ between the mutual and self-inductance. The current in the passive coil follows the active coil multiplied by the ratio M_{ap}/L_p with a small delay as shown in figure 4.2 and then saturates with a small deviation from the expected current.

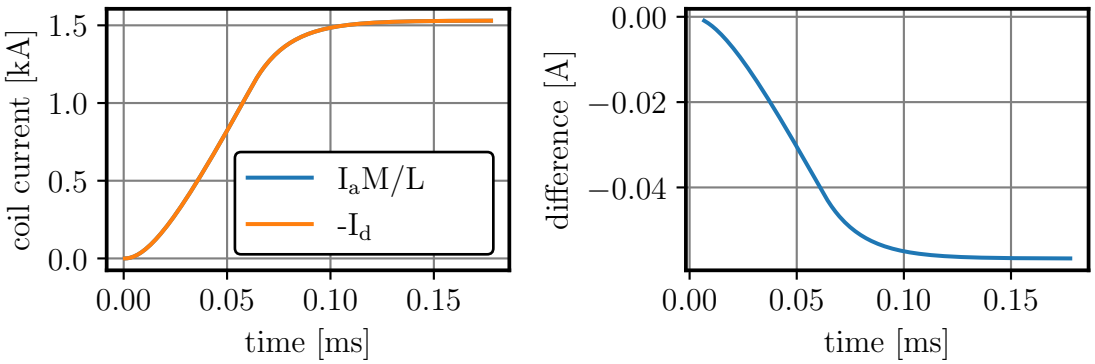

Figure 4.2: An active coil a induces a current in the passive coil p determined by the ratio of their mutual inductance M_{ap} and the self-inductance L_p of the passive coil. On the right the deviation from the expected current is shown.

Coil-wall interaction: In most experiments, the PF coils for the feedback controller are located outside the vacuum vessel, which reacts to current changes in the coils. In order to validate the interaction between a coil and the conducting wall structure in STARWALL, the following test was set up. A wall and a coil of similar geometry and equal resistivity are

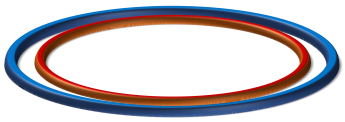

Figure 4.3: Location of the active coil in blue and the passive wall or coil in red.

placed in the plane of an active current loop as shown schematically in figure 4.3. Like in the case before, the plasma has been removed to suppress external influences. The current of the active coil was ramped up to 30 kA, inducing a current in the passive structures according to equation (4.2). Figure 4.4 shows how the induced currents in the wall and coil become very similar, when increasing the distance to the active coil because the difference in geometry is

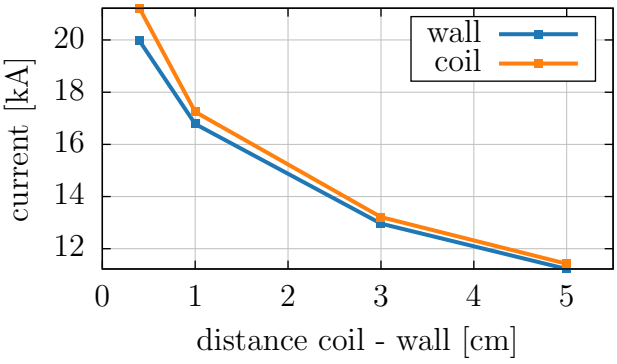

Figure 4.4: The current induced in a coil and wall of similar shape by an active coil is compared. At a larger distance from the active coil, the geometry of the structure is less important and the induced currents are similar.

less important at a larger distance to the active coil. As the coil-coil interaction has been validated above, this shows that the interaction between the wall and a coil behaves in the same way.

Analytic field calculation: The last part of the coil validation without plasma effects consists of numerically calculating the magnetic field of the coils with the Biot–Savart law (4.3) and comparing it to the field on the JOREK boundary in absence of a plasma. The Biot–Savart law allows to calculate the magnetic field of a coil filament with arbitrary geometry by:

$$\mathrm{d}\mathbf{B}(\mathbf{r}) = \frac{\mu_0}{4\pi} I \, \mathrm{d}\mathbf{l} \times \frac{\mathbf{r} - \mathbf{r}'}{|\mathbf{r} - \mathbf{r}'|}, \tag{4.3}$$

where $\mathrm{d}\mathbf{B}$ is the magnetic field at the location $\mathbf{r}$ due to the current I in the coil segment $\mathrm{d}\mathbf{l}$ located at $\mathbf{r}'$. This expression was integrated numerically for the PF coils of AUG to obtain the full magnetic field. The tangential projection on the JOREK boundary in the poloidal plane was then compared to the JOREK result.

In order to remove the magnetic field of the plasma, it was quenched by setting a large resistivity and increasing the perpendicular heat and particle transport. The magnetic field on the boundary is then only due to the coil currents, which were chosen as in the experiment, while only the PSL current can evolve freely. After letting the PSL and wall currents decay to zero, only the field of the PF coils remained. In figure 4.5, the results are shown along the JOERK boundary points. The value of the tangential field obtained by the Biot-Savart law is very close to the one calculated by JOREK. The small difference can be partly explained by the slightly simplified geometry of the PF coils used for the Biot-Savart law, where the coil is represented by an infinitely thin band as well as errors arising from the numerical integration and the tangential projection.

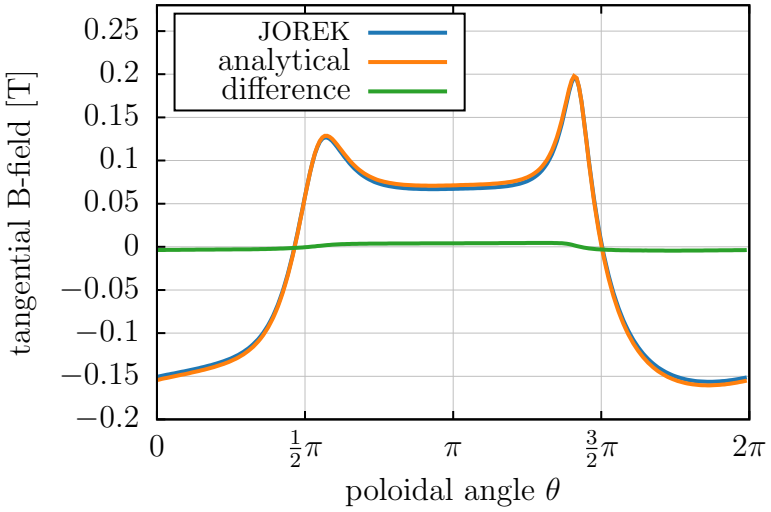

Figure 4.5: The tangential magnetic field along the JOREK boundary points produced by the AUG coils compared to the field calculated with the Biots-Savart law.

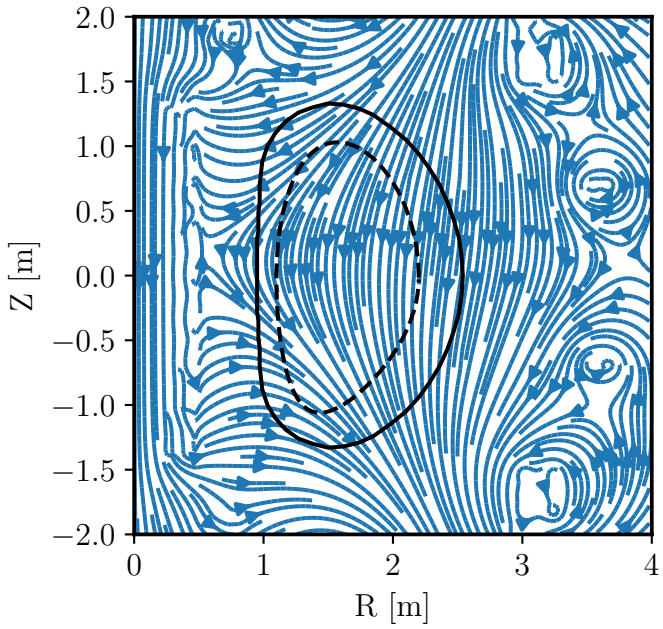

Figure 4.6: Magnetic field of the PF coils in the poloidal plane with the outline of the vacuum vessel and the JOREK boundary (dashed).

The field lines in the poloidal plane are shown in figure 4.6 together with the JOREK boundary and the wall. The eddies indicate the position of the V coils and small OH coils, while the transformer coil shows the typical field structure of a solenoid with straight lines in the center. The form of the quadrupole field produced by the V1–V3 coils, which is responsible for the plasma shape, can be nicely seen here. Also, it can be deduced from the curvature of the field lines that the field index deteriorates, when the plasma moves inwards.

This completes the series of the coil validation, which do not yet include the interaction with the plasma. In the following section, the validation will be extended to cover the current induction by plasma flux changes.

4.1.2 Coil plasma interaction

In the following section, the interaction between coils and plasma is investigated in two different ways. The goal is to validate the current induction in a passive coil by a change in the plasma and second, to verify that the coil currents have the correct effect on the plasma.

Current induction in wall and coil: First, it is shown that a moving plasma induces the same current in a passive coil as in a wall of comparable shape and position. The current induction in the wall by a flux change of the plasma has already been validated before in [AS18], so that it is sufficient to show the wall and a passive coil behave in the same way.

The coil consists of two toroidal bands of the height $2b$ at a distance $2a$ placed at the major radius R_w as shown in figure 4.7, while the cross section of the wall is an ellipse with

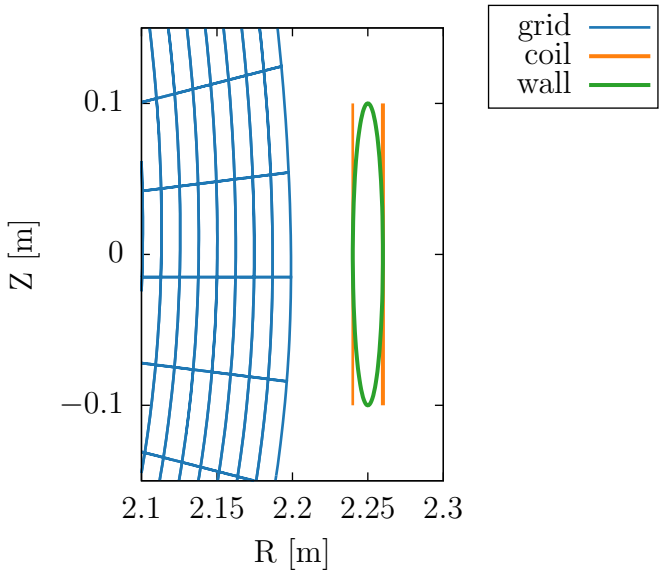

Figure 4.7: Placement of the wall and the two bands of the coil next to the plasma.

the same height and roughly the same cross section as the two coil bands described by:

$$\mathbf{R} = \begin{pmatrix} a\cos(\theta) + R_w \\ b\sin(\theta) \end{pmatrix} \tag{4.4}$$

with the semi-major axis a, the semi-minor axis b and the poloidal angle θ.

In order to compare the current induction, the wall and coil resistivity must be set to the same value. As STARWALL requires the thin wall resistivity $\eta_{w,thin}$ for the wall and the total resistance for the coil input, those quantities were calculated consistently by the definition of the resistivity η:

$$\eta_w = \mathcal{R}\frac{A}{l} \approx \mathcal{R}\frac{2d_w 2a}{2\pi R_w} \tag{4.5}$$

$$\eta_{thin,w} = \frac{\eta_w}{d_w} = \mathcal{R}\frac{2a}{\pi R_w}, \tag{4.6}$$

where the wall resistivity η_w is defined as the product of the resistance $\mathcal{R}$ of the conductor with a cross section A and a length l. The cross section of the wall is the height $2a$ multiplied by twice the wall thickness d_w, as both wall sides are penetrated by the field. The length of the axisymmetric wall is $2\pi R_w$, where R_w is the major radius of the wall. The coil resistance $\mathcal{R}$ was chosen to match the given resistivity of the wall $\eta_{\mathrm{w,thin}}$ by inverting equation (4.6).

First, the coil and the wall were both placed at a large distance of 10 m from the plasma to eliminate the back reaction of the structures on the plasma. The net toroidal wall current and the coil current are shown in figure 4.8, where it can be seen that the coil and wall currents are of equal shape and magnitude. Due to the large distance from the plasma, the different geometries are not important as the variation of the magnetic flux over the structure surface is small.

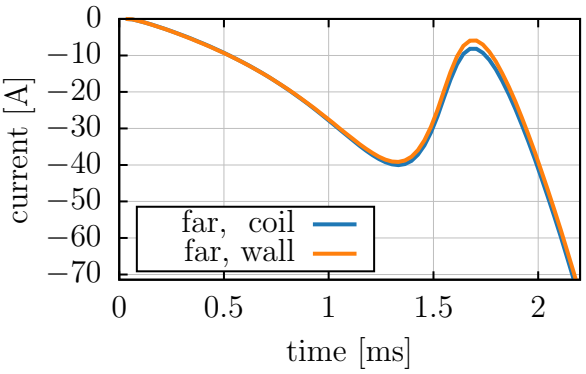

Figure 4.8: Comparison between net toroidal wall current and coil current for the case at large distance from the wall.

Next, the major radial position of the structures was reduced to 2.25 m, close to the JOREK boundary, as shown in figure 4.7. Two different setups were chosen at this position. First, the resistivity was set to a high value of $\eta_{\mathrm{w,thin}} = 3 \times 10^{-2}\,\Omega$ to only allow for small currents, meaning that they have a negligible effect on the plasma. In the second case, the resistivity was decreased to $3 \times 10^{-5}\,\Omega$.

The results in figure 4.9 show that the currents are equal for the high resistance case, while there is a visible deviation for a smaller resistance. Also, it can be seen that the shape of the curve is different and the currents differ in several orders of magnitude compared to the high resistance case.

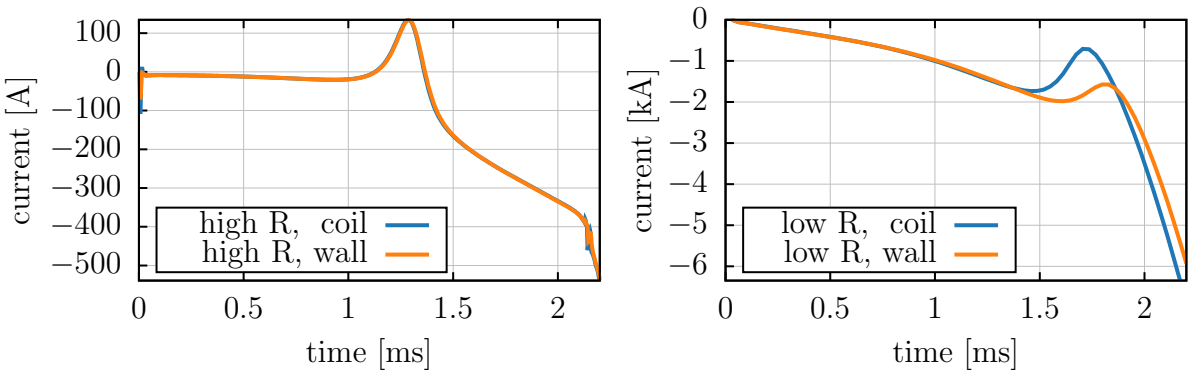

Figure 4.9: In the high resistance case, the coil currents match closely, while there is a visible deviation for the currents in the low resistance case on the right due to the different geometries of the wall and the coil.

The different evolution of the current is due to the effect of the structures on the plasma, which results in a different axis evolution as shown in figure 4.10. Compared to the high resistance case, the velocity of the plasma displacement is reduced by the larger coil currents in the structures. In the low resistance case, the deviation of the induced currents results in a different axis evolution. Note that the growth rate is very large, as neither the realistic wall nor the PSL are present in this case.

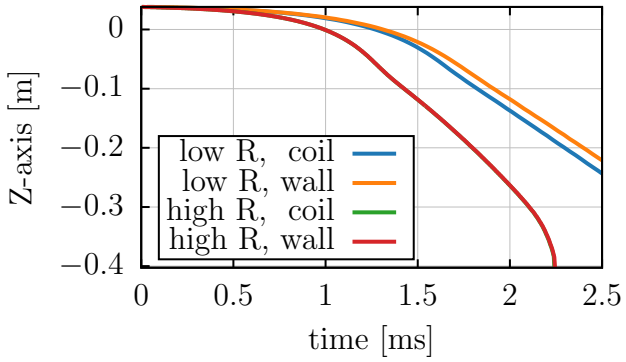

Figure 4.10: Axis displacement for the structures at small distance to the plasma. The deviation in the currents for the low resistance case leads to a different axis evolution.

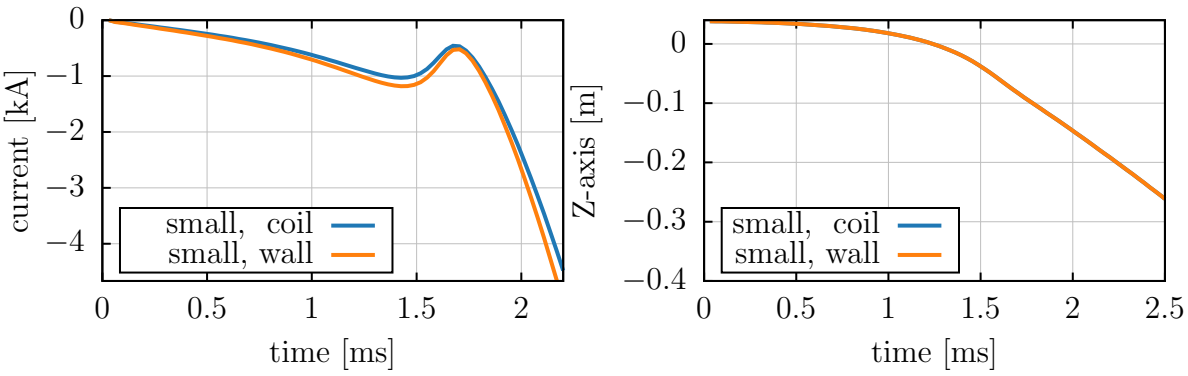

Figure 4.11: When the size of the structures is reduced until the shapes become similar, the current induction and back reaction on the plasma are the same.

These deviations are attributed to the coil and wall geometry. In the large distance and high resistance cases, the different representations play no role because the feedback of the currents on the plasma is negligible. However, when the structures are close to the plasma, it has a larger effect. To show that this is the reason for the deviation, the minor radius a of the wall was reduced as well as the distance between the coil bands to make the geometries more similar. As shown in figure 4.11, the currents now match better and the axis evolution for the case with the wall is the same as for the one with the coil.

These tests prove that the correct current is induced in the coil, as the wall induction has been validated before. Also, the effect on the plasma is very similar for both the wall and the coil, which means that the magnetic field produced by the structures is matching closely.

Flux conservation: This part of the induction validation aims to show that the coil conserves the magnetic flux. The plasma current was quenched to zero, resulting in a change of magnetic flux. An ideal coil conserves the flux exactly as the induced current $\frac{\mathrm{d}I}{\mathrm{d}t}$ is

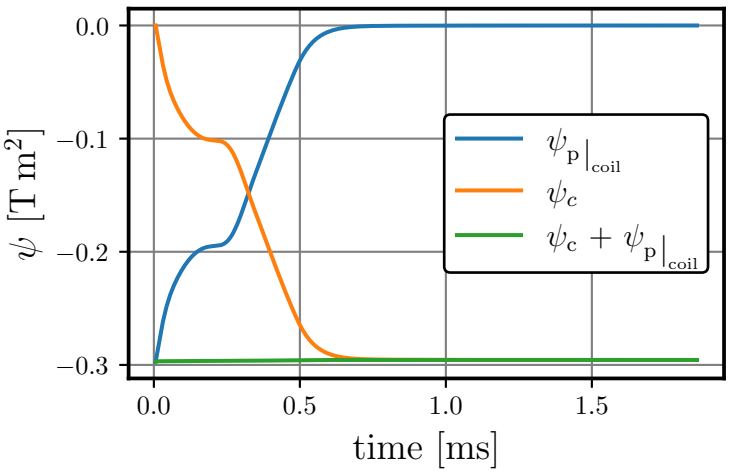

Figure 4.12: The magnetic flux of the coil compensates exactly for the flux change due to the plasma quench.

proportional to the flux change $\frac{\mathrm{d}\Phi}{\mathrm{d}t}$, so that:

$$\frac{d\Phi}{dt} = -L\frac{dI}{dt}, \tag{4.7}$$

where L is the self-inductance of the coil. The magnetic flux of the plasma was calculated by the JOREK function *Psi_at_RZ*, which returns ψ $(= \Phi/(2\pi))$ at any given position. The coil currents of the PF coils remain constant due to the imposed current term and their high resistance, while the wall resistance was increased to suppress eddy currents.

According to equation (4.7), the flux produced by the coil compensates for the flux change of the plasma $\Delta\psi_p$, so that the flux at the coil position is conserved:

$$\Delta\psi_p\Big|_{coil} \stackrel{!}{=} -\Delta\psi_c\Big|_{coil} = -\frac{1}{2\pi}LI_c\Big|_{coil}, \tag{4.8}$$

where the magnetic flux change $\Delta\psi_c$ of the coil is given by the self-inductance L of the coil and its current I_c.

The coil was modelled as a toroidally symmetric passive coil with a small height to ensure that the flux is constant over its surface. The self-inductance was calculated by STARWALL to be 18.4 µH, while the resistance of the coil was set to a low value to avoid resistive current decay. Figure 4.12 shows how the decreasing flux of the plasma is completely compensated by the coil, so that the total flux at the coil position is constant, proving that the coil current is induced correctly.

After this extensive testing, we can conclude that, on the one hand, the induction in the coils by the plasma as well as by current changes in the other coils is correct. On the other hand, the coils produce a magnetic field, which has been validated by comparing it to the analytically calculated field. These coils are essential for the free boundary equilibrium as

well as for active and passive stabilization of the vertical position. Thus, we can now start looking at vertical displacement events in the following sections.

4.2 Benchmark with CASTOR3D

The growth rates of a VDE were benchmarked against the linear, full MHD code CASTOR3D [Str16], which is coupled to a different version of STARWALL. The goal is to validate the influence of the PSL on the vertical displacement by comparing the growth rates for different conductivities.

The **setup** is the following: The equilibrium of the experimental discharge #28848 of ASDEX Upgrade was reconstructed by the code *Cliste* as explained in section 3.1 to be used as a basis for both the JOREK and the CASTOR3D runs. To relate the conductivity used as an input for CASTOR3D to the PSL resistance used in JOREK, the definition of the resistivity was used:

$$\frac{1}{\sigma_{\mathrm{PSL}}} = \eta_{\mathrm{PSL}} = \mathcal{R}_{\mathrm{PSL}} \frac{A}{l}, \tag{4.9}$$

where σ_{PSL} is the specific conductivity, $\mathcal{R}$ the coil resistance, A the cross section and l the length of the coil. The specific conductivity of the PSL is $\sigma_{\mathrm{PSL}} = 56.2 \times 10^6\,\mathrm{S\,m^{-1}}$ given by the material value of copper. For the benchmark, the PSL conductivity was varied over several orders of magnitude from 56.2×10^{-4} to $10^4\,\mathrm{S\,m^{-1}}$. These cases did not include a conductive wall to capture the influence of the PSL only.

The low conductivity region corresponds to the no-PSL limit, as no significant coil currents can occur, while the other limit is close to the realistic PSL conductivity. In the first phase of the displacement, the plasma behaves as described in the three wire model in section 2.2.1, where equation (2.21) shows the dependence of the growth rate on the resistive decay time of the conducting structures.

In CASTOR3D, the scrape off layer consists of a vacuum, while it can contain stabilizing halo currents in JOREK. This difference becomes important, when increasing the PSL

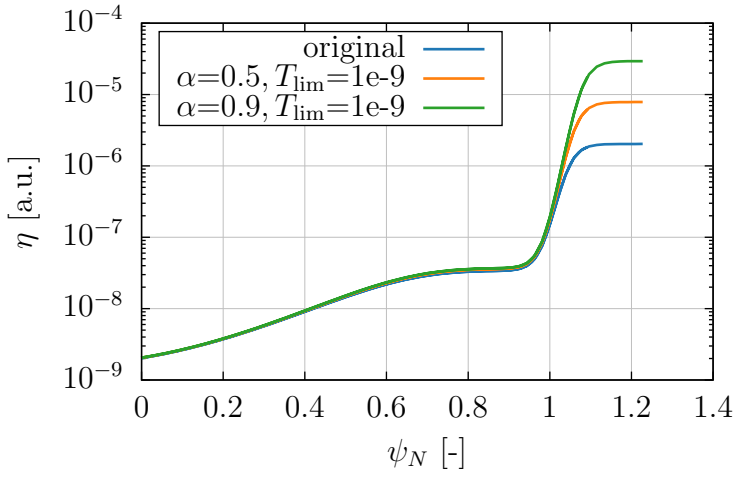

Figure 4.13: The modified temperature for the resistivity calculations increases η in the SOL, while the core is not changed for small values of α.

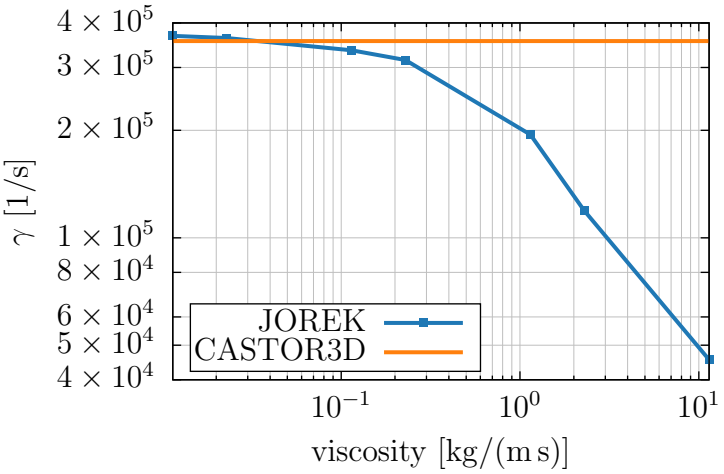

Figure 4.14: Scan over the viscosity in the low conductivity limit in JOREK, which is limited by the plasma inertia. The value of CASTOR3D was added for reference.

resistance until the resistive time of the halo region becomes comparable to the resistive time of the PSL ($\tau_h \approx \tau_{\mathrm{PSL}}$). Therefore, the halo currents must be eliminated by increasing the resistivity of the SOL for the benchmark. As the plasma resistivity η is defined by the temperature in a Spitzer like dependence ($\propto T^{-3/2}$) in the model, it can be regulated by replacing the temperature with an effective temperature T_{eff}:

$$T_{\mathrm{eff}} = T - \alpha T_{\mathrm{bnd}}, \tag{4.10}$$

where T is the local temperature, T_{bnd} the temperature on the JOREK boundary and α a parameter. This results in the resistivity

$$\eta = \eta_0 \left(\frac{T_{\mathrm{eff}}}{T_0} \right)^{-1.5}, \tag{4.11}$$

where η_0 is the central resistivity and T_0 the central temperature at the position of the magnetic axis. The effective temperature is bounded by T_{lim} to avoid negative values and set a maximum limit for the resistivity. The new profile increases η only in the SOL, while it leaves the core resistivity unchanged for small values of α as shown in figure 4.13. In this particular case, without stabilization by a wall, the halo currents influence the plasma already significantly for a PSL conductivity in the order of $10^3\,\mathrm{S\,m^{-1}}$.

In the opposite limit of a highly conductive PSL, a different problem occurs. The plasma current decays rapidly, which shifts the equilibrium and thus, the magnetic axis to another position, which increases the growth rate. The current decay can be reduced by decreasing η in the plasma core and enforcing the current profile to remain constant by an artificial current source as shown in the equations of the model (2.40).

In summary, it is necessary to eliminate **halo currents**, while keeping the current in the

Table 4.1: The parameters used as an input vary for the different PSL conductivities. The low conductivity region requires a high value of η in the halo region, while current decay has to be prevented in the high conductivity region, where the growth rate is small.

	low σ	transient region		high σ
$\boldsymbol{\sigma}_{\mathrm{PSL}}$ [S m^{-1}]	56.2×10^{-4}-10^{0}	56.2×10^{1}	56.2×10^{2}-10^{3}	56.2×10^{4}
profiles	free profiles		fixed profiles	
$\boldsymbol{\alpha}$	5	2		0.5
$\boldsymbol{T}_{\mathrm{lim}}$	10^{-9}		10^{-8}	10^{-7}

plasma core constant to prevent **current decay**. This proved to be difficult because of the large disparity in growth rates between both limits. Thus, it was necessary to set up different cases depending on the PSL conductivity. This is possible because the tuned parameters have no direct influence on the growth rate of the vertical instability.

The parameters for the different setups are given in table 4.1. In principle, the fixed sources can also be used in the low conductivity region, however, the sharp η profile makes this numerically difficult and caused oscillations in the current. As the current decay plays no role on these short time scales, the current source was removed for the low conductivity cases. In this region, the growth rate is limited by the plasma inertia, so that a scan over the viscosity was performed to match the growth rate. At a central viscosity of $\approx$0.22 kg m^{-1} s^{-1}, the growth rate is equal to the value of CASTOR3D as shown in figure 4.14 and does not vary much with a further decrease of viscosity.

Scans of the η profile were performed to ensure the convergence of the growth rate. The results for the low conductivity test are shown in figure 4.15. The growth rate converges at a high value of α, where the η_{SOL} is significantly higher than before. When scanning the limit temperature, one can observe a jump for a high T_{lim}, where the temperature is bounded in

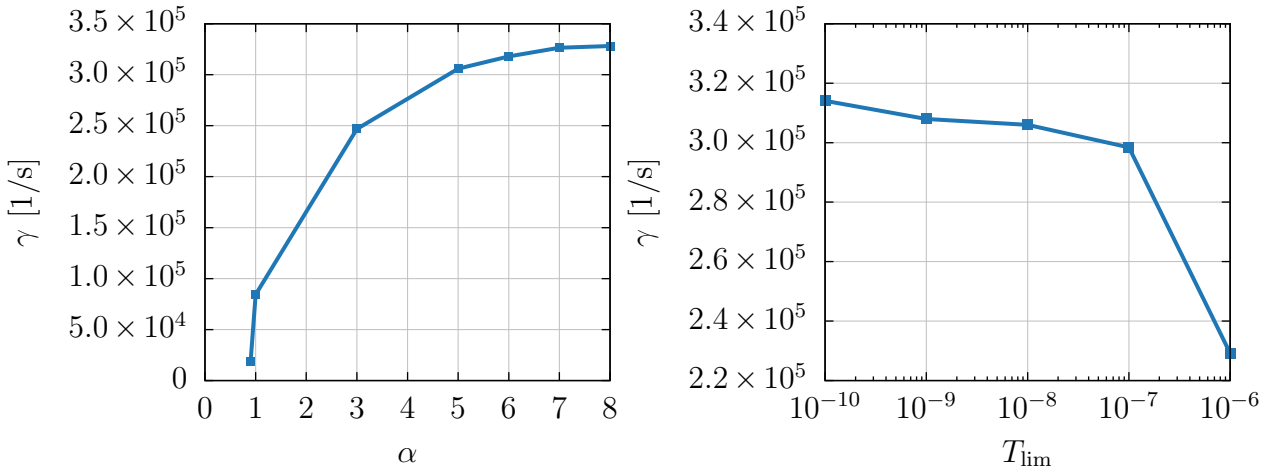

Figure 4.15: The scan over the parameter α (defined in equation 4.10) and the limit temperature T_{lim} in the normalized units of JOREK show that the growth rate is converged in the region of the chosen parameters.

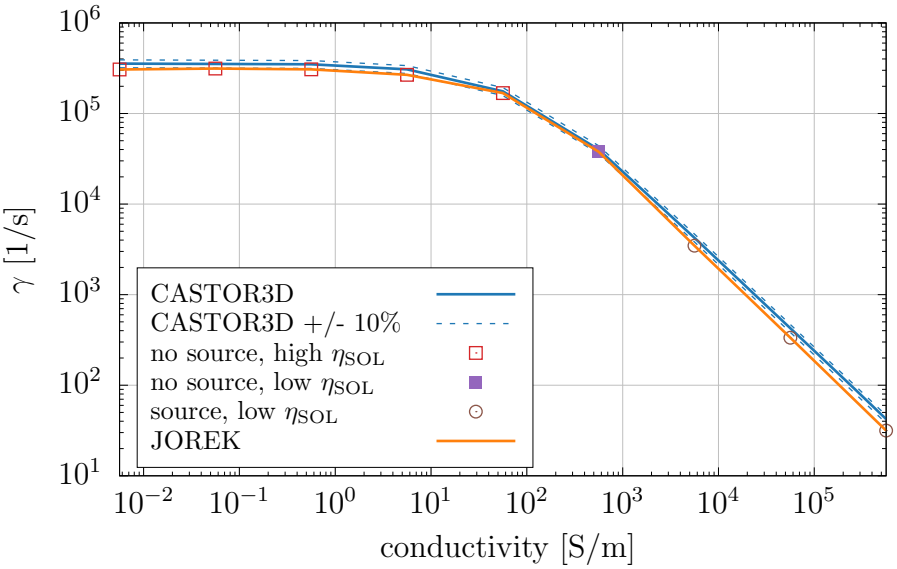

Figure 4.16: The growth rates of CASTOR3D and JOREK match over a large range of PSL conductivities, from the inertial limit to the realistic PSL conductivity.

the whole SOL. For lower values, the growth rate does not change much as T_{eff} is above T_{lim} in most parts of the region. A high η in the halo region does not affect the growth rates for the low resistance PSL in theory. However, due to the way η is defined, a high value of α also affects the resistivity in the pedestal, where the temperature gradient is high. Therefore, it was necessary to use a low α in the transient region to reduce the current decay.

The final result is shown in figure 4.16. This benchmark shows, on the one hand, that JOREK can determine the correct growth rate even on the fast Alfvénic time scale, and on the other, that the growth rate dependence on the PSL conductivity is correct.

4.3 VDE investigations

In the previous sections, we validated the coils and benchmarked the dependence of the growth rate on the PSL conductivity. This section presents investigations of VDEs to assess the dependence on different parameters.

First, we will compare the linear growth rates of the different PSL geometries to show the validity of all three models. Second, the importance of the wall in ASDEX Upgrade is evaluated by varying its resistivity. Finally, the growth rate for different PSL resistances for the setup including a conductive wall are calculated.

4.3.1 Different PSL geometries

In section 3.2, the three different approaches for modelling the PSL in STARWALL were presented and in section 4.1, the resistive decay times of the models were validated against the documentation value. In this section, the VDE growth rates for the different PSL models are calculated and compared to show which models are suitable for modelling stabilizing conductive structures.

As the broad band model of the PSL with ten bands in radial direction was used for the benchmark with CASTOR3D in section 4.2, this model is used as a base line for the comparison of the different geometries. Also, this model will be used in the following sections if not stated differently.

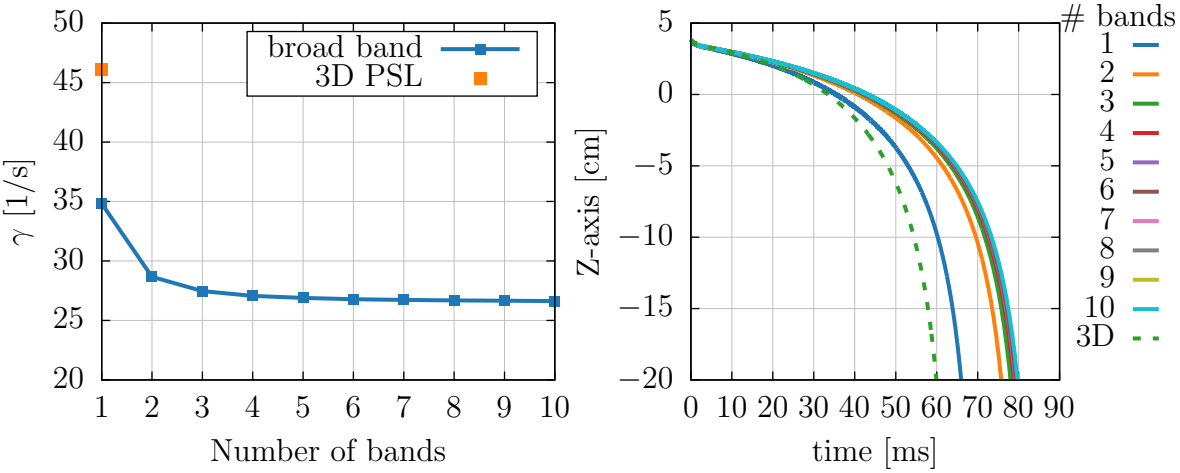

Figure 4.17: On the left, it is shown that the growth rate converges rapidly when more bands are added to the broad band PSL model. On the right, the axis evolution for the different models is shown. For comparison, the 3D PSL model with only one band is added.

First, the effect of the thickness on the growth rate is investigated. The axisymmetric PSL models can represent the thickness of the structure by decomposing it into several layers. For the broad band model, the number of bands in radial direction is increased, while multiple filaments in the radial direction are used for the filamentary model. Figure 4.17 shows how

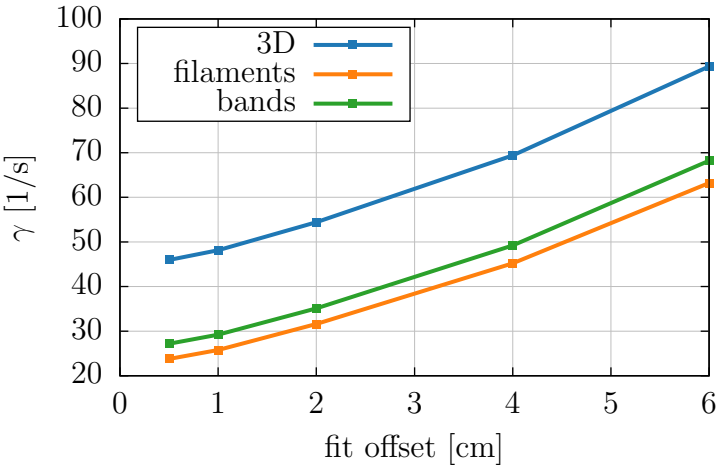

Figure 4.18: The growth rates at different displacements from the initial position are similar for the two axisymmetric coils, while γ for the 3D PSL is about twice as large.

the growth rate converges rapidly, when increasing the number of bands in the broad band model. Thus, the effects by the thickness of the coil is important to obtain the correct behavior. The 3D PSL, which only has one layer in radial direction, was added to the plot for comparison. It can be seen that it is closest to the one band limit of the axisymmetric band model. However, the growth rate is approximately twice as high as the converged value, which can be partly due to the modelling of the bridge in the 3D PSL model in STARWALL.

When comparing the growth rates of the different models directly in figure 4.18, it can be seen that the two axisymmetric models show a similar behavior, while the 3D PSL exhibits a larger growth rate. Figure 4.18 shows the growth rate measured at different displacements from the initial position during the first phase of a hot VDE. The growth rate increases with the displacement of the plasma, as the coupling to the structures, especially to the PSL, becomes weaker.

Despite the different geometries, we have shown before that the resistive decay time of the coils is similar for all cases. As the growth rate depends strongly on this value, a similar growth rate for the models was expected. However, the thickness of the PSL is important for the current distribution in the structure and has an influence on the coupling to the plasma. This cannot be represented with the 3D structure, as it is modelled as a single thin band, so that the growth rate deviates strongly from the other cases.

In conclusions, the multiple band model of the PSL is closest to the realistic PSL, as it has the correct value of the self-inductance, the resistive decay time τ_{PSL} as well as a benchmarked coupling to the plasma. Thus, this model will be used further on for the ASDEX Upgrade simulations.

4.3.2 Dependence on the wall resistivity

The vacuum vessel in ASDEX Upgrade provides only insufficient stabilization of the vertical instability because of its large distance to the plasma, but it still has a stabilizing effect on the growth rate. In the following, the effect of the resistive wall is investigated.

First, the PSL is removed to observe the scaling of the growth rate with the wall resistivity with the results shown in figure 4.19, where the realistic wall resistivity was marked with a vertical, dashed line. In the ideal wall limit, the growth rate tends to zero if it was not limited by the plasma current decay. In the high resistivity limit, the movement is limited by halo currents and the plasma inertia. In comparison with the benchmark case in section 4.2, the maximum growth rate is lower by two orders of magnitude, as the viscosity is larger and halo currents are allowed to stabilize the motion. When the PSL with the realistic resistance of $\mathcal{R}$=23 µΩ is added to the setup, the growth rate decreases by almost one order of magnitude. The intersection of the growth rate curve of the case without PSL with the horizontal, dashed line marks the point, where the PSL becomes more important than the wall.

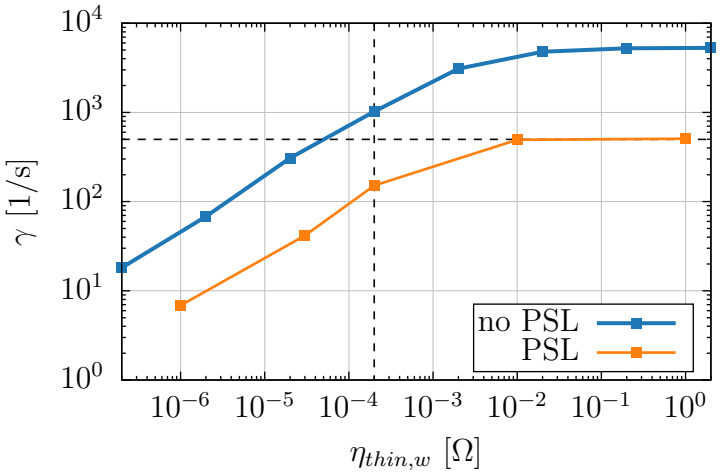

Figure 4.19: Growth rate of the VDE for different thin wall resistivities with and without PSL with the realistic wall resistivity marked with a vertical dashed line. The intersection of the blue curve with the horizontal dashed line marks the point, where the PSL becomes more important than the wall.

Figure 4.20 shows the growth rate for different configurations of the setup at three different wall resistivities as well as with and without the PSL. The value of $\eta_{thin,w} = 3 \times 10^{-5}\,\Omega$ corresponds to the resistivity of stainless steel given the average thickness of 15 mm [Upg] of the vacuum vessel. The other value also takes into account the gaps and bellows of the wall, which effectively increase the thin wall resistivity to $2 \times 10^{-4}\,\Omega$ as measured in AUG [Gia15]. Additionally, the wall was also removed by setting the resistivity to a large value. The difference in the wall resistivities has an important effect on the growth rate and the role of the PSL.

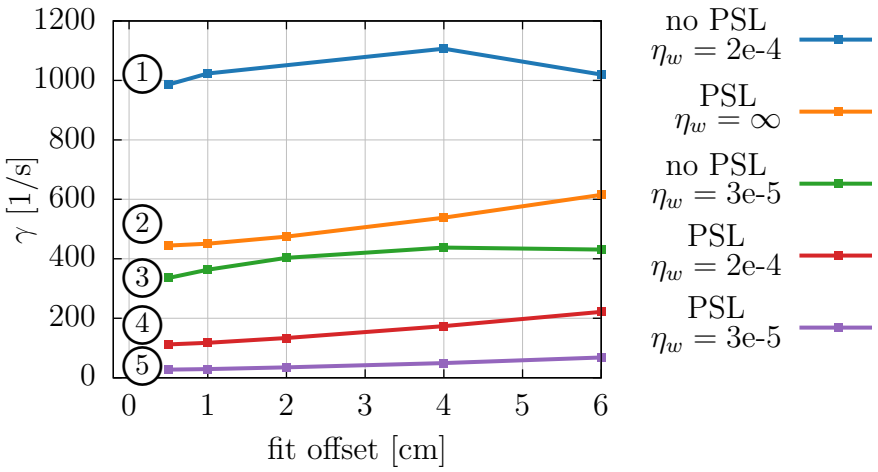

Figure 4.20: To assess the importance of the wall, the PSL was removed at two different wall resistivities and compared to the no wall limit with PSL. When the wall resistivity is high, the PSL is the main stabilizing factor, whereas the wall is more important for a resistivity of $\eta_{thin,w}$=3e-5 Ω.

For the larger value of the resistivity, the PSL is the main stabilizing factor. This can be seen, when comparing the curves (1), (2) and (4) of figure 4.20. Configuration (4) with PSL and wall has the lowest growth rate. When the wall resistivity is increased to the no wall limit (2), the growth rate is increased to ≈500 s^{-1}. When the PSL is removed instead of the wall (1), the growth rate is in the order of 1000 s^{-1}. Thus, the PSL is more important for the stabilization at the realistic resistivity of the vacuum vessel resulting in an $\eta_{thin,w}$ of $2 \times 10^{-4}\,\Omega$.

When using the characteristic value of the material and ignoring holes, etc. (curve 5), the growth rate is lower than when using the larger, measured resistivity (4). When the PSL is removed in this configuration (3), the growth rate is still lower than in the no wall limit (2). Thus, the wall would be more important than the PSL in this scenario.

4.3.3 Dependence on the PSL resistance

The influence of the PSL resistance on the growth rate has been validated against the linear MHD code CASTOR3D in section 4.2 for the case without wall. In this case, we investigate how the situation changes, when a wall is added. The resistance of the 3D PSL was varied over several orders of magnitude at a thin wall resistivity of $3 \times 10^{-5}\,\Omega$ to assess the scaling of γ with the result as shown on the left of figure 4.21.

When including the wall, the growth rate in the no-PSL limit is determined by the resistive decay time of the wall and halo currents, which were not suppressed in this case in contrast to the benchmark. At a high resistance of the PSL, the growth rate matches curve (3) of figure 4.20, where the PSL was not included in STARWALL at all. In the opposite limit of an ideal PSL, the growth rate converges to a value determined by the resistive decay time of the plasma current.

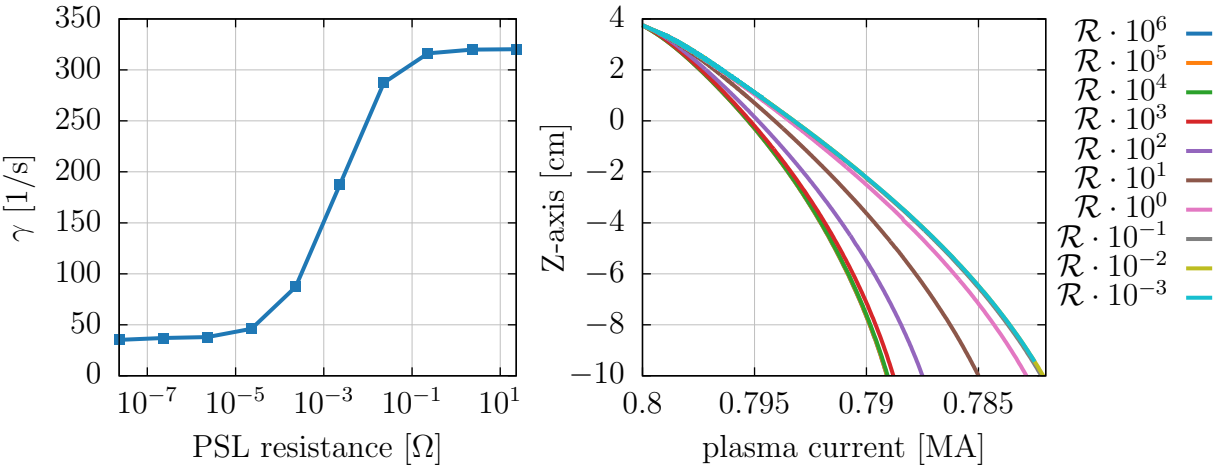

Figure 4.21: Growth rate for different resistances of the PSL in presence of the AUG wall. The resistances are given as a multiple of the realistic PSL resistance.

The right side of figure 4.21 shows the axis evolution against the plasma current for different resistances in terms of the real PSL resistance $\mathcal{R}_{\mathrm{PSL}}$ of 23 µΩ. In the ideal PSL limit, the growth rate is determined by the resistive decay of the plasma current, which can be seen on the right of figure 4.21. When decreasing the resistance, the curves of the vertical position against the plasma current get closer until they reach the ideal limit, where the plasma current decay is faster than the current dissipation in the coil ($\tau_{PSL} \gg \tau_{plasma}$).

In this section, we showed that the most realistic behavior of the PSL can be obtained with the axisymmetric coil models including multiple bands and that the PSL is the main stabilizing factor in the case with a realistic wall conductivity. Only the combination of the wall and the PSL allows to reduce the growth rate of this case to a value of $\approx 100\,\mathrm{s}^{-1}$ for a wall resistivity $\eta_{thin,w}$ of $2 \times 10^{-4}\,\Omega$ and the broad band model of the PSL as shown in curve (4) of figure 4.20. Without the PSL, the growth rate would be 10 times larger as shown in section 4.3.2, where the active stabilization system of AUG would fail. Even at this reduced growth rate, the plasma would reach the wall in several tens of ms as can be seen in figure 4.17 due to the resistive decay of the currents in the conductive structures. To maintain the initial position on a longer time scale, an active stabilization system is indispensable. In the following section, the implemented active stabilization system in JOREK is tested.

4.4 VDE Control

The previous simulations have focused on the passive stabilization of the VDE due to the PSL and the resistive wall (section 4.2 and 4.3), which allows to reduce the growth rate to a time scale, where the active stabilization system can act.

In this section, the implementation of the PID controller in JOREK is tested for different setups. First, the controller properties are evaluated and it is shown that the controller can stabilize the axisymmetric instability as well as prescribe the vertical position of the magnetic axis. Second, the effect of the controller on different plasma equilibria are tested, which differ in their elongation and thus have a different ratio of the stabilizing and destabilizing force f as defined in equation (2.26).

4.4.1 PID controller tests

A PID controller was implemented as described in section 3.3, acting on the fast feedback coils (CoI coils), similar to the one integrated in AUG (see section 1.3.3 for the coil system and 2.3.3 for the control system of AUG). It acts based on the evolution of the vertical axis, which is determined by a search algorithm described in the appendix D. The controller

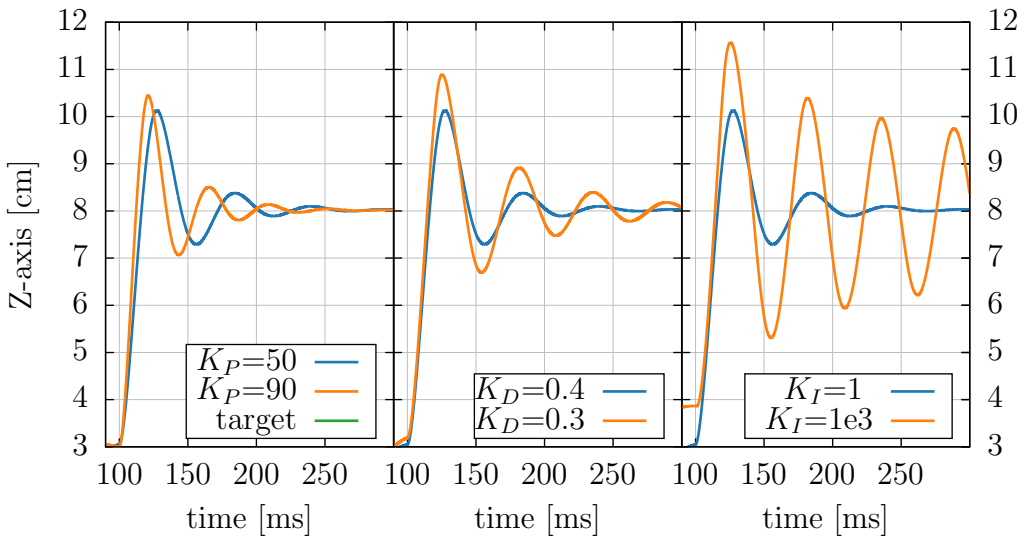

Figure 4.22: Effects on the step response when tuning the gains individually. The target value is increased discontinuously from the equilibrium position of 3 cm to 8 cm to observe the response of the axis. The initial controller gains of $K_{\mathrm{PID}} = 50, 1, .4$ were varied independently to see the effect on the step response. This test was performed with an early implementation of the controller model in JOREK, therefore, the gain settings are lower than for the other tests shown in this section.

in JOREK has two main features, it stabilizes the vertical position of the plasma and also prescribes the position based on an input profile or an analytical expression.

First, the reaction of the controller to a step excitation is investigated to analyze the controller properties described in section 2.3.2 and a first tuning is performed based on

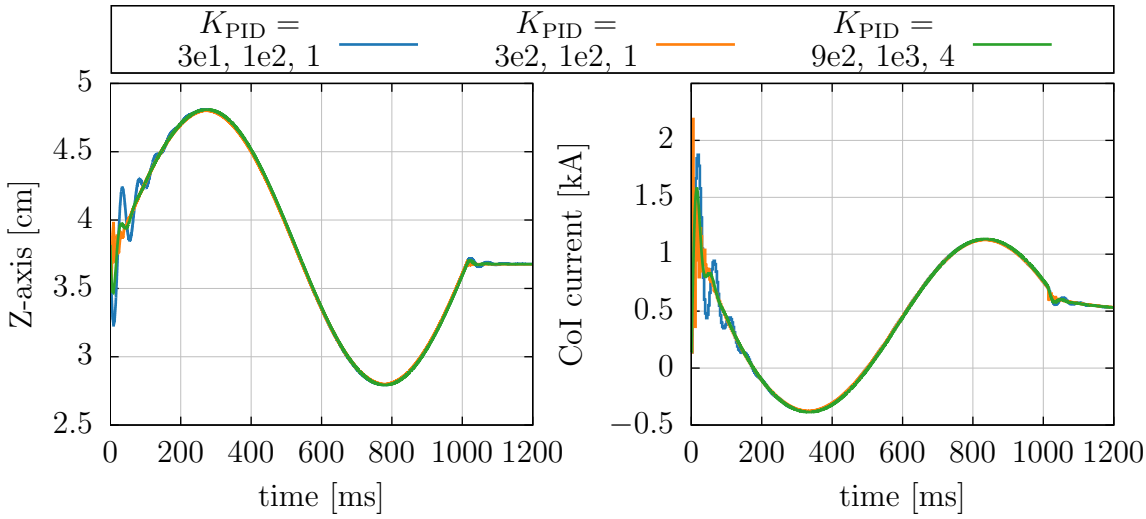

Figure 4.23: The axis can follow a given shape like the sinusoidal oscillation shown in this figure. By increasing the derivative gain, the oscillations around the target values can be reduced. On the right, the corresponding control current is shown.

this example. This is done by first increasing the proportional gain until the axis oscillates closely around the reference position. A high K_P can lead to a larger overshoot as shown in figure 4.22 a), but the settling time is reduced at the same time. Then, the derivative gain is increased to minimize the oscillations around the target value, which can be seen in figure 4.22 b). This allows to decrease the overshoot and settling time of the controller. As a last step, integral gain is adjusted to reduce the steady state error, which was small anyway in the simulations. However, figure 4.22 c) shows how a large integral gain can increase the overshoot and settling time as described in table 2.1. Based on the step response in figure 4.22, we find that the controller has a small overshoot of ≈2 cm depending on the gains, a rise time of ≈10 ms and a negligible steady state error. These characteristics allow a control of the position on a time scale of ms for either stabilization or prescribing the position.

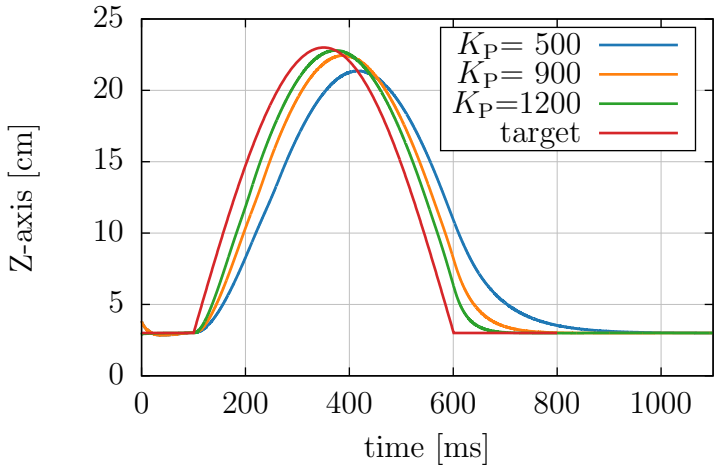

Figure 4.24: When increasing the proportional gain, the prescribed shape can be followed more precisely. In this case, the integral gain and derivative gain were constant with $K_I = 1$ and $K_D = 40$.

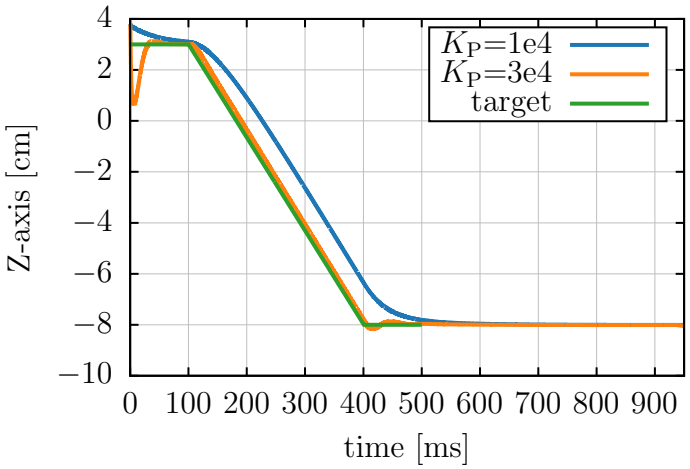

Figure 4.25: The position of the axis can be actively changed by gradually changing the reference position. To void strong oscillations or a loss of control, the change should happen on a reasonable time scale.

The active displacement of the axis position is tested for different cases, before tests for the stabilization of the vertical position are performed in the following sections. Here, the reference position is given as a time dependent input, which is interpolated to the respective time step. The controller gains have to be adjusted to follow the prescribed curve closely by increasing the proportional gain and to minimize the oscillations around the reference profile by a high derivative gain. The change of the position should be made on a reasonable time scale to avoid oscillations. As an example, the position was moved sinusoidally as shown in figure 4.23. The corresponding currents in the upper CoI coil can be seen on the right of the same figure. Here, the smoothing effect of the derivative gain becomes apparent. Another example, where the position was moved over half a period of a sinus is shown in figure 4.24 to investigate the effect of the proportional gain. When increasing K_P, the axis follows the target shape more closely.

Also, the vertical position can be shifted by steadily changing the target value of the axis in a manner as shown in figure 4.25, where the plasma was displaced 10 cm downwards and then fixed at a position of -8 cm. It should be noted that the plasma is only in vertical equilibrium at the new location, while it experiences a net radial force by the vertical magnetic field. To get a steady state, the control has to be extended to the V1–V3 coils to restore the radial force balance. With the present implementation, large excursions from the initial position will ultimately lead to a central disruption, when the plasma touches the side parts of the vessel. In the next section, the controller limits for different plasma elongations are analyzed.

4.4.2 Elongation and shape scan

The VDE growth rate depends on the elongation of the plasma due to the larger required field index n as explained in detail in section 2.2.2. In principle, a controller can keep the plasma in place up to a certain elongation, where it ultimately fails as the coil currents reach their limit or the growth rate is too large for the controller to react. However, the growth rate also depends on other parameters, like the axis position, the internal inductance l_i and the plasma pressure β_p. In this section, we investigate the maximum elongation, which can be stabilized with the JOREK PID controller, when current limits are applied to the coils.

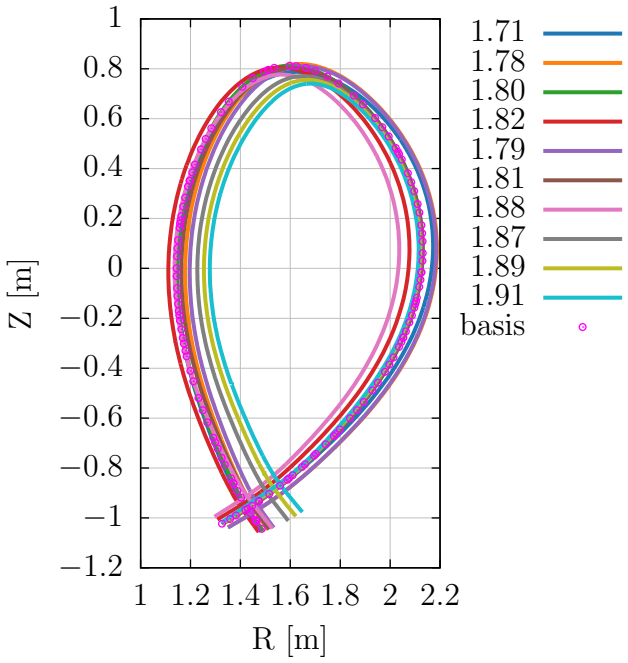

Figure 4.26: The separatrix shapes for the different equilibria are shown. Due to the different currents in the PF coils, not only the elongation changes but also the position of the magnetic axis and the X–point, which can also have an effect on the growth rate of the VDE. The different elongations are listed on the right and the separatrix of the base case is marked.

The current in the V1, V2 and V3 coil pairs were varied to obtain different elongations of the plasma, which resulted in different shapes of the separatrix as shown in figure 4.26. The resulting elongations are in the range from 1.71 to 1.91, where the definition (1.23) of the elongation κ was used. Since the scaling of the currents not only changes the elongation, but also the position of the X–point and magnetic axis, the coupling to the wall and coils also changes. This means that the variation of elongation is not the only influence the growth rate γ in this case. However, figure 4.27 shows that the elongation correlates with the growth rate of the VDE.

For a given equilibrium, it is possible to estimate the ratio between the destabilizing F_d and stabilizing force F_s by approximating the plasma and conductors as thin wires, like it is done in the three wire model in section 2.2.1. This procedure has been applied to various

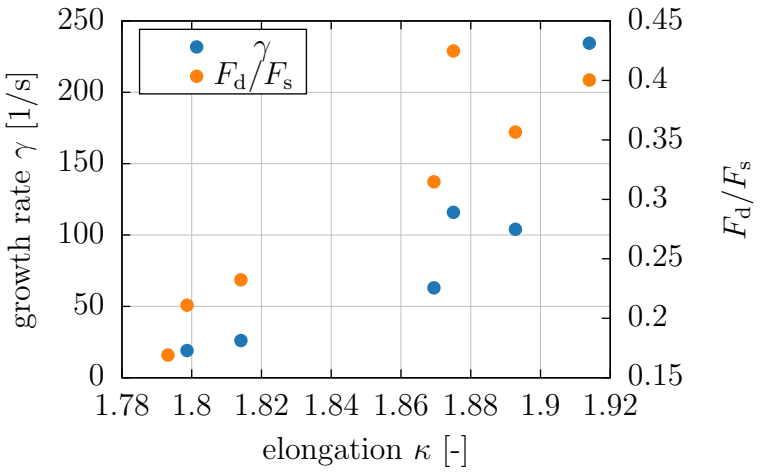

Figure 4.27: The figure shows the growth rate in blue and the ratio between destabilizing F_d and stabilizing force F_s in orange against the elongation κ. The elongation is not the only quantity, that influences the growth rate as the radial axis position is different for the setups. However, the growth rate depends strongly on the elongation because the stability ratio increases with κ.

AUG equilibria in [Seh16]. The same method can be used here to calculate the stability ratio for the different elongations. The result is shown in figure 4.27, where it can be seen that the the F_d/F_s increases with the elongation.

The limitations of the controller model in JOREK were stated in section 3.3, with the most important aspects for this case being the lack of gradient limits on the output currents and of the load distribution among the PF coil types. Furthermore, the JOREK controller acts quasi continuously. Because of these deviations from the experiment, we cannot deduce a quantitative limit of the controller.

Table 4.2: The elongation of the plasma was varied between $\kappa = 1.71 - 1.91$. When the coil current limits are enforced, a VDE occurs for higher elongations

elongation	$I_{max} = \infty$	I_{max} =13 kA	I_{max} =7 kA
1.71	No VDE	No VDE	No VDE
1.78	No VDE	No VDE	No VDE
1.81	No VDE	No VDE	No VDE
1.87	No VDE	No VDE	No VDE
1.88	No VDE	VDE	VDE
1.89	No VDE	No VDE	VDE
1.91	No VDE	VDE	VDE

Despite these simplifications, it was possible to show that the controller can stabilize the vertical position up to a certain elongation depending on the chosen current limits. The maximum currents applied here are below the limits of the experiment because the controller in JOREK reacts faster and continuously. Therefore, it can act in a way that the actual current limits are never reached and was able to stabilize all elongations of this test case.

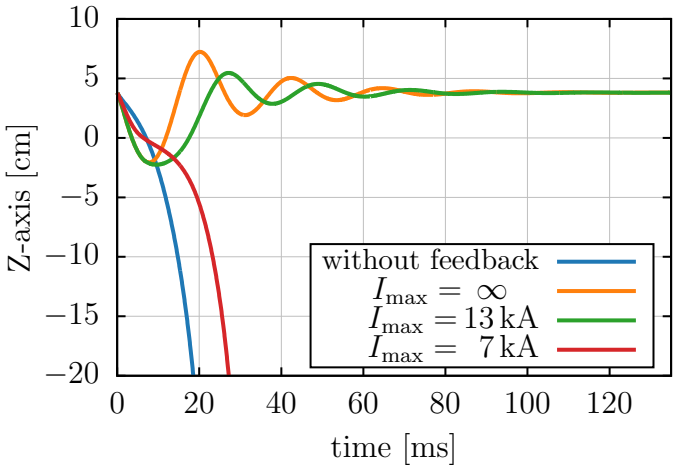

Figure 4.28: With an elongation of 1.89 the controller can stop the VDE for a coil limit of 13 kA, but ultimately fails for a stricter limit of 7 kA

First, the gains were adjusted to stabilize the vertical displacement for all elongations without current limits. Then different current limits were applied to the CoI coils to see in which cases the controller fails and a VDE occurs. The results for different elongations are listed in table 4.2, where the coil current was limited to 13 kA and 7 kA, respectively. While the controller gain setting can keep all configurations stable in the case without limits, it fails above a certain elongation, when coil limits are applied.

There is one outlier in the data at an elongation κ of 1.88, where a VDE occurs for both current limits, while it is again stable for a higher elongation of 1.89. This means that for $\kappa = 1.88$, other factors like the displacement of the magnetic axis compared to the baseline case can play a role. When comparing the radial axis position, we see that, in fact, the $\kappa = 1.88$ case is located 7 cm more inward than the $\kappa = 1.89$ case. As pointed out in section 2.2.3, the coupling deteriorates typically, when the plasma is shifted inward, which is especially true regarding the coupling to the PSL in ASDEX Upgrade. Furthermore, the field index is stronger in this region. Accordingly, the stability ratio shown in figure 4.27 exhibits an outlier for this elongation compared to the other data points. Thus, the different radial location is an indicator for a more unstable equilibrium and explains the discontinuity in the results.

The axis evolution for the case of $\kappa = 1.89$ is shown as an example in figure 4.28. While the controller stabilizes the position for the case without limit and a maximum current of 13 kA, it only slows down the growth rate slightly for the current limit of 7 kA.

It was possible to show that the controller behaves qualitatively as expected, meaning that it can stabilize the position up to a certain growth rate of the vertical instability. This is the case as long as the plasma stability ratio is not too large, meaning that it does not exhibit an extreme elongation or is placed too far from the conductive structures. Apart from the steady state plasma control, the controller behavior in case of a disruption is of interest, as these events are often followed by a VDE. The following section will investigate the controller limits for an artificially triggered disruption.

4.5 Artificial thermal quench

In section 2.2.3, it was described how a thermal quench can trigger a VDE. The plasma is shifted inward due to the pressure drop and the plasma current decays because of the enhanced resistivity. These effects destabilize the vertical position and finally lead to a VDE. As a first small step towards a full disruption simulation, a thermal quench is induced artificially by increasing the perpendicular heat and particle diffusion coefficients $\kappa_\perp$ and $D_\perp$, which results in a loss of thermal energy. This section shows the effects of different CQ times on the dynamics of the VDE and employs the controller to stabilize the vertical position during the CQ.

Here, the thermal quench is characterized by the final temperature as well as the time scale of the energy decrease. The former is determined by the Dirichlet boundary condition on the temperature in our simulations, which was varied from 2.5 to 56 eV to influence the rate of the current quench via the temperature dependent resistivity ($\eta \propto T^{-3/2}$). The latter was controlled by the transport coefficients to be in a range from ≈0.05 to 5 ms as it is observed in the experiment. The flattening of the temperature profile within some ms can be seen in figure 4.29 a) for $T_{\text{final}} = 5.3\,\text{eV}$ and the longest TQ rate.

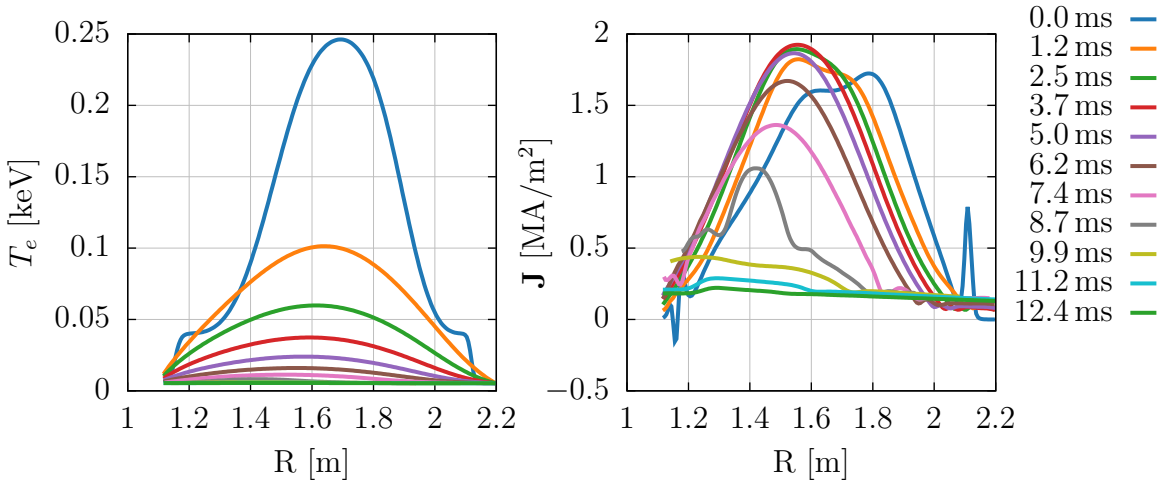

Figure 4.29: The flattening of the temperature profile takes place in less than a ms after its start at 0 ms, which leads to a flattening of the current profile on a slightly longer time scale.

The subsequent current quench takes place with a rate of tens of ms depending on the resistivity set by the final temperature. The loss of thermal energy and current for different final temperatures is shown in figure 4.30 for the case with $\tau_{\text{CQ}} = 0.5\,\text{ms}$. It can be seen, that the current starts to decay rapidly after a large part of the thermal energy is lost. The linear CQ time $\tau_{CQ_{80}}$ defined in equation (2.30) varies from 5 to 160 ms depending on the post TQ temperature as shown in figure 4.31 a). Whereas the different transport coefficients do not affect the CQ rate significantly, but only shift the onset of the CQ in time. During the TQ, the current density profile is shifted radially with the plasma as shown in figure 4.29 b)

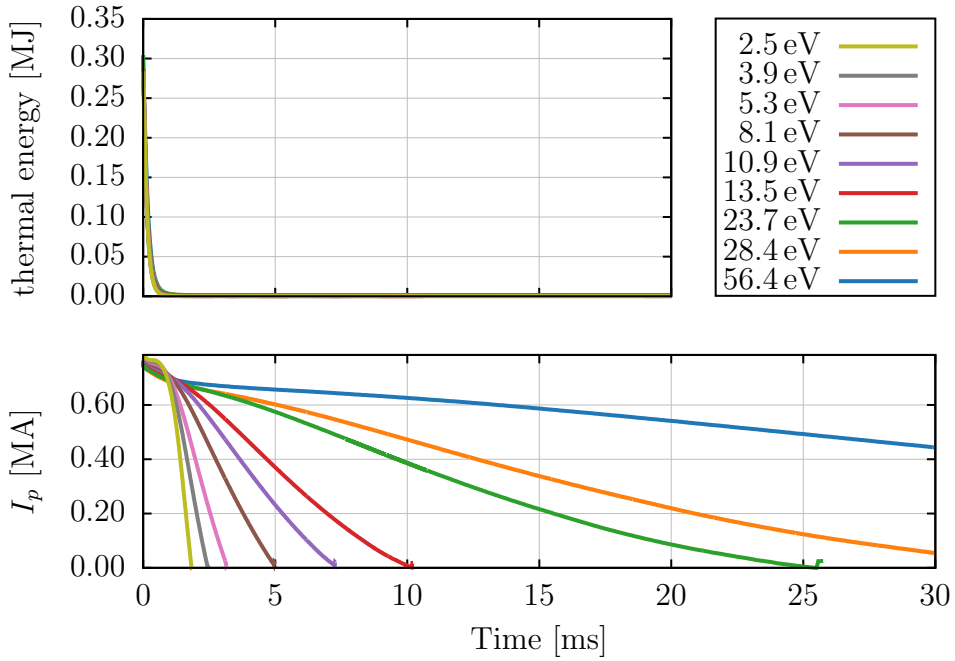

Figure 4.30: The thermal quench takes place on a time scale of less than a ms, determined by the transport coefficient. The subsequent current quench due to the increased resistivity takes place on a time scale of 5 to 160 ms depending on the post TQ temperature.

and becomes more peaked at the same time. This is a contradiction to the experimental observations, which show a flattening of the current profile due to the thermal quench. The difference can be explained by nature of the simple artificial TQ considered here, which keeps the flux surfaces intact. The current density profile then decreases with the start of the CQ.

The displacement velocity of the magnetic axis was measured by the time it takes for a displacement of 20 cm after the current has reached 80 % of its initial value, with the results presented in figure 4.31 b). As expected, the rate of the CQ strongly influences the VDE rate, while the TQ rate does not have a large effect. When the decay rate of the plasma current becomes larger than the resistive decay time of the wall and PSL $\tau_{CQ} \gg \tau_w$, the wall currents dominate the VDE growth rate.

In the ideal wall limit $\tau_{CQ} \ll \tau_{wall}$ and for constant current profiles, the axis position is a function of the plasma current I_p only as described in section 2.2.3. After the thermal quench, the final temperature and thus, the resistivity are uniform, so that the plasma position only depends on the plasma current as shown in figure 4.32, where the resistivity of the wall and PSL were set to a small value.

Figure 4.33 shows the evolution of the plasma current in arbitrary units for the case with $\tau_{TQ} = 50\,\mu s$ ($D_\perp = 1.6 \times 10^3\,m^2\,s^{-1}$) and $\tau_{CQ} = 2.2\,ms$ ($T_{final} = 5.3\,eV$) during the current quench phase with the LCFS and the magnetic axis marked in black. In the first row, the VDE without active control is shown, while the second row shows the effect of the controller on the plasma displacement. Before analyzing the effects of the controller, the evolution

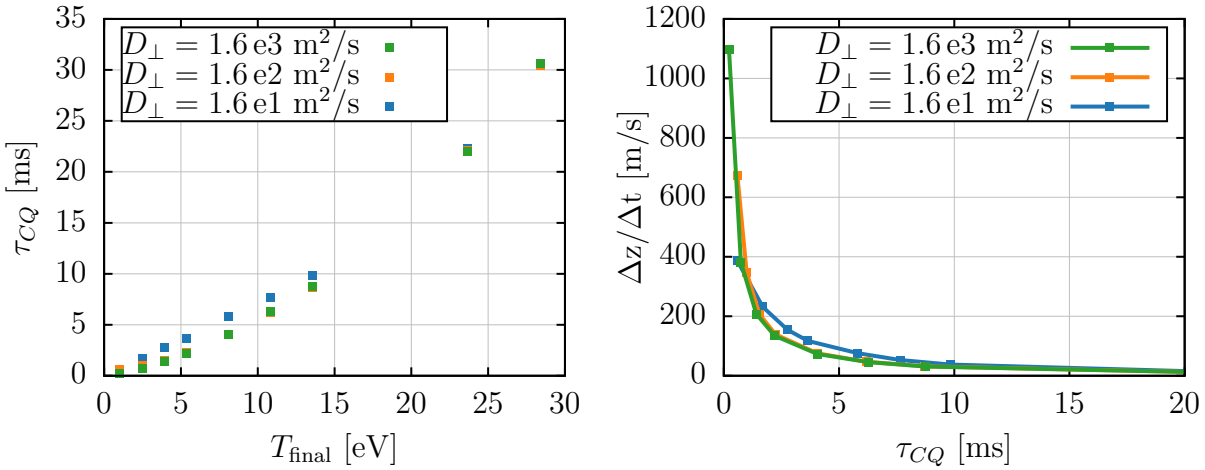

Figure 4.31: On the left, the dependence of the CQ rate τ_{CQ} on the final temperature is shown for different TQ rates. On the right, it can be seen how the current quench time determines the growth rate of the VDE until the resistive time scale of the wall is reached, which then dominates.

of the plasma without active stabilization is described. The different phases of the VDE as lined out in section 2.2.3 can be observed here. In the first frame of 0.1 ms, the magnetic axis is shifted slightly inward to a position at a larger distance from the conducting structures as a result of the pressure drop during the TQ. After 1 ms, the plasma current at the core is already reduced to half of its initial value and the vertical position has shifted downward by ≈9 cm. During the current decay, the plasma moves downward until it comes into contact with a limiting surface and transitions from an X–point to a limiter bound plasma. The simple case considered here evolves axisymmetrically, so that instabilities, which are usually excited at this stage, cannot be observed. Due to flux conservation and plasma current decay, halo currents are induced outside the LCFS.

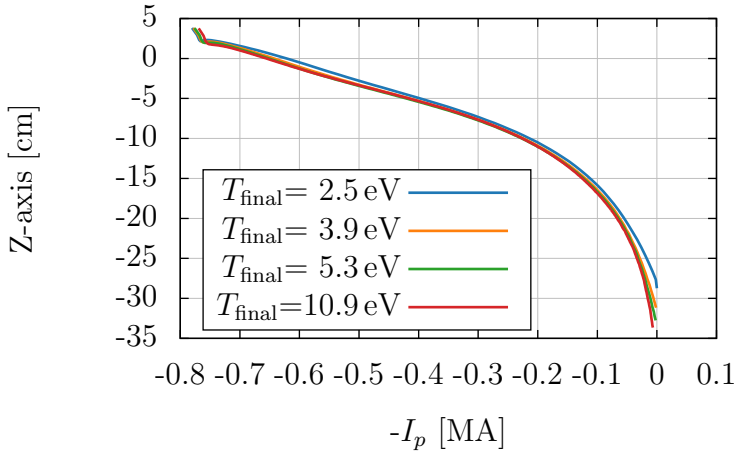

Figure 4.32: If the resistive time of the structures is above the current quench time ($\tau_{CQ} \ll \tau_w$), the axis position is a function of the plasma current even for widely different current quench times.

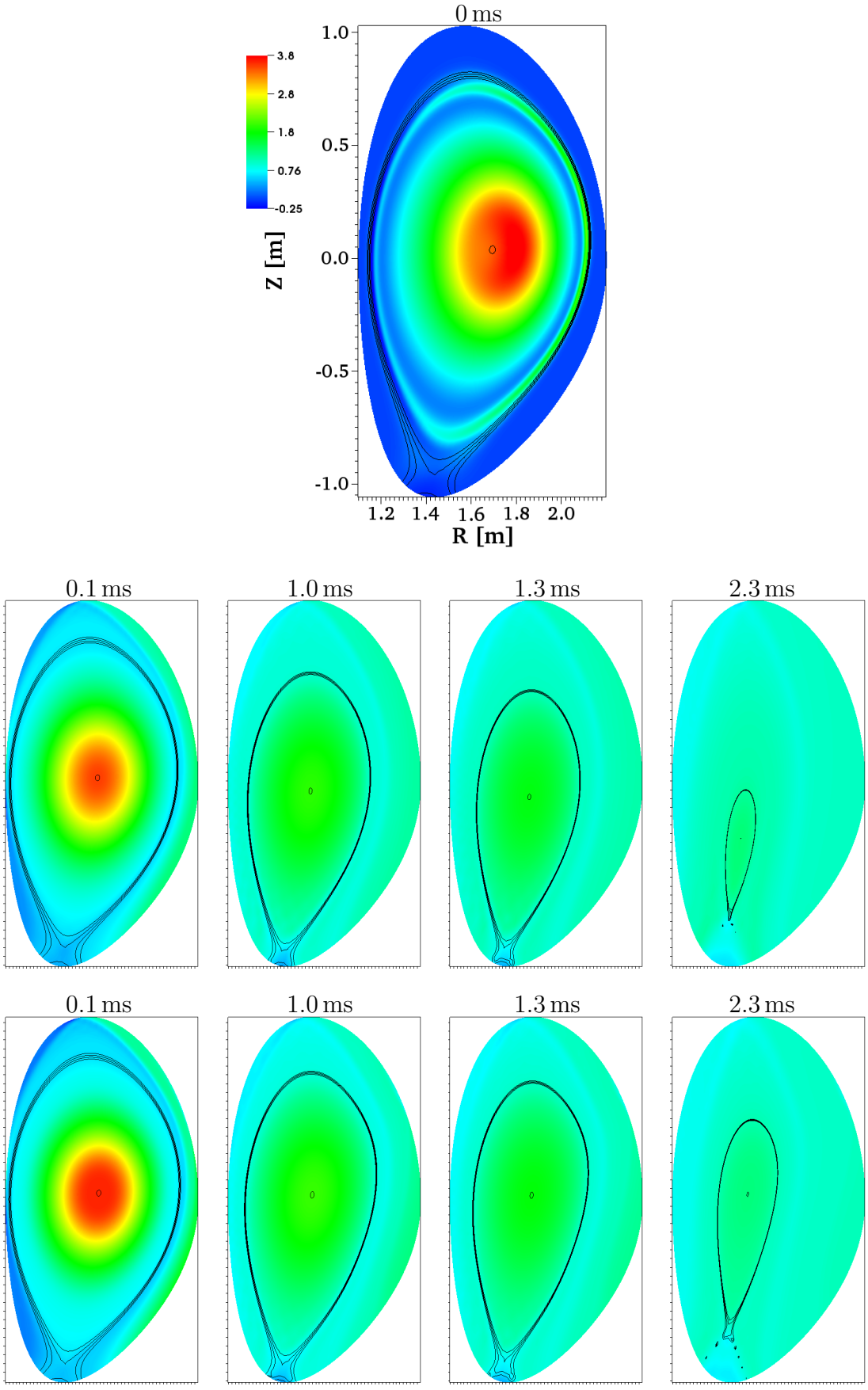

Figure 4.33: When the controller is applied during the current quench, the vertical position can be maintained and the plasma cross section does not decrease as rapidly. The colors indicates the magnitude of the current in arbitrary units.

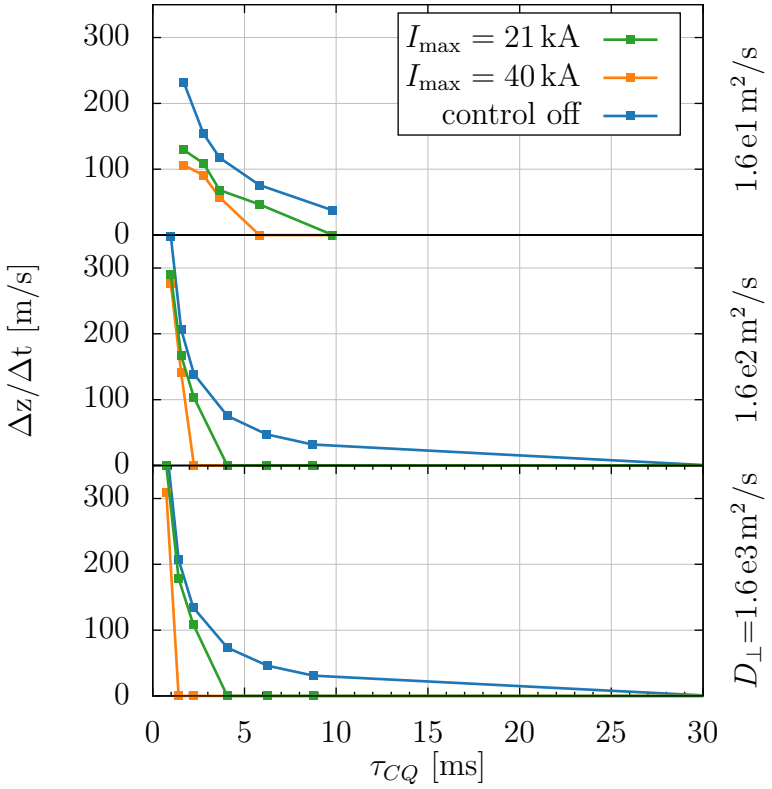

Figure 4.34: The controller can stabilize the vertical position of the plasma up to a certain current quench time τ_{CQ} depending on maximum current in the control coils. A displacement velocity of 0 indicates that the controller could keep the magnetic axis fixed until the plasma current was quenched completely.

When employing the controller, the VDE rate should be either reduced or stabilized completely depending on the CQ rate. As stated in section 3.3, the controller is not fully realistic and thus, cannot be compared 1:1 to experimental data, which means that only qualitative conclusions can be drawn hereC.

In figure 4.34, it can be seen how the active control reduces the displacement velocity for different coil current limits of the CoI coils compared to the case without control. A displacement velocitiy of zero indicates that the controller was able to stabilize the position until the plasma is quenched completely. The maximum coil current of the CoI coils was set to 21 kA and 40 kA, which sets the threshold of the minimum τ_{CQ} that can still be stabilized. For the larger limit, the controller was not able to stabilize the VDEs below a CQ rate of 5 ms, while it failed below a τ_{CQ} of 12 ms for the smaller limit of 21 kA.

The second row of figure 4.33 shows the effect of the controller on the plasma during the current quench phase. After 0.1 ms the plasma is already radially displaced compared to the equilibrium like in the case without control. In the following frames, the plasma moves downward, when the controller is not active. Whereas it stays in the midplane, when the controller is turned on and the plasma cross section does not shrink as rapidly, which is favorable for keeping the edge safety factor high.

Note that there are substantial halo currents in the whole scrape-off layer for both cases, which have a stabilizing influence on the VDE. In reality, however, these currents are limited by the so called ion saturation current. As a consequence, the halo width is reduced. This boundary condition has been implemented in JOREK only very recently [Art20b], so that the halo currents are not realistic in this case.

This first case, despite including only a simple plasma model and a 2D VDE evolution, can reproduce some of the behavior observed in the experiment, like the scaling of the displacement velocity with the current quench rate and the stabilization by a magnetic controller. As a next step to a more realistic model of a disruption, we set up a case including 3D effects and a more consistent thermal quench in the following section.

4.6 Thermal quench by Massive Material Injection

In the previous section 4.5, a thermal quench was triggered by artificially increasing the perpendicular transport coefficients, leading to a loss of thermal energy, which ultimately causes a VDE due to the subsequent current quench.

In this section, we get one step closer to a realistic disruption simulation by adding more Fourier harmonics to include 3D effects and by triggering the thermal quench in a physically more consistent way by massive material injection. This method, inducing a thermal quench by the injection of particles with frozen pellets, consisting either of impurities like Ar or Ne, or of deuterium, is part of the disruption mitigation system foreseen in ITER. The termination of the plasma by this method decreases the thermal loads on the plasma facing components by radiation and is supposed to suppress the creation of runaway electrons (see [Bre19]).

Here, the massive material injection is modelled in a simplified way by a localized, artificial density source placed on a rational surface, which rapidly expands along the field lines due to parallel particle transport. As the simplified, reduced MHD model introduced in section 2.4.1 does not include the parallel velocity, the transport is modelled by a parallel diffusion coefficient $D_\parallel$. Numerically, the density source is represented by S_ρ in the equations (2.40) of the JOREK model. It can be described by a four-dimensional Gaussian distribution:

$$S_\rho(R,Z,\phi,t) = \frac{\Delta S_\rho}{(2\pi)^2 \Delta R \Delta Z \Delta\phi \Delta t} \exp\left(-\frac{(R-R_0)^2}{2\Delta R^2} - \frac{(Z-Z_0)^2}{2\Delta Z^2}\right) \exp\left(-\frac{(\phi-\phi_0)^2}{2\Delta\phi^2} - \frac{(t-t_0)^2}{2\Delta t^2}\right), \tag{4.12}$$

where ΔQ^2 is the variance in the respective dimension, Q_0 is the center of the distribution and ΔS_ρ is the total amount of injected particles. The size of the source was chosen to increase the initial particle content by a factor of five during an injection period of $\Delta t \approx 0.3\,\mathrm{ms}$, leading to a rise from $\approx$0.8 to 4×10^{21} particles inside the plasma region. It was placed at a major radius R of 1.95 m on the Z-axis, which corresponds to the $q = 2$ surface. The extent in the poloidal plane is $\Delta R = \Delta Z = 10\,\mathrm{cm}$ in each direction and it covers over $\Delta\phi = 1\,\mathrm{rad}$ in the toroidal direction, with the simulation having a toroidal resolution of 0.19 rad. The two simulation cases presented here included the toroidal harmonics $n = 0$ to 4 or 8, respectively.

Figure 4.35 shows the density evolution on the $q = 2$ surface, on which the source was placed, for two different times during the injection. On the field lines passing through the injection point, the density is higher and successively increases on the rest of the flux surface. At the end of the injection period, the final density is around 5 times higher than before, consistent with increase of the number of particles. The second row shows the temperature decreasing adiabatically with the rising density. Due to the temperature dependent resistiv-

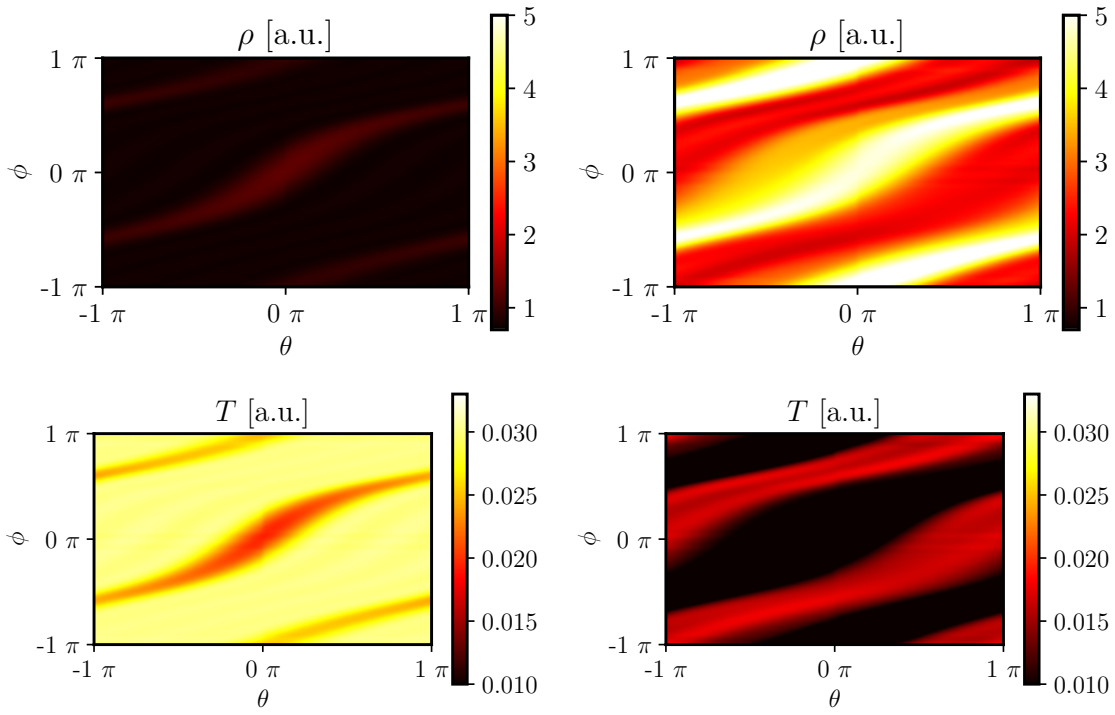

Figure 4.35: The density source is placed at $\theta = \phi = 0$, from where it spreads across the flux surface. The $m = 2, n = 1$ structure of the $q = 2$ surface can be seen here. After 0.16 ms (on the right), the density on the whole surface has increased. The temperature decreases accordingly as shown in the bottom row.

ity, $\eta \propto T^{-\frac{3}{2}}$, the region of larger density contains helical current perturbations, which leads to a reconnection of magnetic field lines and the formation of magnetic islands.

This reconnection process is represented in the Poincaré plots of the magnetic field lines in figure 4.36. Before the injection of the particles, the plasma is in equilibrium, forming nested flux surfaces at the time of 0 ms. The current perturbations in the high density, low temperature regions lead to the formation of magnetic islands, first on the $q = 2$ surface and subsequently also on other rational surfaces after 0.03 ms. Inside the island regions, the magnetic field is stochastic, which can be seen from the blank spots in the Poincaré plots. The rising energy of the different mode numbers shown in figure 4.37 is associated with growth of the islands on the various rational surfaces. Because of the increasing island width and eventual overlap until a large part of the plasma core becomes stochastic, the radial particle and heat transport is enhanced, which ultimately leads to the loss of the thermal energy on a fast time scale – the thermal quench. The first Poincaré plot in the second row of figure 4.36 at 0.16 ms displays the stochastic field lines in large parts of the plasma, which fits to the time of the TQ onset, shown by the thermal energy evolution in figure 4.38 a). The decay of the islands as a result of the complete stochastization can be seen from the decrease in energy associated with the different mode numbers in figure 4.37.

The density distribution in the poloidal plane for the toroidal location $\phi = 0°$ and 180° can be seen in figure 4.39 at 0.3 ms, where also the 3D nature of the perturbation becomes

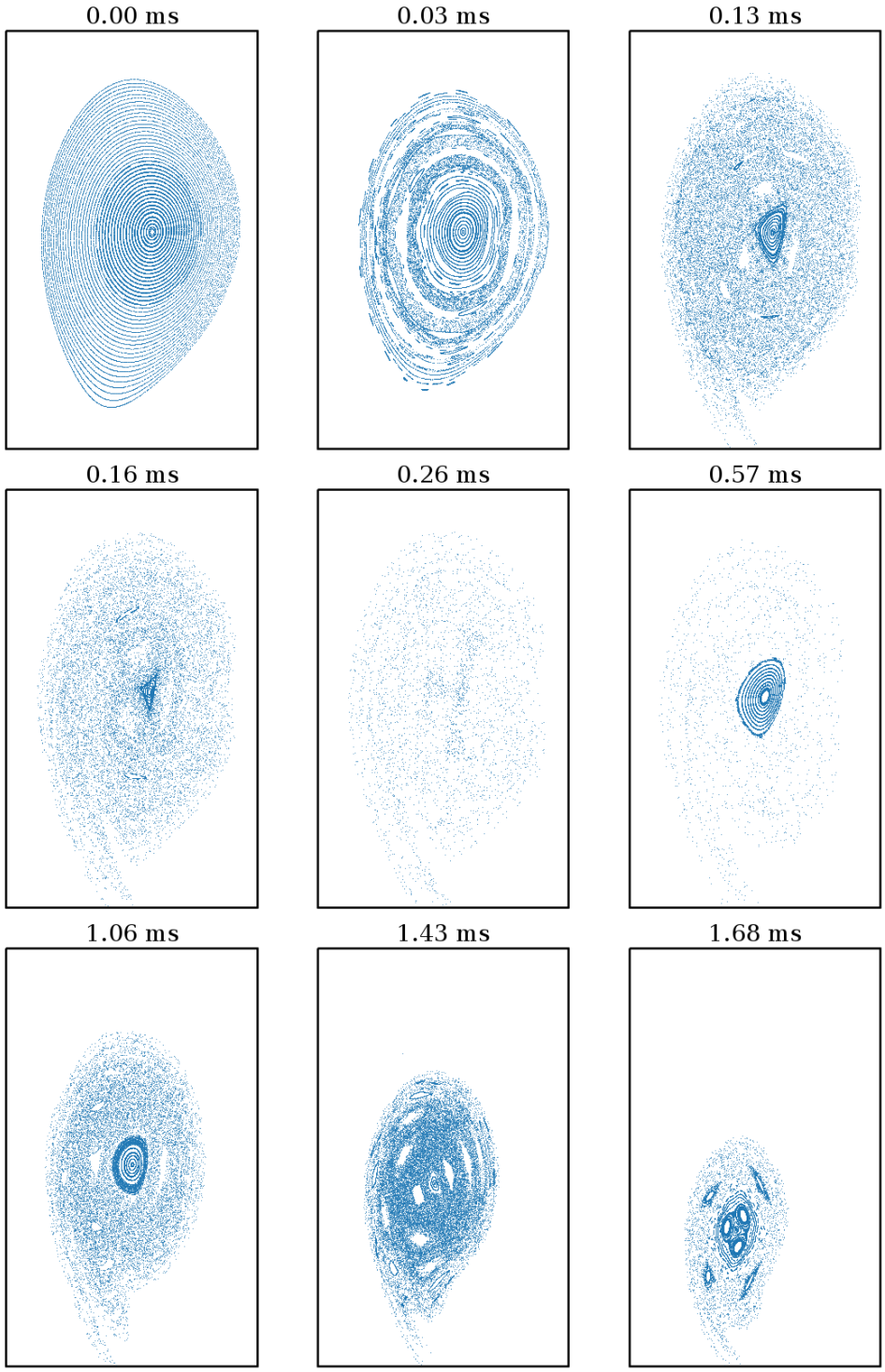

Figure 4.36: The Poincaré plots of the magnetic field lines show the formation of the magnetic islands and the stochastization of the magnetic field lines. After the full stochastization a closed flux surface region reappears starting from the core.

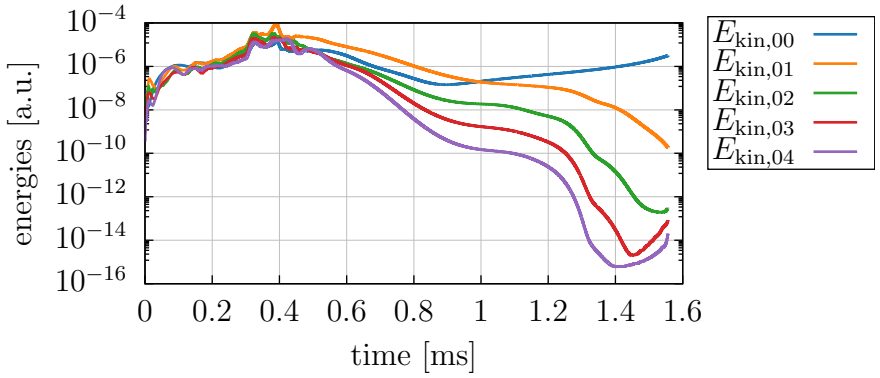

Figure 4.37: The increasing energy of the different modes is associated with the growth of the magnetic islands due to the current perturbation. When the plasma is fully stochastic, the energies reduce, except for the $n = 0$ energy, which increases due to the vertical plasma motion.

visible. At this point, the field lines are already stochastic, leading to a large radial transport in the whole plasma. Accordingly, the density in the whole plasma is substantially higher, with an increase from 1 to up to 5 in arbitrary units.

At the point, where the plasma becomes stochastic, the thermal quench occurs on a fast time scale of less than 1 ms, as represented by the loss of the thermal energy in figure 4.38 a), which is followed by a current decay on a time scale of ≈1 ms in part b) of the same figure. Before the onset of the current quench, the plasma has already slightly shifted downward due the shift of the equilibrium during the thermal quench. As a consequence of the subsequent current quench, the vertical stability is lost and a VDE occurs, resulting in a fast vertical downward movement shown in figure 4.38 c), which is associated with the increase of the

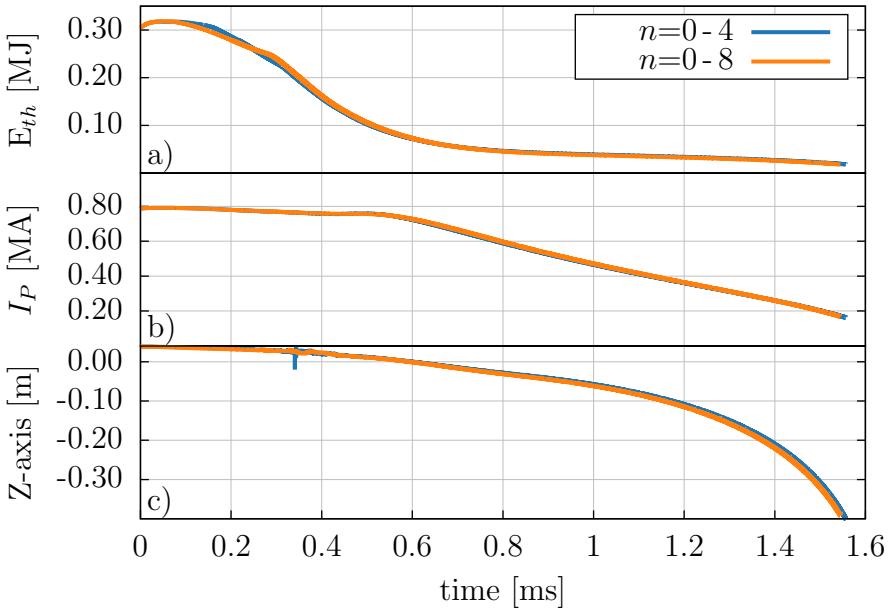

Figure 4.38: The thermal energy is lost in less than a ms, leading to a decay of the plasma current due to the increased resistivity. This, in turn destabilizes the vertical position, ultimately resulting in a VDE on a time scale of 1 ms.

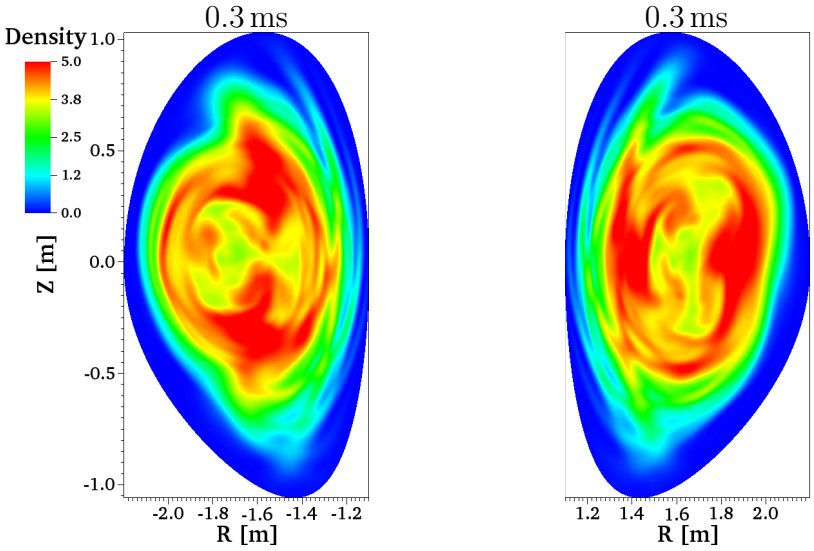

Figure 4.39: The density at 0.3 ms has already increased in the whole plasma. The plot on the left shows the plane at ϕ =180° and the one on the right at 0°.

kinetic energy of the $n = 0$ mode in figure 4.37. The evolution of the density during the downward motion can be followed in figure 4.40, where it can be seen that the three dimensional structures are still clearly visible at 0.6 ms. Afterwards, with the island decay and the stochastization of the the magnetic field, the plasma becomes more uniform and part of the density is lost. While the outer layers stay stochastic, a closed flux surface region reappears in the center of the plasma in the second row of figure 4.36 at $t \approx$ 0.5 ms after the magnetic field has become fully stochastic, resulting in a slowing down of the TQ. The re-formation of the flux surfaces and the shrinking area during the VDE leads to a fresh increase of the density. The plasma reaches the wall around 1 ms after the onset of the CQ.

This simulation of a complete disruption followed by a VDE concludes the presentation of the work of this thesis. In the following chapter, the results of the thesis are summarized and an outlook about future work is given.

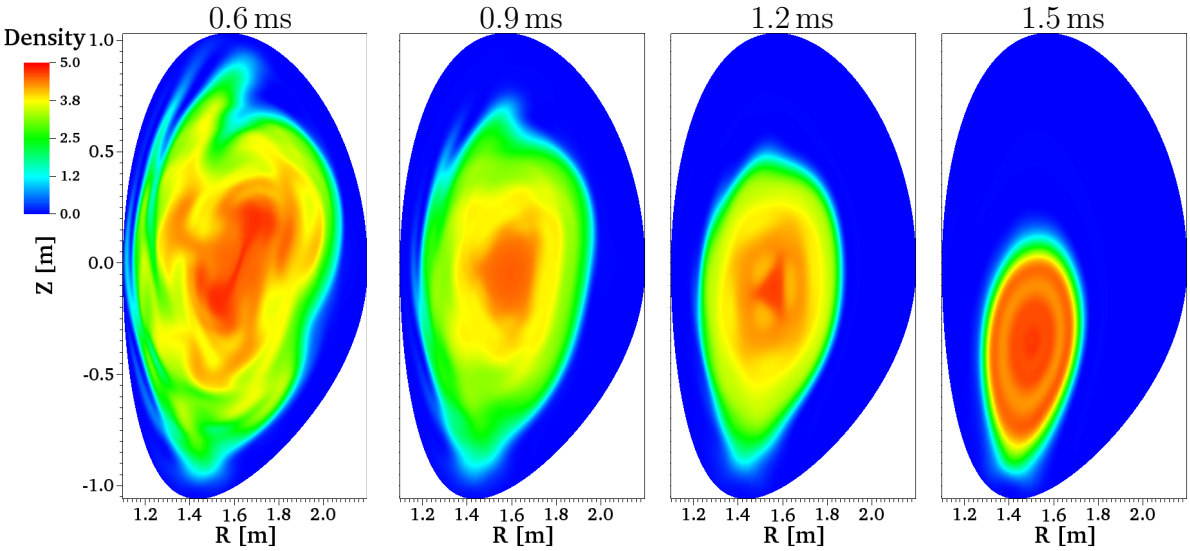

Figure 4.40: The evolution of the density after the thermal quench is shown, where it can be seen how a closed flux surface region forms again and how the plasma moves downward during the VDE.

5 Summary and Conclusion

Towards the goal of this thesis, namely providing the basis for realistic simulations of VDEs in ASDEX Upgrade with JOREK, the following steps were taken.

First, the **axisymmetric coil model in JOREK was validated** in section 4.1, including the interaction between coils, the magnetic field produced by active coils and the resistive decay time of the passive coils. Furthermore, the interaction of passive coils with the plasma was validated by verifying that the correct current is induced by the plasma in passive coils. These investigations were necessary, as the passive coil is crucial for the stabilization of the axisymmetric mode in ASDEX Upgrade and passive coils for stabilization have not been used in JOREK before.

Also, the **benchmark of the VDE with the linear code CASTOR3D** in section 4.2 showed the correct dependence of the growth rate depending on the PSL conductivity. From this, we can conclude that the interaction between the plasma and the passive coil works correctly. Furthermore, it was possible to show that JOREK can even capture the VDE dynamics on the fast Alfvénic time scale.

With this validation as a basis, first simulations of VDEs in ASDEX Upgrade including the realistic wall and PSL were carried out in section 4.3. The **different coil representations** of STARWALL were compared with the result that the PSL model consisting of multiple broad bands matches best with the true, experimental PSL, regarding the resistive time scale for the current decay and the coupling to the plasma. It was found that the thickness of the coil cannot be neglected in the model, as this would deteriorate the coupling of the coil to the plasma. Thus, the axisymmetric coils, which can represent the thickness of the coil, despite the thin wall approximation in STARWALL, provide the most realistic behavior.

Furthermore, the importance of the wall in ASDEX Upgrade was assessed with the conclusion that, with a realistic wall resistivity (including the effect of holes, etc.) as measured in the experiment, the PSL is mainly responsible for the stabilization of the VDE. Without the PSL, the measured growth rates were ten times larger and beyond the stability range of the active control system.

As one of the main tasks of this thesis, a **vertical position controller** was developed and implemented in JOREK based on the PID controller design, acting on the vertical position of the magnetic axis and its displacement velocity. It was shown in section 4.4 that the vertical position could be stabilized against the intrinsic instability of an elongated plasma and the plasma position can be prescribed within reasonable limits. While the controller implementation is not fully realistic as pointed out in section 3.3, it shows a qualitative behavior similar to the experiment, when current limits are applied. The implemented controller provides a tool for varying the vertical position by a direct feedback instead of varying the coil currents explicitly as it had been done before. Now, the position can be prescribed in JOREK easily and more precisely.

Towards the simulation of disruptions, an **artificial thermal quench** was triggered by an increased perpendicular heat and particle transport in section 4.5. The 2D simulations of the subsequent current quench and VDE, showed a reasonable dependence of the vertical displacement dynamics on the current quench rate. The controller with different current limits was employed in this setup, which showed a realistic qualitative behavior by slowing down the vertical displacement and stabilizing it completely for long current quench rates.

In a next step, non axisymmetric effects were added to represent the 3D evolution of the plasma, when the **thermal quench is triggered by massive material injection** in the setup described in section 4.6. The different phases of the thermal quench could be observed in the simulation, consisting of a decrease in temperature as well as the formation and growth of magnetic islands, which ultimately lead to a stochastization of the field lines and loss of thermal energy. The dynamics of the subsequent current quench and VDE could also be resolved in the simulation. As the JOREK model employed for the simulations in this thesis is simplified, not containing neutrals, the parallel velocity, radiation and further effects, the simulation cannot be compared 1:1 to experimental results.

However, the validation of the PSL and the first simulations of a simple thermal quench provide a strong basis for future work on the simulation of disruptions and VDEs in ASDEX Upgrade. **Future work** will include the modelling of more realistic structures by coupling the JOREK code to a more sophisticated code CARIDDI with the capability to represent 3D walls, conductive structures and coils beyond the thin wall approximation of STARWALL. Also, an extended plasma model capturing more physical effects will be used to obtain a more realistic VDE evolution, which will make it possible to draw direct comparisons to the experiment. Also, the more realistic sheath boundary conditions, which were included recently in JOREK [Art20b] will allow for a self-consistent description of the halo region with realistic currents and current distributions.

A Acknowledgments

First, I would like to thank Sibylle Günter for giving me the opportunity to write my thesis at IPP and also Friedrich Röpke for agreeing to supervise the thesis.

A big thank you to Matthias Hölzl for supervising this master thesis and the support on the way with useful discussions during walk&talks that eventually became zoom&talks. Thanks for having me back at IPP and encouraging me to continue with a PhD.

Special thanks to Javier Artola, for the support and motivating words during my stay at ITER and beyond. Especially for the helpful discussions, sharing your knowledge about VDEs and bringing some clarity into the chaos.

Thanks to Erika Strumberger for providing the simulation results of CASTOR3D for the benchmark in this work and the useful information about the code. And to Mike Dunne, for providing access to experimental data, background information about the measurements and making investigations to find the answers, when they were not readily at hand.

Finally, thanks to the whole JOREK team at IPP, especially my fellow students, for welcoming me into the group.

For parts of this work, the Marconi-Fusion supercomputer was used.

B Lists

B.1 List of Figures

1.1 Binding energy per nucleon . . . 2
1.2 Fusion product of tokamaks over the years . . . 3
1.3 Basic configuration of a tokamak . . . 7
1.4 Poloidal plasma cross section in X–point configuration . . . 9
1.5 Coordinate system of a tokamak . . . 10
1.6 Toroidal field modification by β_p . . . 11
1.7 Vacuum magnetic field in the poloidal plane . . . 12
1.8 Shaped plasma cross section . . . 12
1.9 Diagram of ASDEX Upgrade . . . 13
1.10 ASDEX Upgrade: coil system . . . 14
1.11 Passive Stabilisation Loop in ASDEX Upgrade . . . 15
1.12 Laplace force of the PF coils due to vertical displacement . . . 16
2.1 Three wire model: setup . . . 25
2.2 Three wire model: growth rates . . . 27
2.3 Path of halo currents in vacuum and wall . . . 29
2.4 Mechanism of a VDE following a disruption . . . 32
2.5 TQ and CQ time scales . . . 32
2.6 Closed loop feedback system . . . 39
2.7 Reaction to a step excitation of the PID controller . . . 40
2.8 Diagram of PF control system . . . 42
2.9 JOREK grid . . . 46
3.1 Coils and structures of AUG in JOREK and STARWALL . . . 50
3.2 STARWALL coils and wall in 3D . . . 50
3.3 PSL geometries in STARWALL . . . 51
3.4 Implementation of the PID controller in JOREK . . . 54
4.1 Coil validation: measurement of τ_{PSL} . . . 57
4.2 Coil validation: current induction between two coils . . . 58
4.3 Coil validation: placement of structures for the coil-wall interaction test . . . 58
4.4 Coil validation: currents of the coil-wall induction test . . . 58
4.5 Coil validation: comparison of the analytic and the JOREK magnetic field . . . 59
4.6 Coil validation: field lines due to the PF coils in the poloidal plane . . . 60
4.7 Coil validation: induction in wall and coil - setup . . . 61
4.8 Coil validation: induction in wall and coil - current part 1 . . . 62
4.9 Coil validation: induction in wall and coil - current part 2 . . . 62
4.10 Coil validation: induction in wall and coil - axis evolution . . . 63
4.11 Coil validation: induction in wall and coil - current part 3 . . . 63

4.12 Coil validation: flux conservation by a passive coil 64
4.13 Benchmark: resistivity profile 66
4.14 Benchmark: scan over viscosity 67
4.15 Benchmark: parameter scan at low conductivity 68
4.16 Benchmark: growth rates 69
4.17 VDE investigations: influence of the coil thickness on γ 70
4.18 VDE investigations: γ for different PSL geometries 71
4.19 VDE investigations: γ with and without PSL at different $\eta_{thin,w}$ 72
4.20 VDE investigations: effect on γ of the PSL at realistic wall resistivity 73
4.21 VDE investigations: γ and axis evolution for different PSL resistances 74
4.22 Controller: step response for different gain settings 75
4.23 Controller: effect of K_D on position control 76
4.24 Controller: effect of K_P on position control 76
4.25 Controller: shift axis position 77
4.26 elongation scan: separatrix outlines 78
4.27 elongation scan: γ and f^{-1} dependence on κ 79
4.28 elongation scan: axis evolution with and without control 80
4.29 Artificial TQ: temperature and current profile 81
4.30 Artificial TQ: loss of thermal energy and current decay 82
4.31 Artificial TQ: CQ rates and displacement velocity 83
4.32 Artificial TQ: CQ in the ideal wall limit 83
4.33 Artificial TQ: colormap of the current evolution in the poloidal plane 84
4.34 Artificial TQ: effect of the controller on the vertical velocity 85
4.35 TQ: density distribution over the $q = 2$ flux surface 88
4.36 TQ: Poincaré plots of the magnetic field lines 89
4.37 TQ: evolution of the kinetic energy of the different Fourier harmonics 90
4.38 TQ: decay of E_{th} and I_p followed by the vertical movement of plasma 90
4.39 TQ: density at ϕ =0° and 180° after the material injection 91
4.40 TQ: 3D evolution of the density 91

B.2 List of Tables

1.1 ASDEX Upgrade: machine and plasma parameters 13
2.1 Influences of the gains on the PID controller characteristics 40
3.1 Comparison of JOREK equilibrium to *Cliste* reconstruction 49
3.2 Self inductance values for the geometries 52
3.3 Parameters for vertical stability control and their typical values 53
4.1 Benchmark: parameters for the benchmark with CASTOR3D 68
4.2 VDEs for different elongations 79

C References

[Art20a] Artola, F. J., Lackner, K., Huijsmans, G. T. A., Hoelzl, M. et al. *Understanding the reduction of the edge safety factor during hot VDEs and fast edge cooling events.* In: Physics of Plasmas, vol. 27(2020)3:032501. http://dx.doi.org/10.1063/1.5140230.

[Art20b] Artola, F. J., Loarte, A., Matveeva, E., Havlicek, T. et al. *Simulations of COMPASS Vertical Displacement Events with a self-consistent model for halo currents including neutrals and sheath boundary conditions.* In: , (in preparation, 2020).

[Art20c] Artola, J., Sovinec, C. R., Jardin, S. C., Hoelzl, M. et al. *3D simulations of vertical displacement events in tokamaks: A benchmark of M3D-C1, NIMROD and JOREK.* In: Physics of Plasmas, (submitted, 2020). Pre-print at: https://arxiv.org/abs/2011.04523.

[AS18] Artola Such, F. J. *FREE-BOUNDARY SIMULATIONS OF MHD PLASMA INSTABILITIES IN TOKAMAKS.* Thesis, Université Aix Marseille (2018). https://tel.archives-ouvertes.fr/tel-02012234.

[AUG] *AUG Intranet.* (last checked: 2020-08-28).

[Bil] *IPP figure archive (Bilddatenbank).* (last checked: 2020-08-23).

[Boo12] Boozer, A. H. *Theory of tokamak disruptions.* In: Physics of Plasmas, vol. 19(2012)5:058101. http://dx.doi.org/10.1063/1.3703327.

[Boo13] Boozer, A. H. *Tokamak halo currents.* In: Physics of Plasmas, vol. 20(2013)8:082510. http://dx.doi.org/10.1063/1.4817742.

[Bre19] Breizman, B. N., Aleynikov, P., Hollmann, E. M. and Lehnen, M. *Physics of runaway electrons in tokamaks.* In: Nuclear Fusion, vol. 59(2019)8:083001. http://dx.doi.org/10.1088/1741-4326/ab1822.

[Che16] Chen, F. F. *Introduction to Plasma Physics and Controlled Fusion* (Springer International Publishing, Cham, 2016). ISBN 978-3-319-22308-7 978-3-319-22309-4.

[Coo] *Coordinates.* http://fusionwiki.ciemat.es/fusionwiki/images/1/10/Toroidal_coordinates.png, (last checked: 2020-08-24).

[Cza08] Czarny, O. and Huysmans, G. *Bézier surfaces and finite elements for MHD simulations.* In: Journal of Computational Physics, vol. 227(2008)16:7423–7445. http://dx.doi.org/10.1016/j.jcp.2008.04.001.

[DT19] De Tommasi, G. *Plasma Magnetic Control in Tokamak Devices.* In: Journal of Fusion Energy, vol. 38(2019)3-4:406–436. http://dx.doi.org/10.1007/s10894-018-0162-5.

[Dun] Dunne, M. *Internal Communication.*

[Eng] *Binding energy (figure).* https://upload.wikimedia.org/wikipedia/commons/5/53/Binding_energy_curve_-_common_isotopes.svg, (last checked: 2020-07-05).

[Fit11] Fitzpatrick, R. *Theory of nonaxisymmetric vertical displacement events in tokamaks*. In: Nuclear Fusion, vol. 51(2011)5:053007. http://dx.doi.org/10.1088/0029-5515/51/5/053007.

[Fra15] Franck, E., Hölzl, M., Lessig, A. and Sonnendrücker, E. *Energy conservation and numerical stability for the reduced MHD models of the non-linear JOREK code*. In: ESAIM: Mathematical Modelling and Numerical Analysis, vol. 49(2015)5:1331–1365. http://dx.doi.org/10.1051/m2an/2015014.

[Fre14] Freidberg, J. P. *Ideal MHD* (Cambridge University Press, New York, 2014).

[Fus] *Fusion product (figure)*. http://large.stanford.edu/courses/2012/ph240/ramos2/docs/Focus_on.pdf, (last checked: 2020-09-30).

[Geo] *geometry cross section*. http://fusionwiki.ciemat.es/fusionwiki/images/5/58/Geometry.png, (last checked: 2020-09-18).

[Ger14] Gerasimov, S. N., Hender, T. C., Morris, J., Riccardo, V. and and, L. E. Z. *Plasma current asymmetries during disruptions in JET*. In: Nuclear Fusion, vol. 54(2014)7:073009. http://dx.doi.org/10.1088/0029-5515/54/7/073009.

[Gia15] Giannone, L., Fischer, R., McCarthy, P., Odstrcil, T. et al. *Improvements for real-time magnetic equilibrium reconstruction on ASDEX Upgrade*. In: Fusion Engineering and Design, vol. 100(2015):519–524. http://dx.doi.org/10.1016/j.fusengdes.2015.07.029.

[Gir17] Giruzzi, G., Yoshida, M., Artaud, J. F., Asztalos, . et al. *Physics and operation oriented activities in preparation of the JT-60SA tokamak exploitation*. In: Nuclear Fusion, vol. 57(2017)8:085001. http://dx.doi.org/10.1088/1741-4326/aa7962.

[Goe04] Goedbloed, J., Goedbloed, J. and Poedts, S. *Principles of magnetohydrodynamics: With applications to laboratory and astrophysical plasmas* (Cambridge University Press, 2004). ISBN 978-0-521-62607-1.

[Gra96] Granetz, R., Hutchinson, I., Sorci, J., Irby, J. et al. *Disruptions and halo currents in Alcator C-Mod*. In: Nuclear Fusion, vol. 36(1996)5:545–556. http://dx.doi.org/10.1088/0029-5515/36/5/I02.

[Gru93a] Gruber, O., Gernhardt, J., McCarthy, P., Lackner, K. et al. *POSITION AND SHAPE CONTROL ON ASDEX-UPGRADE*. In: C. Ferro, M. Gasparotto and H. Knoepfel (eds.), *Fusion Technology 1992*, pp. 1042–1046 (North-Holland, Oxford, 1993). ISBN 978-0-444-89995-8. http://www.sciencedirect.com/science/article/pii/B9780444899958502022.

[Gru93b] Gruber, O., Lackner, K., Pautasso, G., Seidel, U. and Streibl, B. *Vertical displacement events and halo currents*. In: Plasma Physics and Controlled Fusion, vol. 35(1993)SB:B191–B204. http://dx.doi.org/10.1088/0741-3335/35/sb/015.

[Gru95] Gruber, O., Pautasso, G., Seidel, U., Buechl, K. et al. *Disruptions in vertically elongated ASDEX Upgrade plasmas*. In: Plasma physics and controlled nuclear fusion research 1994. V. 1. Proceedings of the fifteenth international conference, (1995). http://inis.iaea.org/Search/search.aspx?orig_q=RN:27018004.

[Hö12] Hölzl, M., Merkel, P., Huysmans, G. T. A., Nardon, E. et al. *Coupling JOREK and STARWALL Codes for Non-linear Resistive-wall Simulations*. In: Journal of Physics: Conference Series, vol. 401(2012):012010. http://dx.doi.org/10.1088/1742-6596/401/1/012010.

[Hen07] Hender, T., Wesley, J., Bialek, J., Bondeson, A. et al. *Chapter 3: MHD stability, operational limits and disruptions*. In: Nuclear Fusion, vol. 47(2007)6:S128–S202. http://dx.doi.org/10.1088/0029-5515/47/6/S03.

[Hoe14] Hoelzl, M., Huijsmans, G. T. A., Merkel, P., Atanasiu, C. et al. *Non-linear Simulations of MHD Instabilities in Tokamaks Including Eddy Current Effects and Perspectives for the Extension to Halo Currents*. In: Journal of Physics: Conference Series, vol. 561(2014):012011. http://dx.doi.org/10.1088/1742-6596/561/1/012011.

[Hoe20] Hoelzl, M., Huijsmans, G., Pamela, S., Becoulet, M. et al. *The JOREK non-linear extended mhd code and applicationsto large-scale instabilities and their control in magneticallyconfined fusion plasmas*. In: Nuclear Fusion, (submitted, 2020).

[Hum99] Humphreys, D. A. and Kellman, A. G. *Analytic modeling of axisymmetric disruption halo currents*. In: Physics of Plasmas, vol. 6(1999)7:2742–2756. http://dx.doi.org/10.1063/1.873231.

[Huy07] Huysmans, G. T. A. and Czarny, O. *MHD stability in X-point geometry: simulation of ELMs*. In: Nuclear Fusion, vol. 47(2007)7:659–666. http://dx.doi.org/10.1088/0029-5515/47/7/016.

[Igo15] Igochine, V. (ed.). *Active Control of Magneto-hydrodynamic Instabilities in Hot Plasmas*. Springer Series on Atomic, Optical, and Plasma Physics (Springer-Verlag, Berlin Heidelberg, 2015). ISBN 978-3-662-44221-0.

[ITE99] ITER Physics Expert Group on Disruptions, Plasma Control, and MHD and ITER Physics Basis Editors. *Chapter 3: MHD stability, operational limits and disruptions*. In: Nuclear Fusion, vol. 39(1999)12:2251–2389. http://dx.doi.org/10.1088/0029-5515/39/12/303.

[Jar82] Jardin, S. and Larrabee, D. *Feedback stabilization of rigid axisymmetric modes in tokamaks*. In: Nuclear Fusion, vol. 22(1982)8:1095–1098. http://dx.doi.org/10.1088/0029-5515/22/8/011.

[Kia05] Kiam Heong Ang, Chong, G. and Yun Li. *PID control system analysis, design, and technology*. In: IEEE Transactions on Control Systems Technology, vol. 13(2005)4:559–576. http://dx.doi.org/10.1109/TCST.2005.847331.

[Kik12] Kikuchi, M., Lackner, K., Tran, M. and Agency, I. A. E. *Fusion physics*. Publication (International Atomic Energy Agency, 2012). ISBN 978-92-0-130410-0.

[Kir17] Kiramov, D. I. and Breizman, B. N. *Model of vertical plasma motion during the current quench*. In: Physics of Plasmas, vol. 24(2017)10:100702. http://dx.doi.org/10.1063/1.4993071.

[Kre20] Krebs, I., Artola, F. J., Sovinec, C. R., Jardin, S. C. et al. *Axisymmetric simulations of vertical displacement events in tokamaks: A benchmark of M3D-C1, NIMROD,*

and JOREK. In: Physics of Plasmas, vol. 27(2020)2:022505. http://dx.doi.org/10.1063/1.5127664.

[Laz90] Lazarus, E., Lister, J. and Neilson, G. *Control of the vertical instability in tokamaks*. In: Nuclear Fusion, vol. 30(1990)1:111–141. http://dx.doi.org/10.1088/0029-5515/30/1/010.

[McC99] McCarthy, P. J., Martin, P. and Schneider, W. *The CLISTE Interpretive Equilibrium Code*. Tech. Rep. IPP 5/85, Max-Planck-Institut für Plasmaphysik., Garching (1999). http://hdl.handle.net/11858/00-001M-0000-0027-6023-D.

[Mer03] Mertens, V., Raupp, G. and Treutterer, W. *Chapter 3: Plasma Control in ASDEX Upgrade*. In: Fusion Science and Technology, vol. 44(2003)3:593–604. http://dx.doi.org/10.13182/FST03-A401.

[Mer15] Merkel, P. and Strumberger, E. *Linear MHD stability studies with the STARWALL code*. In: arXiv:1508.04911 [physics], (2015). http://arxiv.org/abs/1508.04911.

[Miy16] Miyamoto, K. *Plasma Physics for Controlled Fusion*. Springer Series on Atomic, Optical, and Plasma Physics, 2 ed. (Springer-Verlag, Berlin Heidelberg, 2016). ISBN 978-3-662-49780-7.

[Nak96a] Nakamura, Y., Yoshino, R., Neyatani, Y., Tsunematsu, T. et al. *Mechanism of vertical displacement events in JT-60U disruptive discharges*. In: Nuclear Fusion, vol. 36(1996)5:643–656. http://dx.doi.org/10.1088/0029-5515/36/5/i10.

[Nak96b] Nakamura, Y., Yoshino, R., Pomphrey, N. and Jardin, S. C. *Acceleration mechanism of vertical displacement event and its amelioration in tokamak disruptions*. In: Journal of Nuclear Science and Technology, vol. 33(1996)8:609–619. http://dx.doi.org/10.1080/18811248.1996.9731967.

[Nak02] Nakamura, Y., Pautasso, G., Gruber, O. and Jardin, S. C. *Axisymmetric disruption dynamics including current profile changes in the ASDEX-Upgrade tokamak*. In: Plasma Physics and Controlled Fusion, vol. 44(2002)8:1471–1481. http://dx.doi.org/10.1088/0741-3335/44/8/304.

[Pam20] Pamela, S. J. P., Bhole, A., Huijsmans, G. T. A., Nkonga, B. et al. *Extended full-mhd simulation of non-linear instabilities in tokamak plasmas*. In: Physics of Plasmas, vol. 27(2020)10:102510. http://dx.doi.org/10.1063/5.0018208. https://doi.org/10.1063/5.0018208.

[Pau11a] Pautasso, G., Giannone, L., Gruber, O., Herrmann, A. et al. *The halo current in ASDEX Upgrade*. In: Nuclear Fusion, vol. 51(2011)4:043010. http://dx.doi.org/10.1088/0029-5515/51/4/043010.

[Pau11b] Pautasso, G., Zhang, Y., Reiter, B., Giannone, L. et al. *Contribution of ASDEX Upgrade to disruption studies for ITER*. In: Nuclear Fusion, vol. 51(2011)10:103009. http://dx.doi.org/10.1088/0029-5515/51/10/103009.

[Ric05] Riccardo, V., Barabaschi, P. and Sugihara, M. *Characterization of plasma current quench at JET*. In: Plasma Physics and Controlled Fusion, vol. 47(2005)1:117–129. http://dx.doi.org/10.1088/0741-3335/47/1/007.

[Ric10] Riccardo, V., Arnoux, G., Cahyna, P., Hender, T. C. et al. *JET disruption studies in support of ITER*. In: Plasma Physics and Controlled Fusion, vol. 52(2010)12:124018. http://dx.doi.org/10.1088/0741-3335/52/12/124018.

[Sch17] Schwarz, N. *Towards the self-consistent implementation of active and passive coils for non-linear magnetohydrodynamic simulations of tokamak plasmas*. bachelor thesis, Universität des Saarlandes, Max Planck Institut für Plasmaphysik, Saarbrücken (2017).

[Seh16] Sehmer, T., Lackner, K., Strumberger, E., Fable, E. et al. *Growth of axisymmetric instabilities in ASDEX upgrade*. In: Fusion Science and Technology, vol. 70(2016)1:73–82. http://dx.doi.org/10.13182/FST15-175.

[Sha] *Plasma cross section*. https://www.euro-fusion.de, (last checked: 2017-07-14).

[Shi07] Shimada, M., Campbell, D. J., Mukhovatov, V., Fujiwara, M. et al. *Chapter 1: Overview and summary*. In: Nuclear Fusion, vol. 47(2007)6:S1–S17. http://dx.doi.org/10.1088/0029-5515/47/6/S01.

[Str91] Strait, E. J., Lao, L. L., Luxon, J. L. and Reis, E. E. *Observation of poloidal current flow to the vacuum vessel wall during vertical instabilities in the DIII-D tokamak*. In: Nuclear Fusion, vol. 31(1991)3:527–534. http://dx.doi.org/10.1088/0029-5515/31/3/011.

[Str16] Strumberger, E. and Günter, S. *CASTOR3D: linear stability studies for 2D and 3D tokamak equilibria*. In: Nuclear Fusion, vol. 57(2016)1:016032. http://dx.doi.org/10.1088/0029-5515/57/1/016032.

[Tok] *Tokamak schematic*. http://www.100milliondegrees.com/wp-content/uploads/2015/10/Tokamak_scheme.jpg, (last checked: 2020-08-24).

[Upg] Upgrade, A. *Ringbuch*. Tech. rep., IPP Garching.

[War92] Ward, D. and Jardin, S. *Effects of plasma deformability on the feedback stabilization of axisymmetric modes in tokamak plasmas*. In: Nuclear Fusion, vol. 32(1992)6:973–994. http://dx.doi.org/10.1088/0029-5515/32/6/I07.

[Wes11] Wesson, J. and Campbell, D. *Tokamaks*. International series of monogr (OUP Oxford, 2011). ISBN 978-0-19-959223-4.

[Wie90] Wieczorek, A., Blaumoser, M. and Schwarz, J. *The plasma position control system for ASDEX Upgrade*. In: *1990 Fourth International Conference on Power Electronics and Variable-Speed Drives (Conf. Publ. No. 324)*, pp. 464–471 (1990).

[Wig11] Wigger, C. *Development and Application of a Nonlinear Axisymmetric Resistive MHD-Code*. Ph.D. thesis, Technische Universität München, München (2011).

D Magnetic axis finding

Determining the magnetic axis in JOREK is an important feature for using the feedback system on the vertical position. While the experiment relies on the data of magnetic flux measurements to reconstruct the equilibrium, the magnetic axis can be determined directly from the magnetic flux in JOREK. The method for reconstructing the magnetic axis was developed here [AS18] and will be described in the following.

On the magnetic axis, the poloidal field $\mathbf{B}_{pol} = \boldsymbol{\nabla}\psi \times \boldsymbol{\nabla}\phi$ is zero. The algorithm aims to find the points, where the gradient of the flux $\boldsymbol{\nabla}\psi = 0$ using Newton's method.

1. $\boldsymbol{\nabla}\psi$ is calculated on control points on the Bézier element inside a specific region in $(R \pm \mathrm{d}R, Z \pm \mathrm{d}Z)$.

2. In the element of minimum gradient $|\boldsymbol{\nabla}\psi|$, the Newton-Raphson scheme for finding the root is applied.

   a) The root is found in this element.

   b) If the root is not found in this element, the search continues in the next element with minimum $|\boldsymbol{\nabla}\psi|$.

3. The element containing the root of $|\boldsymbol{\nabla}\psi|$, is used as the center of the search region in the following time step.

The same algorithm can be applied for finding the X–point, as the $\mathbf{B}_{pol}$ is also zero there. For this reason, the search region of the magnetic axis has to be chosen in a way, that it does not contain the X–point region. For VDEs, the search radius should also not be chosen too small, as the displacement of the magnetic axis can happen on a fast time scale. If the algorithm fails or for large, unphysical jumps between two time steps, the algorithm of vertical control system fails, leading to large oscillations of the control coil currents.

Erklärung:

Ich versichere, dass ich diese Arbeit selbstständig verfasst habe und keine anderen als die angegebenen Quellen und Hilfsmittel benutzt habe.

Heidelberg, den (Datum) .....